University of Denver

Digital Commons @ DU

1-1-2011

High Frequency Thermally Actuated Single Crystalline Silicon Micromechanical Resonators with Piezoresistive Readout

Amir Rahafrooz
University of Denver

Recommended Citation

HIGH FREQUENCY THERMALLY ACTUATED SINGLE CRYSTALLINE SILICON

MICROMECHANICAL RESONATORS WITH PIEZORESISTIVE READOUT

_____

A Dissertation

Presented to

The Faculty of Engineering and Computer Science

University of Denver

_____

In Partial Fulfillment

of the Requirements for the Degree

Doctor of Philosophy

_____

by

Amir Rahafrooz

August 2011

Advisor: Siavash Pourkamali

Author: Amir Rahafrooz
Title: HIGH FREQUENCY THERMALLY ACTUATED SINGLE CRYSTALLINE
SILICON MICROMECHANICAL RESONATORS WITH PIEZORESISTIVE
READOUT
Advisor: Siavash Pourkamali
Degree Date: August 2011

Abstract

Over the past decades there has been a great deal of research on developing high
frequency micromechanical resonators. As the two most common and conventional
MEMS resonators, piezoelectric and electrostatic resonators have been at the center of
attention despite having some drawbacks. Piezoelectric resonators provide low
impedances that make them compatible with other low impedance electronic
components, however they have low quality factors and complicated fabrication
processes. In case of electrostatic resonators, they have higher quality factors but the need
for smaller transductions gaps complicates their fabrication process and causes squeezed
film damping in Air. In addition, the operation of both these resonators deteriorates at
higher frequencies.

In this presented research, thermally actuated resonators with piezoresistive
readout have been developed. It has been shown that not only do such resonators require
a simple fabrication process, but also their performance improves at higher frequencies
by scaling down all the dimensions of the structure. In addition, due to the internal
thermo-electro-mechanical interactions, these active resonators can turn some of the
consumed electronic power back into the mechanical structure and compensate for the
mechanical losses. Therefore, such resonators can provide self-Q-enhancement and self-
sustained-oscillation without the need for any electronic circuitry. In this research these

facts have been shown both experimentally and theoretically. In addition, in order to further simplify the fabrication process of such structures, a new controlled batch fabrication method for fabricating silicon nanowires has been developed. This unique fabrication process has been utilized to fabricate high frequency, low power thermal-piezoresistive resonators. Finally, a new thermal-piezoresistive resonant structure has been developed that can operate inside liquid. This resonant structure can be utilized as an ultra sensitive biomedical mass sensor.

ACKNOWLEDGEMENTS

Table of Contents

LIST OF TABLES

LIST OF FIGURES

LIST OF TERMS

AC: Alternating Current

AlN: Aluminum Nitride

BAR: Bulk Acoustic wave Resonator

BAW: Bulk Acoustic Wave

BOX: Buffer Oxide

CMOS: Complementary Metal-Oxide Semiconductor

DC: Direct Current

DRIE: Deep Reactive Ion Etching

FBAR: Film Bulk Acoustic Resonator

HF: High Frequency

HF: Hydrofluoric Acid

IBAR: I-shaped Bulk Acoustic Resonator

IC: Integrated Circuit

KOH: Potassium Hydroxide

MEM: Micro-Electro-Mechanical

MEMS: Micro-Electro-Mechanical Systems

NEMS: Nano-Electro-Mechanical Systems

RIE: Reactive Ion Etching

Q: Quality Factor

QCM: Quartz Crystal Microbalance

SAW: Surface Acoustic Wave

SCS: Single Crystal Silicon

SEM: Scanning Electron Microscopy

SiC: Silicon Carbide

SMR: Solidly Mounted Resonator

SOI: Silicon On Insulator

TCXO: Temperature Compensated Quartz Oscillator

TED: Thermo Elastic Damping

VHF: Very High Frequency

UHF: Ultra High Frequency

1. INTRODUCTION

1.1 Mechanical Resonator Concept

A mechanical resonator is a structure which is free to vibrate. A classical example of such in macroscale is a guitar string. Every guitar string depending on its length, tension and properties of its structural material has a certain frequency of vibration. In case of guitar the resonance frequencies of all strings fall in the audio frequency range (20Hz-20kHz).

If the resonator dimensions are scaled down into the micrometer range, much higher resonance frequencies anywhere from a few kHz to tens of GHz are achievable. Figure 1.1 shows a clamped-clamped beam micro-electro-mechanical system (MEMS) resonator. This released bridge can vibrate in its fundamental out-of-plane flexural mode with resonance frequency of ~5MHz [1].

A mechanical resonator can be modeled as a series/parallel RLC circuit in electronics or as a mass, spring, and damper system in mechanics. Figure 1.2 shows a mass (m), spring (k) and damper (D) system as well as its frequency response with the resonance frequency of f_0. Transfer function of such a system which relates the applied actuation force (F) to the displacement of the resonator (x) can be written as follows:

$$\frac{x(s)}{F(s)} = \frac{1}{k\left(\frac{s^2}{\omega_0^2} + \frac{s}{\omega_0 Q} + 1\right)} \tag{1.1}$$
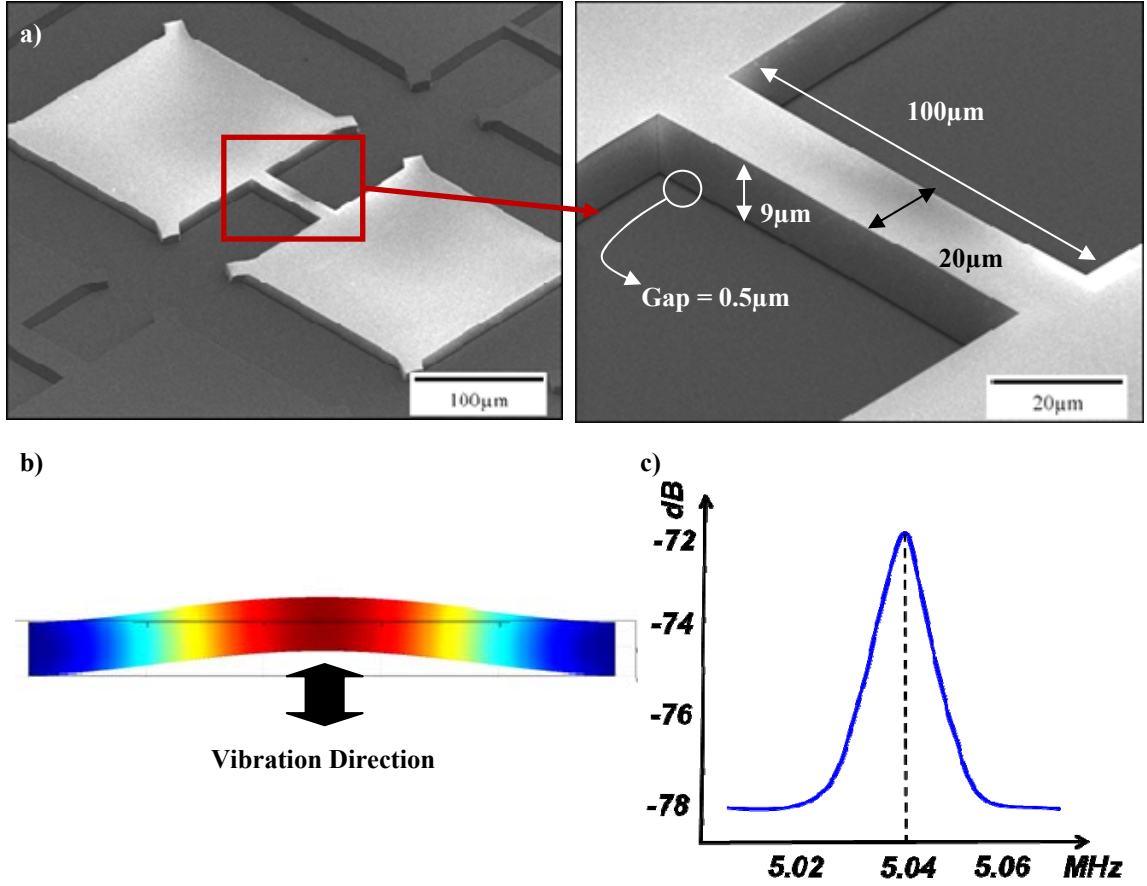
Figure 1.1. a) A scanning electron microscope (SEM) view of a single crystalline silicon clamp-clamp beam resonator. b) Modal analysis of the clamp-clamp resonator showing its side-view vibration amplitude in its fundamental out-of-plane mode. Blue and red colors represent the minimum and maximum displacements respectively. c) Frequency response of the clamp-clamp beam resonator with the resonance frequency of ~5MHz [1].
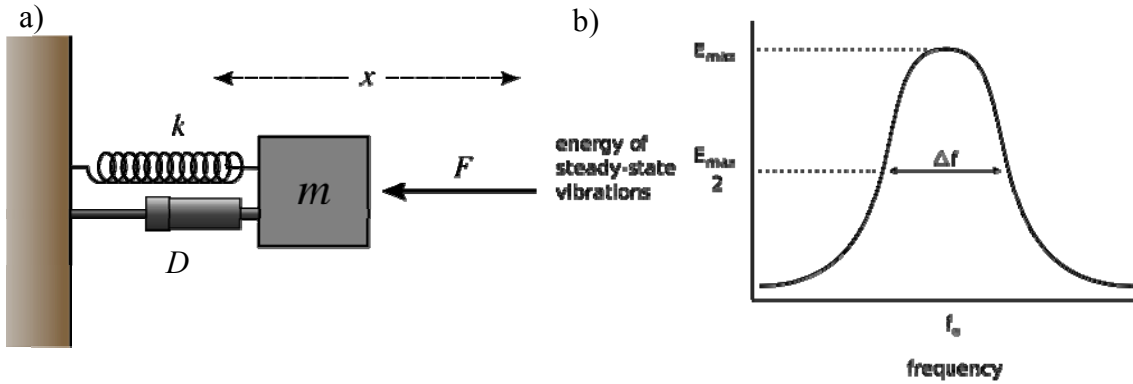
Figure 1.2. a) A mass connected to a damper (D) and a spring (k) to form a second order mechanical system. b) Frequency response of the mass, spring and damper system in part a, showing its resonance frequency plus the points at which the vibration energy decreases to half of its maximum value.

where s is the Laplace transform parameter, ω_0 and Q are the angular resonance

frequency and quality factor of the resonator respectively and are related to the component values as follows:

$$\omega_0 = 2\pi f_0 = \sqrt{\frac{k}{m}} \tag{1.2}$$

$$Q = \frac{\sqrt{k.m}}{D} \tag{1.3}$$

Both of these parameters can be found from the frequency response of the resonator; resonance frequency is the frequency at which the vibration amplitude maximizes which is in fact in the center of the passband of the frequency response. On the other hand, quality factor can be defined as:

$$Q = \frac{f_0}{\Delta f} = \frac{\omega_0}{\Delta \omega} \tag{1.4}$$

where Δf and $\Delta \omega$ are the bandwidth and angular bandwidth of the resonator at which the energy of the resonator decreases to half of its maximum value (Fig. 1.2b). Physically Q is proportional to the energy stored in the resonator over the energy loss inside the structure.

1.2   Mechanical Resonator Applications

For decades, mechanical resonators have been widely used as frequency references and filters in electronic circuits. It has been just a few years that microscale resonators gradually have entered the market. Due to their smaller size, lower power consumption and compatibility with integrated circuit technologies, they have great potential as replacements for larger scale resonators. In this way, portable wireless communication systems benefit most [2].

One of the other applications of resonators is their ability for direct mass sensing of different particles. If a particle with small mass (Δm) sits on a resonator, based on Eq.

(1.2) the resonance frequency of the resonator decreases proportionally to the added mass. To show this, by taking a derivative from both sides of Eq. (1.2) the following equation can be derived:

$$\frac{\Delta f}{f} = -\frac{\Delta m}{2m}$$

(1.5)

where Δf is the change in resonance frequency of the resonator due to the added mass. Based on Eq. (1.5) it is obvious that by using smaller micro and nano scale resonators for sensing, not only the resonance frequency increases but also the resonant mass decreases. These two changes work in favor of the mass sensor and make the resonator more sensitive to the added mass.

1.3 Mechanical Resonator Transduction

In order to be able to use a mechanical resonator, first a mechanism is required to actuate the resonator and initiate its mechanical vibration. To do so a force with proper amplitude, phase and frequency should be applied to the resonator. After the vibration started, another mechanism is needed to measure the vibration amplitude of the resonator and convert it into an electric signal. A combination of these actuation and sensing mechanisms are called transduction of the resonator. There are different transduction mechanisms for macro and especially micro mechanical resonators that will be covered in this chapter.

1.3.1 Piezoelectric Transduction

There are certain materials called piezoelectric material. Due to the piezoelectric effect they can be used for transduction of resonators. By applying an electric filed to the piezoelectric material, there is going to be a mechanical force generated within the structure that can actuate the resonator (Fig. 1.3). On the other hand, by applying a

mechanical force into the material, an electric charge is generated inside the material that could be sensed and used to detect the vibration amplitude of the resonator.

The nature of the piezoelectric effect is closely related to the occurrence of electric dipole moments in solids. The piezoelectric material is composed of ions or molecules with asymmetric charge surroundings. Dipoles near each other tend to be aligned in regions called Weiss domains [3]. The domains are usually randomly oriented, but can be aligned using the process of poling, a process by which a strong electric field is applied across the material. During this alignment due to the applied dipole moments, a mechanical force would be generated and the material would be stretched along the direction of the applied electric field (Fig. 1.3).
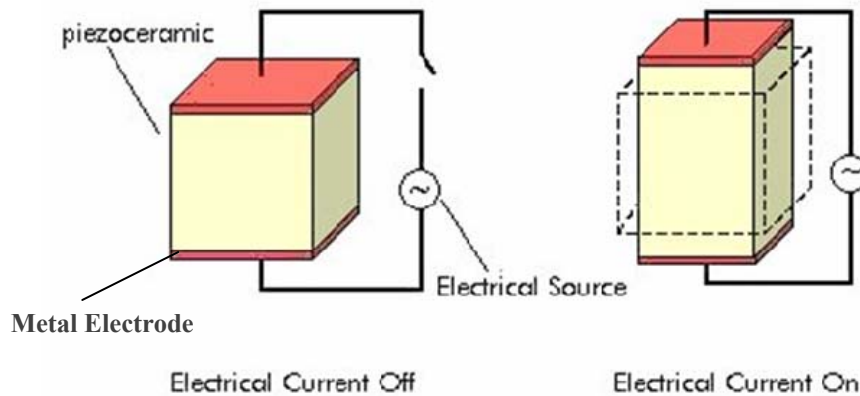
Figure 1.3. Acoustic-wave propagation in bulk acoustic wave (BAW) piezoelectric resonators. The piezoelectric material is sandwiched between two metal electrodes.

Based on the structure and the vibration mode, the generated acoustic waves can be propagated using either surface acoustic waves (SAW) or bulk acoustic waves (BAW) [4]. The waves we can see propagating on the surface of a lake after hitting the water mass with a stone illustrate the concept of a SAW. While, the sound waves traveling

through the air until reaching our ears are of the BAW type. From the acoustic wave propagation view piezoelectric resonators can be divided into SAW and BAW resonators.

Piezoelectric transduction is one of the first mechanisms traditionally used for decades for macro mechanical resonator transduction. There are different macroscale piezoelectric resonators that vary in the used piezo material and the structure.

Quartz crystal which is the first material used for implementation of piezoelectric resonators, still has a lot of applications as frequency references. The reason is its superior stability in compare to other materials. Piezoelectricity was discovered by Jacques and Pierre Curie in 1880 by investigating quartz resonators for use in sonar during World War I [5]. In 1928, Warren Marrison (of Bell Telephone Laboratories) developed the first quartz crystal clock. This invention replaced the pendulums as the time reference inside clocks. Since then, the performance of quartz frequency standards has gradually improved with new innovations such as use of temperature-compensated quartz crystals (TCXO) [6] and discovery of highly temperature stable crystal cuts such as SC-cut quartz crystal [7].

SAW resonator is one of the more recent macroscale piezoelectric resonators. It consists of a piezoelectric substrate with two or more comb low-density metal electrodes potentially two acoustic reflectors patterned on top of the piezoelectric material (Fig. 1.4). The applied electric field using one of the electrodes generates lateral acoustic waves on the surface of the substrate; the generated waves propagate on the substrate and reach the other metal electrode where they can be transuded back to an electrical signal. The interval between consecutive combs of each of the electrodes determines the wave length of the resonance frequency of the resonator [4].

Reflectors

(piezoelectric substrate) Comb Electrodes
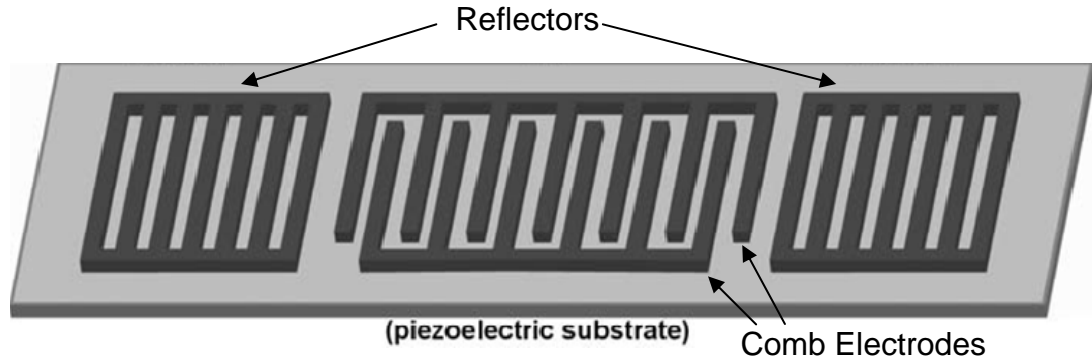
Figure 1.4. One-port SAW resonator with two acoustic reflectors on both sides of the resonator [4].

SAW resonators can be used as filters inside cell phones and other wireless communication systems [8]. However, when a mobile communication system uses a radio frequency higher than 2 GHz, it becomes very difficult to realize low-loss and sharp-cut off filters using SAW technology [9]. That is mainly because of the gradual decrease in the Q of such resonators. The reason is that at such high frequencies the width and also the interval between consecutive combs of the metal electrodes falls in the submicron and nano scale range. This not only causes some fabrication challenges, but also increases the electric resistance of such fine comb electrodes. The high electric resistance lowers the Q at higher frequencies.

To increase the performance of piezoelectric resonators at higher frequencies, the piezoelectric thin film resonators attracted attention that take advantage of bulk acoustic waves (BAW) rather than SAW. They basically consist of a piezoelectric layer sandwiched by two metal electrodes (Fig. 1.3) [4, 9, 10]. The applied electric filed actuate the resonator in its extensional mode. Therefore, the resonance frequency is mostly determined by the thickness of the piezoelectric material. As a group of such resonators, thin-film bulk acoustic wave resonators (FBAR) were first introduced by Lakin and Wang in 1981. Figure 1.5a shows a typical FBAR structure fabricated on a

7

silicon substrate with the integrated air gap between the vibrating piezoelectric material and the substrate. Such structure provided higher Qs especially at higher frequencies however it added to the fabrication challenges; In order to achieve a precise frequency adjustment the thickness of all the contributing layers should be finely controlled. The other utilized BAW resonator is the solidly mounted resonator (SMR) [4], which has an acoustic mirror made of a multi layered acoustic film. Figure 1.5b shows a typical SMR structure. SMR is more robust than the FBAR about the inner stress between the piezoelectric layer and metal electrodes and is more compatible with IC fabrication technologies. However the increased number of fabrication steps further complicates its fabrication process.
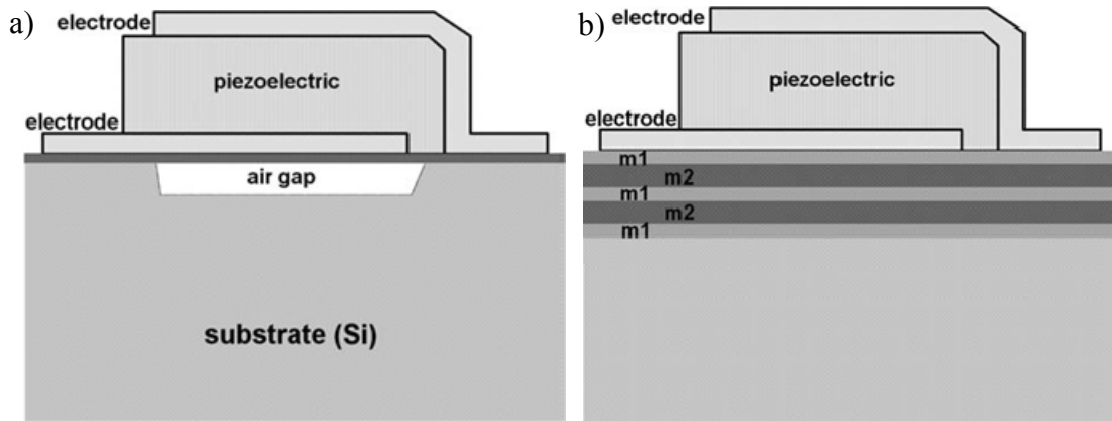
Figure 1.5. Structures of two bulk acoustic wave resonators; a) a micro machined air gap thin-film bulk acoustic wave resonators (FBAR) and b) a solidly mounted resonator (SMR) with a Bragg reflector [4].

Although both FBAR and SMR structures had improved performances especially at higher frequencies and also relatively smaller size in compare to SAW structure, SAW filters are still inexpensive and have their own applications. However, the disadvantage for all such structures is their large size that limits miniaturization of portable communications systems. In addition in case of FBAR and SMR resonators, due to the dependency of the resonance frequency of the resonator to the thickness of the

piezoelectric material, simultaneous fabrication of resonators with different resonance frequencies on a single chip is impossible [9]. To avoid such problems, several efforts have been carried out to come up with new miniaturized piezoelectric resonator structures on silicon substrates.

Piazza et. al. [11-13] presented a new class of aluminum nitride (AlN) piezoelectric resonators that have their fundamental frequency defined by in-plane dimensions. For this reason the devices were called contour-mode resonators. The use of contour modes allowed the batch fabrication of arrays of piezoelectric microresonators with different frequencies on a single chip. These devices mostly were realized in the form of rectangular plates. Figure 1.6 shows a schematic diagram of a microscale one-port aluminum nitride counter mode piezoelectric resonator. The generated eclectic filed along the thickness of the resonator excites the resonator either in length-extensional or width-extensional mode shapes.
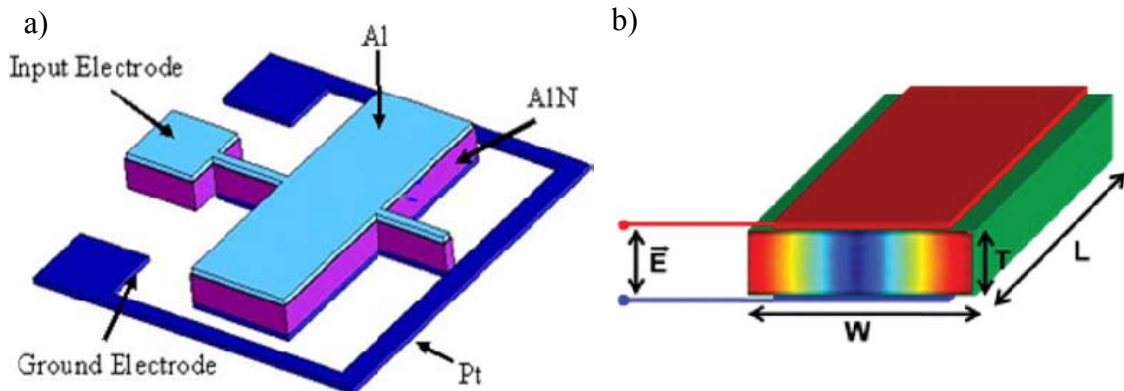
Figure 1.6. Schematic representations of one-port AlN contour-mode rectangular plate resonator [12].

The other class of microscale piezoelectric resonators that developed in parallel with the monolithic AlN counter mode resonators is the counter mode piezoelectric on silicon counter mode resonators [14, 15]. In this structure, piezoelectric material is used

for transduction of silicon body of the resonator. Recently the same structure has been used however, by using diamond rather than silicon as the resonating material higher quality factors has been achieved at higher frequencies [16].
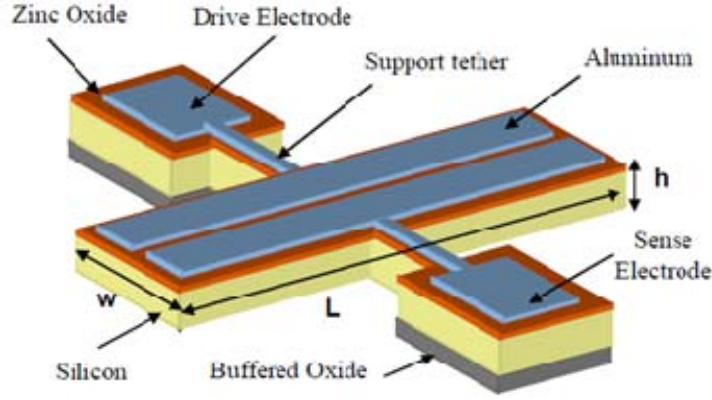
Figure 1.7. Schematic view of a two-port piezoelectric on silicone counter mode resonator [14].

1.3.2   Scaling the Microscale Piezoelectric Resonators

In a microscale AlN counter mode piezoelectric resonator with the dimensions shown in Fig. 1.6b, the fundamental lateral extensional resonance frequency f_0 is set by the width W, other than that electrical capacitance C_0 and motional resistance of the resonator have the following proportionality to the dimensions of the resonator [17]:

$$C_0 \propto \frac{LW}{T} \tag{1.6}$$

$$R_m \propto \frac{T}{L} \tag{1.7}$$

By scaling down the resonance frequency f_0 to values above 3GHz the width W should decrease to values below 1.2μm. However, by doing so according to Eq. (1.6) electrical capacitance could decrease to values less than the parasitic capacitance of the resonator that can completely mask the output signal of the resonator. Therefore, in order to improve the performance of such resonator at very high frequencies not only the W should be decreased but also at the same time the overall area of the electrodes should be

10

somehow increased to provide large enough capacitances. Also according to Eq. (1.6) further thinning down the piezoelectric layer would help having higher capacitances. To satisfy these requirements, Rinaldi et. al. [17] patterned the top metal layer on top of piezoelectric material into parallel electrodes. In this case the width of each of these parallel electrodes determines the resonance frequency of the resonator which is off-course one of the higher frequency lateral-extensional modes of the block resonator (Fig. 1.8). For similar reasons in order to increasing the resonance frequency of microscale piezo on silicon structures, similar comb-shape metal electrodes is usually used.

Overall, piezoelectric micro-resonators could provide impedances close to 50Ω which provides the impedance match needed for connecting to 50Ω instruments. They can be fabricated close to integrated circuits by a CMOS compatible fabrication process. However it requires deposition of piezoelectric and metal thin films generally resulting in lower quality factors and frequency and quality control issues.
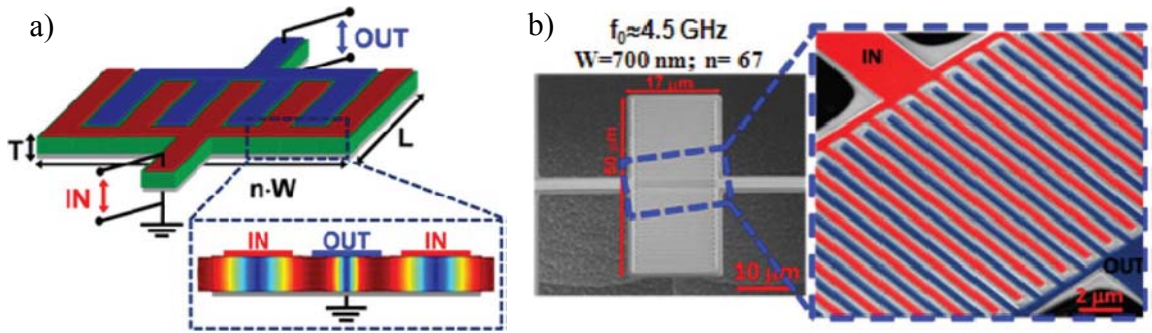
Figure 1.8. a) Schematic view and b) SEM view of a super-high-frequency two-port AlN counter mode resonator [17]

1.3.3 Capacitive Transduction

Capacitive or electrostatic transduction is one of the other mechanisms widely used for micromechanical resonator transduction. Assuming a parallel plate capacitor, by applying a voltage across the plates, the accumulated opposite charges on both surfaces

apply an attractive force to each other, leading to the attraction of the plates. This force depends on gap-size, area and the applied voltage across the plates. By applying an alternating voltage across the plates, the periodic mechanical force can be used to actuate a micromechanical resonator. On the other hand, in order to sense the vibration amplitude of a resonator, the same parallel plate capacitor can be utilized. By connecting the parallel plate capacitor to a constant DC voltage, if somehow the distance between the plates changes, there is going to be a change in capacitance of the capacitor. This causes a transient current to be generated that can be measured. In a vibrating resonator, the mechanical vibration can change the gap size and therefore, produce an alternating output current.

Figure 1.9 shows a schematic view of a disk resonator vibrating in its in-plane counter resonance mode. The disk in the middle is free to vibrate. By applying an AC voltage while the disk itself has been connected to a constant DC voltage, it will be actuated. Then since there is a constant DC voltage between the disk and the right-side electrode, an alternating output current will be generated during the vibration.
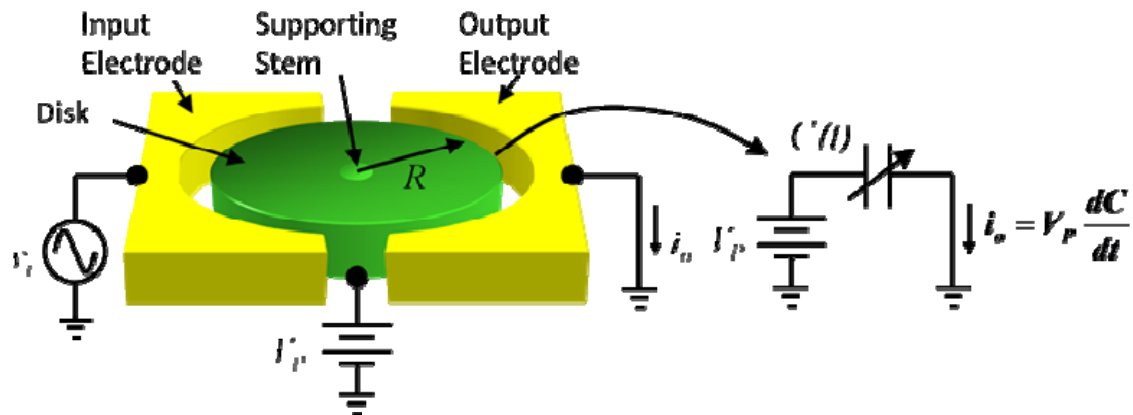
Figure 1.9. A schematic view of a counter mode electrostatic disk resonator. the left and right side electrodes are being used for actuation and sensing of the resonator respectively.

The electrostatic resonators are usually homogeneous. They mostly made of single crystalline silicon which is a low cost material with relatively simple processing technologies. Silicon has lower loss in compare to piezoelectric martial. In addition, in this structure the conductive electrodes are physically isolated from the resonator body through the capacitive gaps which lowers the anchor loss. As a result quality factor of capacitive resonators can reach one order of magnitude larger values than their piezoelectric counterparts. Furthermore, since the resonance frequency of such resonators is usually determined by the photolithography, electrostatic resonators in a wide range of frequencies can be simultaneously fabricated on a single substrate.

On the other hand, the low electromechanical coupling is such resonators has led to high output impedances much larger than the desired 50Ω resistance [18-20]. To overcome this problem, there have been some efforts to decrease the gap size of the capacitors into a few tens of nanometer. Pourkamali et. al. [21-23] presented a fabrication mechanism to fabricate capacitors with ultra thin nanoscale gap sizes. This fabrication process in its simplest form can be described as first growing a thin layer of thermal oxide on the resonator. Then depositing poly silicon all around the resonator and carve the sensing and actuation electrodes out of it. Then by removing the thin thermally grown oxide, there will be a narrow air gap between the single crystalline silicon resonator body and the poly silicon electrodes. Using this method several disk and block resonators with frequencies in the VHF and UHF range with output impedances as low as 120Ω were fabricated [23]. Although this fabrication method drastically improved the performance of such structures however, first of all it made the fabrication method more difficult. Second, due to the narrow gaps the applied voltage across the capacitors can have the

chance to jump from one side of the capacitors to another side and damage the capacitors. In addition, in case of capacitors with narrow air gaps there is going to be an energy loss mechanism called squeezed film damping; during vibration of the resonator in air, the vibrating resonator body should constantly push away the air inside the gap and loses some energy that lowers its quality factor.

As another category of electrostatic resonators, solid dielectric electrostatic resonators use transduction gaps filled with a solid dielectric material (preferably a high-K dielectric) to take advantage of the larger dielectric coefficients and improve the electromechanical transduction coefficients [24, 25]. The fully solid structure of such devices relax several problems associated with aggressive reduction of the gaps sizes such as stiction and pull-in issues and allows reduction of the dielectric gap sizes to few tens of nanometers (as small as 15nm demonstrated [25]). However, similar to the piezoelectric resonators, such devices require integration and physical contact of dielectric thin films and conductive electrodes with the resonator structures. This defeats some of the main purposes of moving away from piezoelectric transduction. Moreover, large dielectric constant of the very thin dielectrics films results in very large parasitic capacitors associated with such devices.

The more recent work on electrostatic resonators is a homogeneous silicon micromechanical resonator actuated using forces acting on the immobile charge in the depletion region of a symmetrically doped PN diode [26]. This resonator combines the high quality factor (Q) of air-gap transduced resonators with the frequency scaling benefits of internal dielectrically transduced resonators. In addition the fabrication method for such structure is simpler. Hwang et. al. [26] demonstrated a thickness

longitudinal mode micromechanical PN diode single crystalline silicon resonator with Q ~ 18,000 at a resonant frequency of 3.72 GHz. Such doped resonators seem to have the potential for further improvements at high frequencies. It seems that by identifying the loss mechanisms in such structures their performance could be improved [27].

All that said, frequency tuning and compensation of the temperature induced frequency drift are other formidable challenges for both piezoelectric and capacitive resonators. Finally, in order to achieve a strong enough electromechanical transduction and consequently a large signal to noise ratio, both capacitive and piezoelectric resonators require relatively large electrode areas (thousands of μm2) consuming costly real-estate on the chip and limiting the maximum number of devices that can be integrated on a single chip.

1.3.4   Active Transduction Mechanisms

Resonant devices combining electrostatic actuation along with active sensing mechanisms such as field effect [28] and piezoresistive [29-31] have been demonstrated by several researchers. This helps alleviate some of the issues associated with large motional impedances resulting from fully electrostatic transduction. However, fabrication challenges and reliability issues associated with capacitive air-gaps prevail.

1.3.5   Thermal Actuation with Piezoresistive Readout

By passing a current though a conductor, there will be a power loss in the structure that elevates its temperature. The resulted increase in temperature causes an increase in the dimensions of the structure as follows:

$$\Delta L = \alpha L \Delta T \qquad\qquad (1.10)$$

where L, T are the length and temperature of the structure. α is the thermal expansion coefficient which is uniquely determined for the used material. This thermal expansion in the structure can apply a stress into its surroundings and therefore, it can be used as an actuation mechanism for both generating force and displacement in microscale. On the other hand, as a resonator vibrates, there is going to be a change in the resistance of the resonator that can be sensed. Despite the metals in which change in the dimensions of the resonator causes a changes in its electrical resistance ($R = \rho \frac{L}{A}$), in semiconductors there is another effect that mainly determines the change in resistance. This dominant effect is called piezoresistive effect and has a few orders of magnitude higher effect than that of the involved mechanism in metals. The change in resistance due to the piezoresistive effect depends on the applied stress to the structure and can be shown as follows:

$$\Delta R = R\mu_l \Delta L \tag{1.10}$$

Where R, μ_l and L are the resistance, longitudinal piezoresistive coefficient and length of the structure respectively.

Thermal actuation is a well known mechanism that can be implemented conveniently at microscale without fabrication challenges or the need for material integration. In addition, thermal actuators have great properties such as large actuation force, low operating voltage and simplicity of design and integration. On the downside their relatively high power consumption usually makes them an undesirable choice. Furthermore, thermal actuators are generally considered slow actuators only suitable for DC or very low-frequency applications. This is mainly due to the time delay for the temperature of a heating element to raise and generate the expected force. Consequently, although thermally actuated micromechanical resonant devices with frequencies up to

16

9.8MHz have been demonstrated [32-36], there has not been adequate study on the possibility of utilization of thermal actuation for higher frequency applications in the VHF and UHF range. Our recent studies and experiments have shown promising results and plenty of unexplored potentials for thermally actuated high frequency resonators.

Both modeling and experimental measurements suggest that as opposed to the electrostatic and piezoelectric resonators, thermal-piezoresistive resonators perform better as their size is shrunk down and therefore, could be a much stronger candidate for realization of highly integrated nanomechanical signal processing arrays.

2. THERMO-ELECTRO-MECHANICAL MODELING OF THERMALLY ACTUATED RESONATORS WITH PIEZORESISTIVE SENSING

2.1 Operation Concept

Figures 2.1 and 2.2 show the schematic 3D view of the resonator structures used in this research known as I^2-Bulk Acoustic wave Resonator or I^2-BAR [37, 38] (also known as dog-bone resonators [30,31]) and in-plane mode plate resonators respectively [36]. Such structures are a great fit for thermal actuation as they can be actuated simply by applying the actuation voltage between the two support pads on their two sides. The resulting current passes through the structure heating it up by the resulting ohmic loss. The ohmic losses are maximized in the thinner parts. The fluctuating power loss results in a fluctuating temperature gradient and therefore periodic thermal expansion of the extensional beams. The alternating extensional force resulting from the fluctuating temperature in the pillars can actuate the resonators in their in-plane extensional (in I^2-BARs) and flexural (in plate resonators) resonance mode [20]. If the ohmic loss and consequently the resulting temperature fluctuations have the same frequency as the resonant frequency of the resonator, the mechanical vibration amplitude is amplified by the mechanical quality factor (Q) of the resonator. The amplified alternating stress in the pillars leads to increased fluctuations in their electrical resistance (due to the piezo-resistive effect). When biased with a DC voltage, such resistance fluctuations modulate the current passing through the structure resulting in an AC current component known as

the motional current. Since the I^2-BAR structure has the potential to operate at higher frequencies than the plate resonator, this research was mostly concentrated on it.
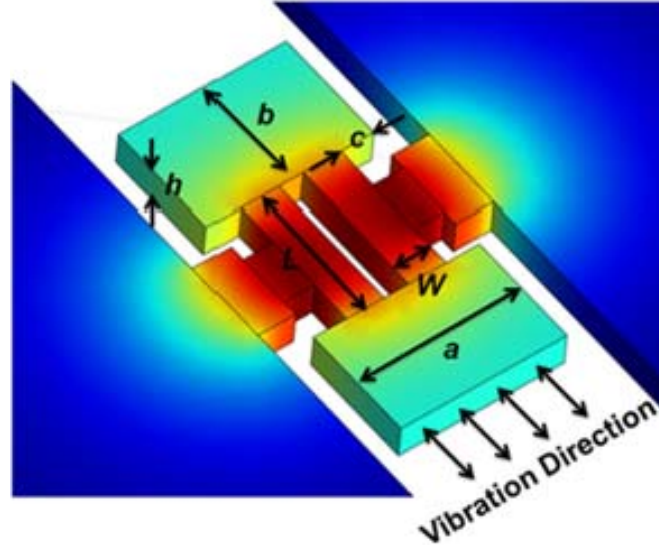
Figure 2.1. 3D view schematic of a thermally actuated I^2-BAR (dog-bone resonator) showing the dimensions and the qualitative distribution of AC temperature fluctuation amplitude (red being the maximum and blue minimum).
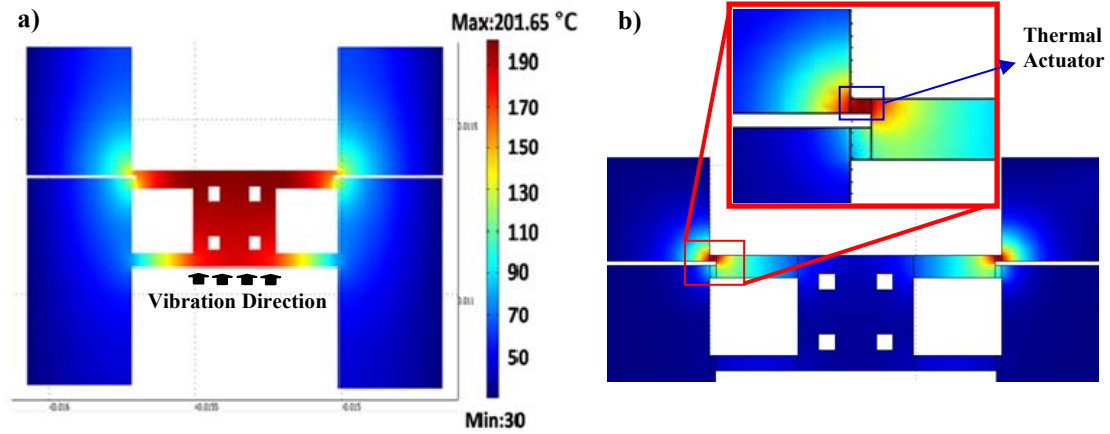
Figure 2.2. COMSOL finite element thermal analysis of plate resonator. a) The color code shows in-plane vibration amplitude of the structure. b) The color code shows static temperature of the structure resulting from the DC bias current. (red being the maximum and blue minimum)

2.2 High Frequency Thermal Actuation

It is hard to imagine a thermal system with small enough thermal time constants to respond to high frequency excitations in the VHF and UHF range. Similar to electrical

19

RC circuits, thermal time constant of a thermal actuator (e.g. a suspended conducting beam) is the product of its thermal capacitance and thermal resistance: $\tau_{th} = R_{th}C_{th}$. Thermal resistance can be calculated using a very similar equation to electrical resistance, i.e. $R_{th} = \rho_{th}L/A$, where ρ_{th} is the thermal resistance of the structural material and L and A are the length and cross-sectional area of the element. Similar to electrical resistance, thermal resistance increases proportionally as the dimensions of the element are scaled down, i.e. if a thermal actuator is scaled by a factor of S, its thermal resistance changes by a factor of S^{-1}. On the other hand, thermal capacitance is proportional to the mass, and therefore the volume of the element and scales by a factor of S^3. Hence, the overall thermal time constant of the element scales by a factor of S^2.

On the other hand, if a mechanical structure is scaled by a factor S, its mechanical resonant frequency (ω_m) changes by a factor of S^{-1}, i.e. its mechanical time constant changes by a factor of S. The overall conclusion is that if the dimensions of a thermally actuated resonant structure are scaled down, its thermal time constant shrinks more than its mechanical time constant. In other words, both thermal and mechanical responses of the system become faster upon scaling the dimensions down, however, the increase in the speed of the thermal response is more (proportional to S^{-2}) than the increase in the mechanical resonant frequency (proportional to S^{-1}). In conclusion, as the structural dimensions are scaled down, the performance of thermally actuated mechanical resonators is expected to improve (more actuation force for the same actuation power) as the thermal response of the system can better catch up with the mechanical vibrations.

2.3   Thermo-Electro-mechanical Modeling

The overall input to output transfer function of thermal-piezoresistive resonators includes a combination of three different domains (sub-systems) of thermal, mechanical and electrical nature as shown in Fig. 2.3. First, the electrical input voltage is turned into a temperature, the temperature is then turned into a mechanical force that causes a mechanical displacement, and finally the mechanical displacement is turned back into an electrical signal (motional current).

Figure 2.3. Block-diagram demonstration of the thermo-electro-mechanical model of the resonator that can be divided into three sub-systems of thermal, mechanical and electrical nature. The electrical input AC voltage causes a temperature fluctuation that is turned into an AC mechanical force and therefore displacement. Finally the mechanical displacement is turned into an electrical signal (motional current) due to the piezoresistive effect.

The first box in Fig. 2.3 is the thermal subsystem that turns the input voltage to a heating power (ohmic loss) and therefore to a temperature fluctuation amplitude (T_{ac}). Due to the square relationship between ohmic power loss and electrical voltage (or current), application of an actuation voltage with frequency of f_a results in an AC ohmic loss component with frequency of $2f_a$. In order to have the same frequency as the input AC actuation voltage for the thermal actuation force, a combination of AC and DC voltages (V_{dc} and v_{ac}) needs to be applied between the two pads of the resonators. The resulting power loss component at the same frequency as v_{ac} will then be:

$$P_{ac} = \frac{2V_{dc}v_{ac}}{R_A} \hspace{4cm} (2.1)$$

where R_A is the electrical resistance of the actuator elements (extensional pillars in I^2-BARs) and V_{dc} and v_{ac} are the applied DC and AC actuation voltages respectively.

Figure 2.4a shows the equivalent electrical circuit of the thermal subsystem. The equivalent circuit consists of a current source representing the heating power along with a capacitance (C_{th}) and a resistance (R_{th}) representing the effective thermal capacitance and thermal resistance of the thermal actuators respectively. The resulting voltage across the parallel RC combination (T_{ac}) represents the temperature fluctuation amplitude and the transfer function giving the temperature fluctuation amplitude versus the input voltage can be derived as follows:

$$H_{th}(s) = \frac{T_{ac}}{v_{ac}} = \frac{2V_{dc}R_{th}}{R_A\left(1 + R_{th}C_{th}s\right)} \tag{2.2}$$

where $s = j\omega$ is the Laplace transform parameter.

The alternating mechanical force amplitude due to thermal stress caused by the fluctuating temperature is:

$$F = 2\alpha T_{ac}AE \tag{2.3}$$

where α is the thermal expansion coefficient of the thermal actuator structural material, A is the thermal actuator cross sectional area, and E is the Young's modulus of the thermal actuator along its length. The coefficient "2" has been added since there are two actuator beams in each I^2-BAR contributing to the actuation force.

In the equivalent electrical circuit of the mechanical subsystem shown in Fig. 2.4b, the voltage source represents the thermally generated mechanical force, and the inductor, capacitor, and resistor represent the effective mechanical mass, stiffness, and

damping of the resonator respectively. Consequently, current represents velocity and charge ($Q = \int i.dt$) represents displacement. Therefore:

$$X_{th}(s) = Q(s) = \frac{i(s)}{s} = \frac{F}{\left(Ms^2 + bs + K\right)} \tag{2.4}$$

where M, K and b are the effective mechanical mass, spring constant and damping coefficient of the resonant structure, and X_{th} is the elongation amplitude of the thermal actuators (resonator vibration amplitude). Replacing the actuation force from Eq. 2.3 into Eq. 2.4 results in the following transfer function for the mechanical subsystem:

$$H_m(s) = \frac{X_{th}}{T_{ac}}(s) = \frac{2\alpha AE}{(Ms^2 + bs + K)} \tag{2.5}$$

The undamped mechanical resonance frequency of the resonator is $\omega_0 = \sqrt{K/M}$ and its intrinsic quality factor is $Q = M\omega_0/b$. At the resonance frequency, the mechanical stiffness and mass in the mechanical transfer function cancel each other out and H_m is simplified to:

$$H_{m,res} = \frac{X_{th}}{T_{ac}}(s)\bigg|_{s=j\omega_0} = \frac{2\alpha AEQ}{Mj\omega_0^2} = \frac{2\alpha AEQ}{jK} \tag{2.6}$$

where $j = \sqrt{-1}$ showing that the mechanical displacement is lagging behind the temperature (and force) fluctuations by 90°, which is always the case for linear mechanical resonators at resonance.

The vibration amplitude, which is the output of the mechanical subsystem, causes a change in the resistivity of the thermal actuators due to the piezoresistive effect:

$$r_{ac} = R_A \pi_l E \frac{X_{th}}{L} \tag{2.7}$$

where π_l is the longitudinal piezoresistive coefficient of the actuator beams, r_{ac} is the amplitude of the actuator resistance fluctuations, and L is the length of the thermal actuators. Since a DC bias voltage is applied to the thermal actuators, this change in resistance modulates the current in the actuators:

$$i_m = \frac{r_{ac}}{R_A} I_{dc}$$
(2.8)

Therefore, the transfer function of the electrical subsystem (Fig. 2.4c) will be as follows:

$$H_e = \frac{i_m}{X_{th}} = \frac{\pi_l E I_{dc}}{L}$$
(2.9)
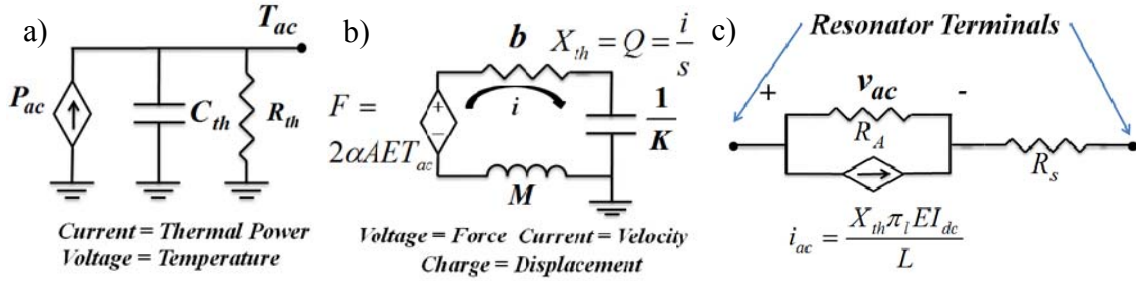
Figure 2.4. a) Equivalent electrical circuit for the thermal sub-systems; b) Equivalent electrical circuit for the mechanical sub-systems; c) Equivalent electrical circuit for the electrical sub-system.

R_s in Fig. 2.4c represents the all parasitic electrical resistances in series with the actuator resistance which mainly includes resistance of resonator support beams.

Finally, the overall transfer function that relates the AC motional current (output current) to the AC input voltage is the product of the three transfer functions of the thermal, mechanical and electrical subsystems:

$$H_T = \frac{i_m}{v_{ac}} = H_{th} H_m H_e = \frac{4\alpha A E^2 I_{dc}^2 \pi_l}{L(Ms^2 + bs + K)} \frac{R_{th}}{(1 + R_{th} C_{th} s)}$$
(2.10)

which simplifies as following at resonance frequency:

24

$$H_T\big|_{s=j\omega_0} = \frac{4\alpha E^2 \pi_l QAI_{dc}^2}{KLj} \frac{R_{th}}{\left(1 + R_{th}C_{th}s\right)}$$ (2.11)

Furthermore, for physical dimensions in the micro and even nanoscale, the thermal time constant is typically much larger than the mechanical time constant of the structure. In other words, it takes a much longer than the mechanical resonance period of the structure for the temperature of the actuators to reach its steady state value and stabilize. Therefore, $\omega_0 >> \tau_{th}^{-1} = (R_{th}C_{th})^{-1}$, which simplifies H_T to:

$$H_T\big|_{s=j\omega_0} = g_m = 4\alpha E^2 \pi_l Q \frac{AI_{dc}^2}{KLC_{th}\omega_0}$$ (2.12)

Knowing that $K = 2EA/L$, Eq. 2.12 can be further simplified to:

$$g_m = 2\alpha E \pi_l Q \frac{I_{dc}^2}{C_{th}\omega_0}$$ (2.13)

The transfer function in Eqs. 2.12 and 2.13 can be referred to as small signal voltage to current gain, or motional conductance (g_m) of the resonator at its resonance frequency, which is one of the most important parameters of a thermal-piezoresistive resonator when utilized as an electronic circuit component.

2.3.1   Resonator Equivalent Electrical Circuit

For the single-port I^2-BAR resonators used in this work, where the resonator extensional pillars acting as thermal actuators also act as piezoresistive sensors, the physical resistance of the resonator connects the input and output of the devices. Therefore, the equivalent electrical circuit includes a resistance $R_A + R_s$ connected between the two terminals of the resonator, which is the overall resistance in the current path between the two pads of the resonator. In parallel to the static resistance of the actuators,

25

there is a series RLC combination that represents the mechanical resonant behavior of the structure. The value of R_m in the RLC has to be set so that at resonance, a motional current of $i_m = g_m.v_{ac} = v_{ac}/R_m$ is added to the feedthrough current passing through R_A. Therefore, $R_m = g_m^{-1}$ and L_m and C_m values can be calculated based on the value of R_m as shown in Fig. 2.5 according to the resonance frequency and quality factor of the resonator.
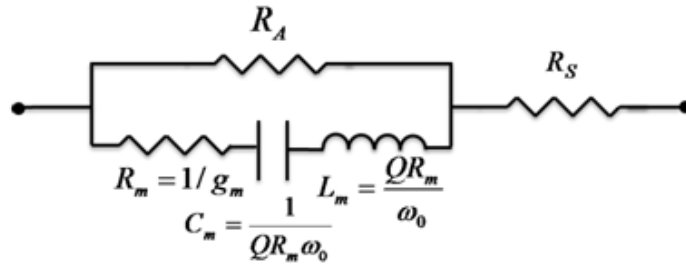
Figure 2.5. Overall equivalent electrical circuit for one-port thermally actuated resonators with piezo-resistive readout.

2.3.2   Calculation of Actuator Thermal Capacitance

To calculate the g_m of a thermal-piezoresistive I²-BAR, which is the most important parameter to be extracted from the model, using Eq. 2.12, all the parameters except the effective thermal capacitance of the actuators (C_{th}) are known for every set of resonator dimensions. Due to the distributed nature of the thermal parameters including thermal generator (resistance of the structure), thermal capacitance and thermal conductance, analytical derivation of the effective equivalent values for the thermal parameters could be quite complicated. Therefore, COMSOL finite element analysis was used to analyze the AC thermal behavior of the actuators and calculate the fluctuating temperature amplitude (T_{ac}) at different points along the length of the actuator beams

(Fig. 2.6). The mean value of the small signal temperature amplitudes at different points along the actuators is the effective temperature fluctuation amplitude for the actuator.

Again using the typically valid assumption of $\omega_0 >> \tau_{th}^{-1} = (R_{th}C_{th})^{-1}$, C_{th} can be calculated using the value of (T_{ac}) obtained from the finite element analysis and a rearranged and simplified version of Eq. 2.2:

$$C_{th} = \frac{2I_{dc}i_{ac}R_A}{T_{ac}\omega_m} \tag{2.14}$$

Figure 2.6 shows the COMSOL finite element transient thermal analysis of a 61MHz I^2-BAR. In this model by applying a combination of DC and AC currents of 60mA and 5mA, the DC temperature profile of the resonator as well as the AC temperature amplitude at different points along the length of the thermal actuators were obtained. Figure 2.5 shows that in order to actuate such a resonator in its in-plane resonant mode only an AC temperature with an amplitude of about 0.01 °C in needed.
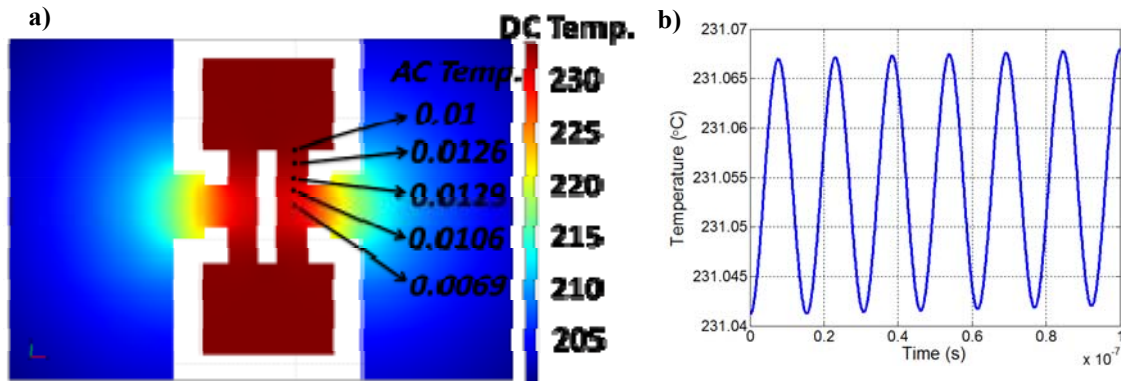
Figure 2.6. a) COMSOL finite element thermal analysis a 61MHz I^2-BAR by applying DC and AC currents of 60mA and 5mA respectively. The color code shows static temperature of the structure resulting from the DC bias current, and the numbers show temperature fluctuation amplitude (T_{ac}) at different points along the actuator caused by the AC excitation; b) time domain temperature variations of a point in the middle of the thermal actuator showing Tac of ~0.01°C

2.4   Thermal Capacitance Investigation

In order to further investigate the effect of dimensions of the thermal actuators on their effective thermal capacitance, plate thermal resonators shown in Fig 2.2 were used. It was desired to perform this modeling for different resonators with different thermal actuator dimensions. To verify the validity of the assumption that actuation frequency is much higher than the thermal natural frequency of the actuators ($\omega_0 >> \tau_{th}^{-1}$), COMSOL thermal transient analysis was performed on the resonator of Fig. 2.2. The thermal time constant of the actuator in this structure was found by applying a DC bias current to the actuator and monitoring the resulting temperature increase over time. The thermal time constant was calculated by finding the time needed for the thermal actuator temperature to reach 63% of its final value (similar behavior as an RC electrical circuit). For the resonator in Fig. 2.2 τ_{th} was found to be *6.2×10⁻⁴ s*, i.e. τ_{th}^{-1}=*1.61 kHz*, while ω_0 = *2π×700 kHz*. Since there is a huge difference (close to three orders of magnitude) between the thermal and mechanical frequency response, we can safely assume that this assumption holds for all the resonators in this research.

Values of C_{th} were calculated for several actuator dimensions embedded in the resonator structure of Fig. 2.2. Both length and width of the two thermal actuator beams were changed several times to cover a broad range of dimensions, while the structure height (15μm) and actuation current were kept constant. Figure 2.7 shows the calculated average T_{ac} for different thermal actuator dimensions. Since Eq. 2.14 is only valid if $\omega_0 >> \tau_{th}^{-1}$, a very high actuation frequency of 200MHz was used in the simulations.

As expected based on Eq. 2.14, increasing the actuator length increases both thermal capacitance of the element as well as the ohmic AC power generated in the actuator proportionally (due to higher resistance) and therefore does not lead to
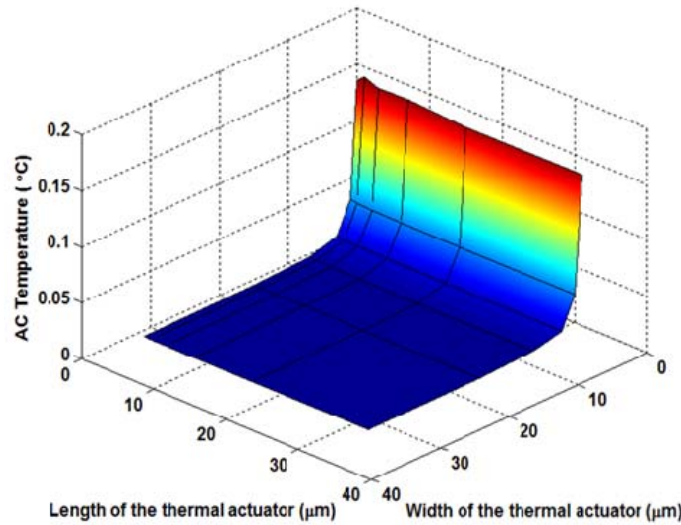
Figure 2.7. Average temperature fluctuation amplitude with respect to the length and width of the thermal actuators. All the thermal actuators have the same height of 15μm with material resistivity of 0.014 Ω.cm. A combination of DC bias (50mA) and AC actuation (5mA in 200MHz) currents has been applied to the plate resonator in all cases. A 3D electro-thermal simulation using COMSOL transient analysis was used to simulate the small signal temperatures response. The AC temperature increases by increasing the length and decreasing the width of thermal actuator.

significant change in the amplitude of T_{ac}. Decreasing the actuator width on the other hand increases the power generation while at the same time reduces the thermal capacitance of the actuator and therefore results in a sharp increase in the small signal temperature amplitude.

A more informative parameter, that can be considered an indication of thermal actuation efficiency, is the temperature fluctuation amplitude per power consumption which is shown in Fig. 2.8. According to this graph, by reduction of both length or width of the thermal actuator, higher temperature fluctuation amplitudes can be achieved with the same power consumption.

Finally, figure 2.9 shows the calculated thermal capacitances for a wide range of different actuator lengths and widths using the calculated temperature fluctuation amplitudes from COMSOL simulation and Eq. 2.14. Figure 2.9 shows that the effective thermal capacitance of the actuators is proportional to their volume.
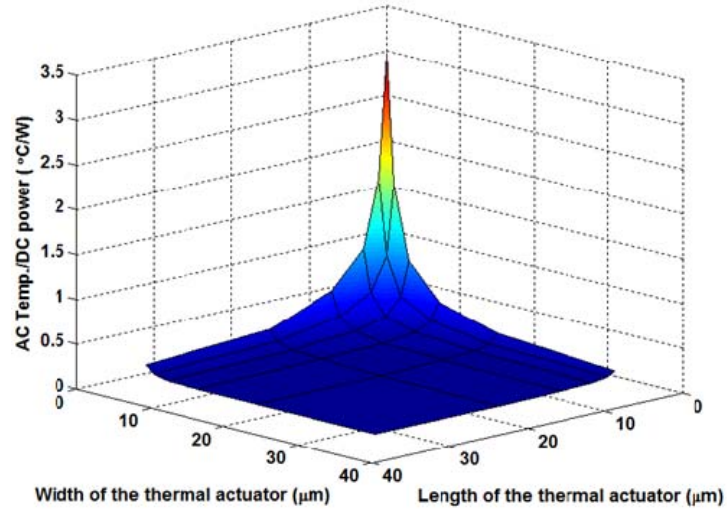
Figure 2.8. The ratio of the temperature fluctuation amplitude over the DC power consumption as a function of the width and length of the thermal actuator. It clearly shows that as the actuator dimensions shrink down, more temperature fluctuation amplitude can be achieved with the same power consumption.
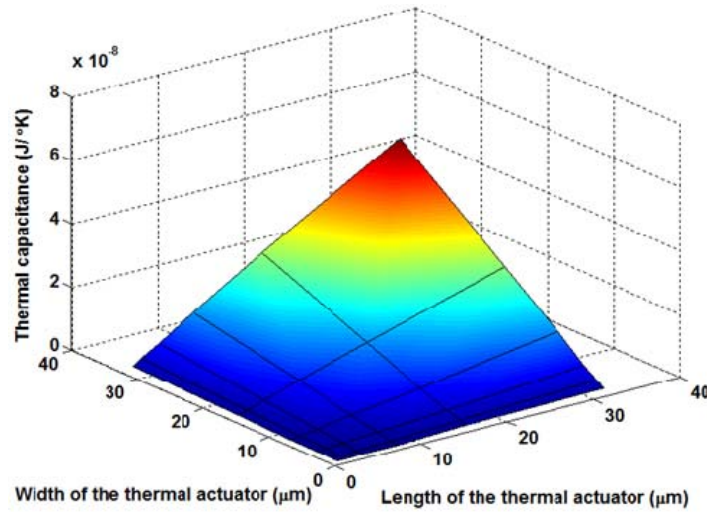
Figure 2.9. Actuator thermal capacitance as a function of the length and width of the actuator.

The 2D plots of Fig. 2.10 include different cross-sectional views of the 3D plot in Fig. 2.9 showing a very linear dependency between the effective thermal capacitance and both actuator length and width.

If the actuator is treated as a lumped element, there will also be a linear dependency between the actuator thermal capacitance and its volume (i.e, each of its dimensions), therefore the effective thermal capacitance should be proportional to the lumped-element thermal capacitances of the actuators (C_{LE}) with a ratio β:

$$C_{th} = \beta C_{LE} \tag{2.15}$$

Having the mass and the specific heat capacity of silicon, the lumped-element thermal capacitance of an actuator beam can be calculated as:

$$C_{LE} = M_A C_H = \rho L_A W_A H C_H \tag{2.16}$$

where C_H is the heat capacity of silicon (700 J/Kg.K), M_A is the actuator mass, and ρ, L_A, W_A, and H are the density, length width, and height of the actuator beam respectively.
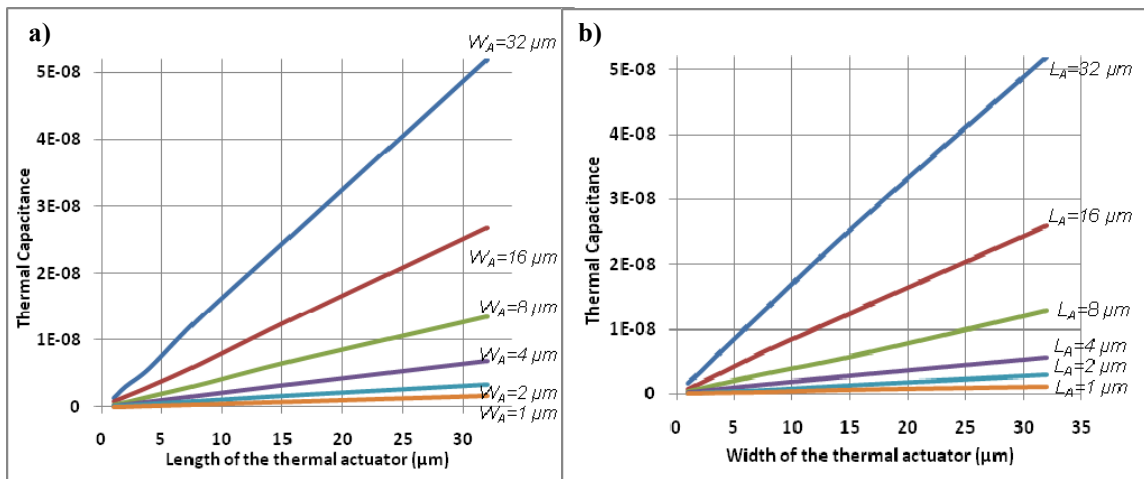
Figure 2.10. Effective actuator thermal capacitance with respect to a) the length of the thermal actuator while keeping its width constant at 1, 2, 4, 8, 16 and 32 μm b) to the width of the thermal actuator while keeping its length constant at 1, 2, 4, 8, 16 and 32 μm.

Figure 2.11 Shows the ratio of the calculated lumped-element thermal capacity over the effective thermal capacity found from the COMSOL model versus the aspect ratio of the actuator beam (L_A/W_A) for different actuator widths.

Despite minor variations and nonlinearity of the results, especially at lower actuator aspect ratios, for all the thermal actuators the calculated thermal capacitances from Eq. 2.16 are almost 0.9-0.98 of the effective thermal capacitances calculated by finite element analysis. For larger aspect ratios all the curves in Fig. 2.10 seem to converge to 0.92. Therefore, the value of β, with a good approximation, is $(0.92)-1 = 1.086$. This information can be used to directly calculate the effective thermal capacitance of any thermal actuator beam using its physical dimensions without having to go through the finite element analysis.
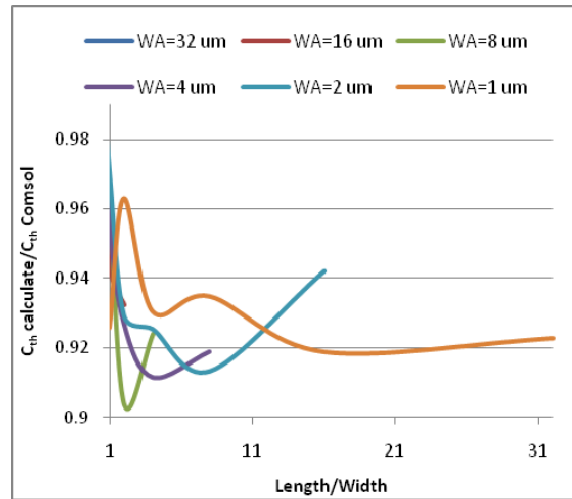
Figure 2.11. The ratio of the calculated lumped-element thermal capacitances using Eq. 2.16 over the effective thermal capacitance of the actuator calculated by COMSOL finite element analysis versus the aspect ratio of the actuator beams (length/width) showing a relatively constant ratio of 0.9-0.98.

3. FABRICATION AND CHARACTERIZATION OF HIGH FREQUENCY THERMALLY ACTUATED RESONATORS WITH PIEZORESISTIVE READOUT

3.1   Resonator Fabrication

A single mask process was used to fabricate the resonators on low resistivity SOI substrates [38, 41]. The fabrication process starts by thermally growing a thin (~200nm) layer of silicon dioxide on the device layer that will serve as a hard mask for silicon etching (Fig. 3.1). The silicon dioxide layer is patterned to define the resonator structures. The structures are then carved into the SOI device layer all the way down to the buffer oxide layer (BOX) by plasma etching. Finally, the structures are released by etching the underlying BOX layer in hydrofluoric acid (HF). At the same time the remaining oxide mask on top of the structures is also etched away.

a) Starting SOI Substrate, Grow thin thermal oxide

b) Pattern Oxide, Silicon Wet Anisotropic Etch in KOH

c) HF release
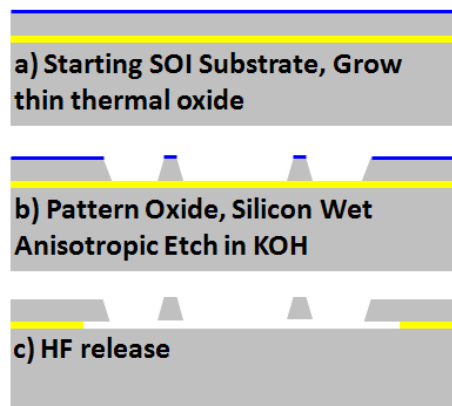
Figure 3.1. Process flow used for fabrication of the resonators.

A wide variety of I^2-BAR structures with different dimensions were fabricated on SOI substrates with different device layer thickness, resistivity and doping type. Figure 3.2 shows the SEM view of a few of the fabricated resonators. For some of the devices the actuator beams were thinned down in order to minimize resonator power consumption. By performing a number of consecutive thermal oxidation and oxide removal steps, submicron actuator width were achieved (Fig. 3.2c).

3.2   Electrical Connections for Operation in One-Port Measurement Configuration

Since the resonant structures in this work are one-port devices comprised of a monolithic piece of crystalline silicon, they were tested in a one-port configuration. In a one-port configuration the extensional beams act simultaneously as both thermal actuators and piezo-resistive sensors. Figure 3.2d shows the schematic diagram of the electrical connections required for operation of the resonator in the one-port configuration along with COMSOL modal analysis results for the 61MHz resonator shown in Fig. 3.2b in its fundamental in-plane extensional mode. In this configuration a combination of a DC bias current and an AC actuation voltage are applied between the two terminals of the resonator. Large bypass capacitors and bias resistors are used to isolate the AC and DC sources.
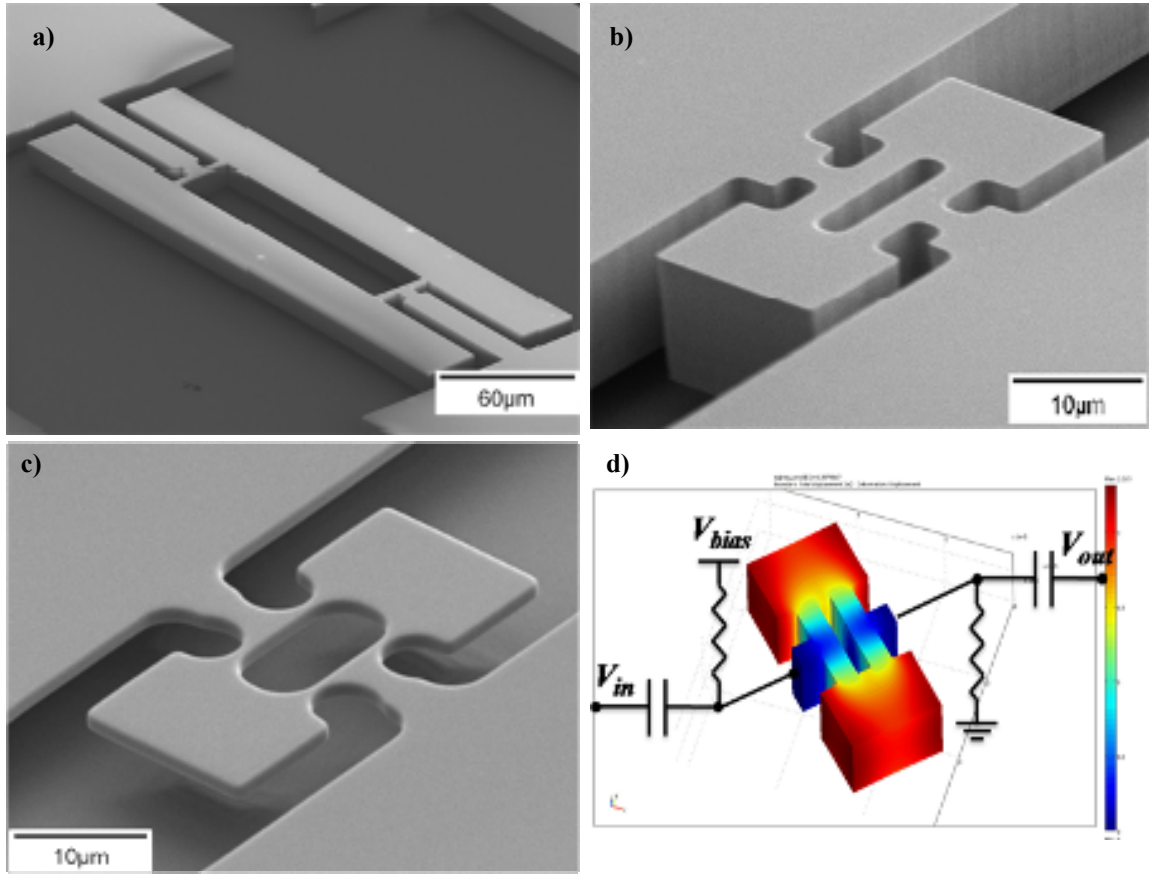
Figure 3.2. a) a SEM view of a 7.9MHz 15µm thick I^2-BAR fabricated on a low resistivity p-type substrate; b) a SEM view of a 61MHz 15µm thick I^2-BAR fabricated on a low resistivity p-type substrate; c) a SEM view of a 41MHz 3µm thick I^2-BAR fabricated on a low resistivity n-type substrate followed by thermal oxidation to thin down its thermal actuator beams. All devices are fabricated on 100 SOI substrates. The first two resonators are oriented along the 110 crystalline orientation while the third resonators is aligned to the 100 crystalline orientation; d) Schematic diagram showing the electrical connections for operation of an I^2-BAR in a one port configuration along with the COMSOL modal analysis results, showing the in-plane fundamental extensional resonance mode for the resonator of Fig. 6b. The resonator dimensions are $a=22µm, b=15µm, c=4.4µm, L=18µm, W=5µm$ showing a frequency of 60.77MHz. Red and blue colors show locations with the largest and smallest vibration amplitudes respectively.

3.3   Processing the Frequency Response Measurement Data

Due to the very low resistance of the actuator beams in the order of a few Ohms, only a small portion of the applied voltage by the network analyzer through its 50Ω terminations will fall across the actuators resulting in excessive attenuation in the transmission spectra. Therefore, the effect of the bias resistors, the 50Ω terminations of the network analyzer, as well as the parasitic resistances associated with the resonator

structures should be de-embedded from the measured data before comparing them to the theoretically calculated values [38, 42].

3.3.1   Finding the Motional Conductance from the Peak Transmission Level

Figure 3.3 shows the electrical small signal model of the resonator along with bias resistors and the network analyzer terminations. The resonator motional conductance, which is the parameter to be extracted from the measurements is $g_m = i_m/v_{ac}$, where v_{ac} is the AC voltage amplitude across the resonator actuators and i_m is the motional current of the resonator. Eq. 3.1 gives the resonator output voltage as a function of the resonator motional current:

$$v_o = \frac{R_T.R_A.i_m}{2R_T+R_A + R_s}$$

(3.1)

where R_T is the parallel combination of the bias resistor (R_{bias}) and the network analyzer 50Ω impedance, R_A is the resonator actuator resistance (including both actuators), and R_s is the internal parasitic resistance of the resonator which is the resistance between the two resonator pads not including the actuator resistance. R_s mainly consists of the support beam resistances. Eq. 3.1 can be rearranged as:

$$i_m = \frac{v_o.(2R_T + R_A + R_s)}{R_T.R_A}$$

(3.2)

On the other hand, the voltage across the resonator actuators (v_{ac}) can be calculated by dividing the thevenin equivalent voltage of the source voltage ($v_s.R_T/50$) between the series combination of $2R_T$, R_s, and R_A.

$$v_{ac} = \frac{R_T.R_A}{2R_T + R_A + R_s}.\frac{v_s}{50}$$

(3.3)

Combining Eq.s 3.2 and 3.3 leads to the motional conductance of the resonator as:

36

$$g_m = \frac{i_m}{v_{ac}} = \frac{50.(2R_T + R_A + R_s)^2}{R_T^2.R_A^2} \cdot \frac{v_o}{v_s} \qquad (3.4)$$

The transmission value in dB measured by the network analyzer is:

$$T_{dB} = 20\log\frac{2v_0}{v_s} \qquad (3.5)$$

Therefore:

$$g_m = \frac{i_m}{v_{ac}} = \frac{25.(2R_T + R_A + R_s)^2}{R_T^2.R_A^2} \cdot 10^{\frac{T_{dB}}{20}} \qquad (3.6)$$
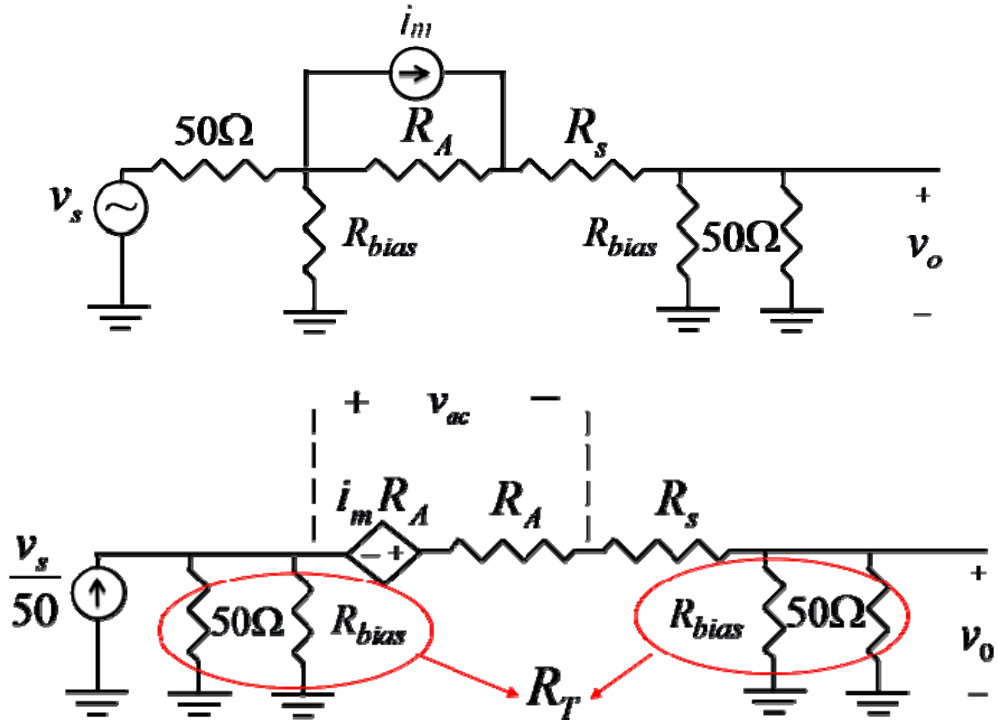
Figure 3.3. Electrical small-signal model used to extract the motional conductance of the resonators by de-embedding the effect of the bias resistors as well as the resistance of the resonator support beams.

3.3.2 Obtaining the Motional Conductance Plot

Figure 3.4 shows a frequency response of the resonator shown in Fig. 3.2b upon the application of 80mA of DC current under vacuum directly taken form a network

analyzer. Due to the existence of a physical resistance between the input and output terminals of the network analyzer, the signal level is pretty high. Although it is possible to determine the value of motional conductance using the method mentioned in the last section, however, in order to be able to measure the quality factor of the resonator, change in the motional conductance of the resonator with respect to frequency should be calculated. Then, since the motional conductance is proportional to the vibration amplitude, the quality factor can be easily calculated.
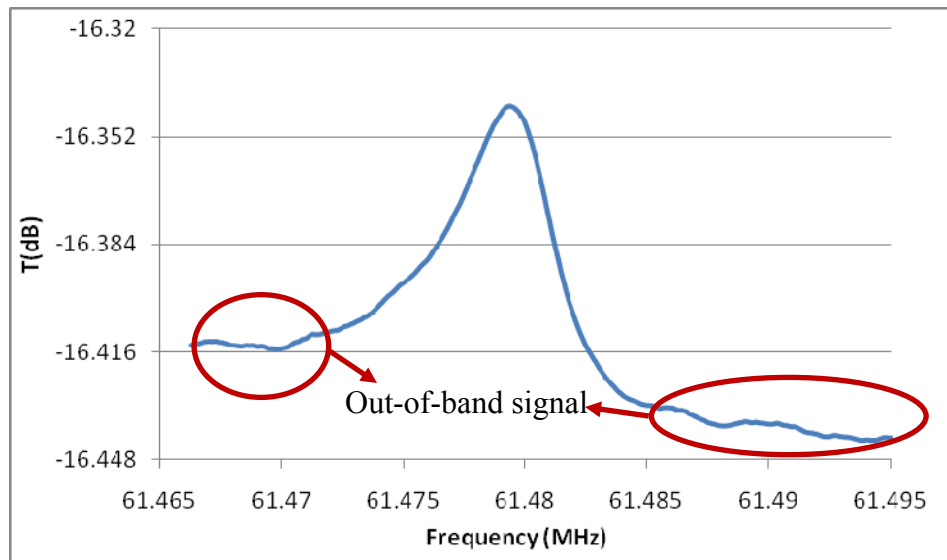
Figure 3.4. Measured frequency response of the thermally actuated 61MHz resonator of Fig. 3.1b by applying 80mA of bias current under vacuum pressure.

In order to convert the data in Fig. 3.4 into motional conductance values, schematic model of Fig. 3.5 is used. In this electrical equivalent model, the resistance of the supports (R_s) has been neglected due to its relatively low value. It is also assumed that the two bias resistances are greater than the internal 50Ω impedances of the network analyzer terminals. Therefore with a good approximation $R_T = 50 \ \Omega$. Therefore the output voltage v_o can be found as a function of the input voltage (v_s):

$$\frac{v_o}{v_s} = \frac{1}{50} \cdot \frac{R_T}{2R_T + \dfrac{1}{G_A + G_M}}$$ (3.7)
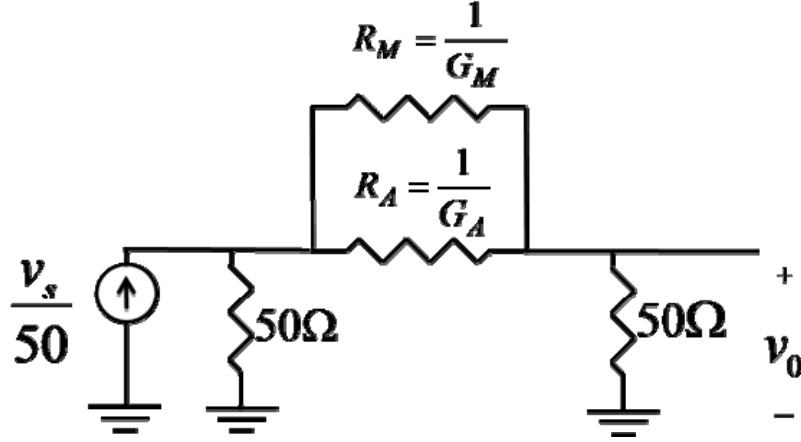
Figure 3.5. Electrical small-signal model of a thermal-piezoresistive resonator at resonance. It is used to calculate the plot showing the motional conductance of the resonator versus frequency.

From this equation the sum of $G_M=1/R_M$ and $G_A=1/R_A$ can be found. At frequencies far from the resonance frequency of the structure G_M is zero and G_A can be calculated using the following equation:

$$G_A = \frac{-1}{2R_T - \dfrac{2R_T}{10^{\frac{T_{dB_{Out-of-Band}}}{20}}}}$$ (3.8)

Where $T_{dB_{Out-of-Band}}$ is the averaged transmission value measured by the network analyzer at frequencies away from the resonance frequency of the resonator (out-of-band range). Figure 3.4 shows this out-of-band range for the frequency response of the 61MHz resonator. Having the value for G_A, G_M can be calculated as follows:

$$G_M = \frac{-1}{2R_T - \dfrac{2R_T}{10^{\frac{T_{dB}}{20}}}} - G_A$$ (3.9)

Where T_{dB} is the transmission data taken from the network analyzer at different frequencies. At the end the G_M values should be converted to dB values and be plotted versus frequency to find the quality factor. Figure 3.6 shows the obtained motional conductance values for the transmission frequency response of Fig. 3.4.
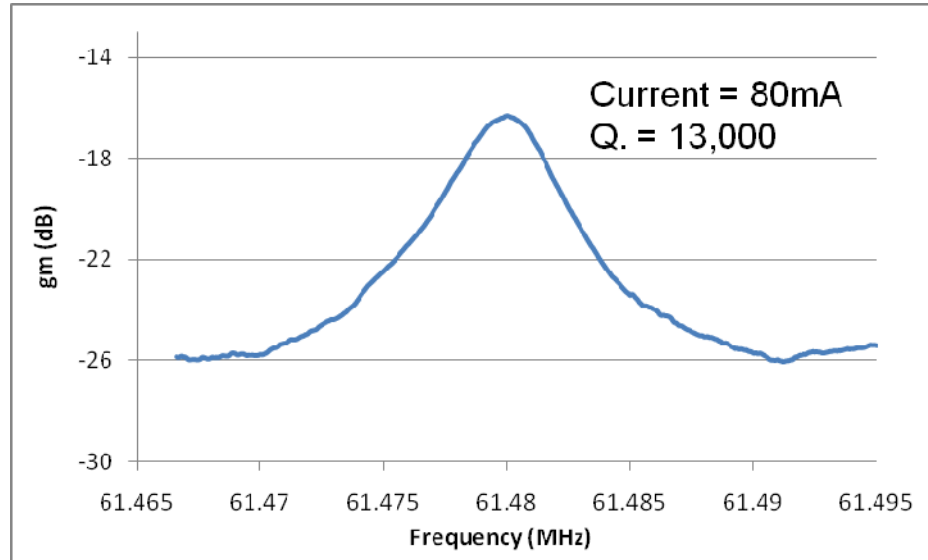
Figure 3.6. Obtained frequency response of the thermally actuated 61MHz resonator of Fig. 3.1b upon application of 80mA of DC bias current.. It shows the motional conductance values in dB at different frequencies calculated from the measured frequency response of Fig. 3.4.

3.4 Measurement Results

Figure 3.7 shows measurement results of the de-embedded motional conductance values obtained from the 61MHz resonator in Fig. 3.1b. For this resonator quality factors ranging from 12,000-14,000 were measured under vacuum. The quality factor dropped to 6,000-8,000 under atmospheric pressure. A large frequency tuning range can be achieved for such resonators by changing their DC bias currents. This is mainly due to the raising temperature of the resonating body, especially its extensional beams that provide most of the structural stiffness in the in-plane extensional mode. As expected, as the DC bias

current increases the output signal level increases while due to the higher static temperature and softening of the structural material, the resonant frequency decreases.
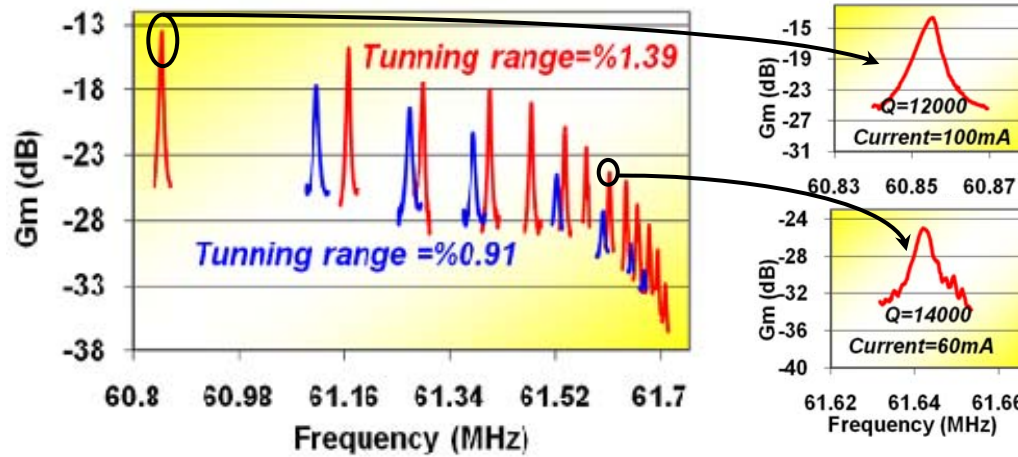
Figure 3.7. Measured frequency response of the thermally actuated 61MHz resonator of Fig. 3.1b with different bias currents. Red and blue plots refer to vacuum and Air testing conditions respectively. Current range is 45-100mA in vacuum and 55-100mA in air.
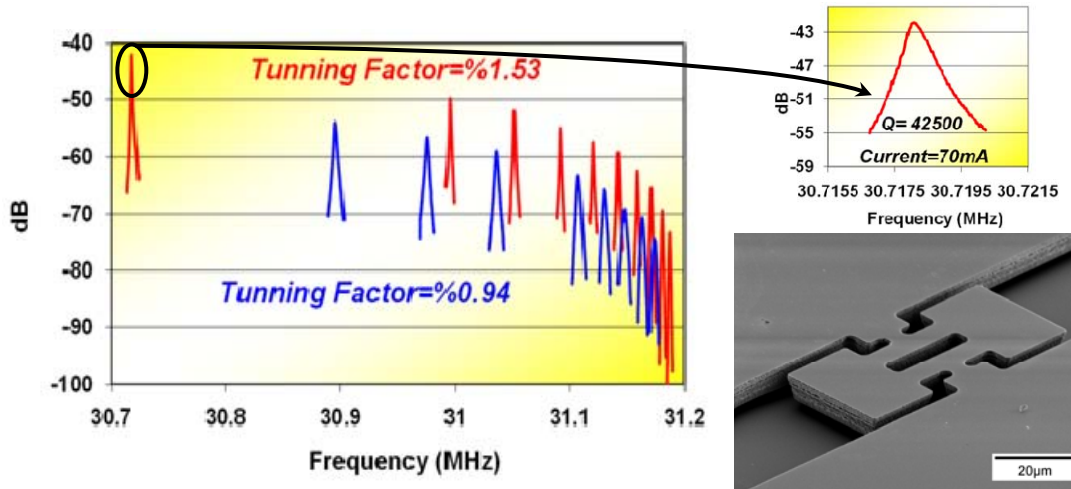
Figure 3.8. Measured frequency response and SEM view of a thermally actuated 30.5MHz resonator with different bias currents. Red and blue plots refer to vacuum and Air testing conditions respectively. Current range is 10-70mA in vacuum and 20-70mA in air.

Although operating at high frequencies unprecedented for thermally actuated resonators, and high quality factors, the large current requirement and power consumptions for the resonators in Fig.s 3.7 and 3.8 are major drawback against using

41

such as electronic components. Therefore, for a number of fabricated resonators the actuator widths were reduced by oxidizing them in order to consume a thin layer of silicon on their surfaces including on their actuator beams. After removal of the grown oxide layer, a thinner extensional beam is left. This sequence was repeated a few times for some of the resonators until submicron beam widths were achieved.

Figure 3.9 shows some of the frequency responses measured for one of such devices with resonant frequency of 30.5MHz and ~750nm wide actuators. As opposed to the 61MHz resonator of Fig. 3.7 that required at least 40mA of DC bias to exhibit a measurable resonance peak, a resonance peak was detected for this resonator with currents as low as 43μA translating into DC power consumptions as low as a 3.6μW. At the DC bias current of 720μA (DC power of 1mW), motional conductance of 44μA/V was measured for this resonator. Maximum currents tolerable for such narrow actuator beams are in the few mA range leading to motional conductances as high as 0.23mA/V in air with Q of 9,200. According to the derived model, much higher motional conductances can be achieved by consuming the same amount of power using lower resistivity structural material allowing higher bias currents. This resonator was fabricated on an N-type SOI device layer with resistivity of ~0.01Ω.cm. Therefore, another one to two orders of magnitude improvement are expected to be achievable using lower resistivity substrates. Figure 3.10 shows a comparison between the measured and calculated motional conductances values in both air and vacuum for the 30.5MHz resonator of Fig. 3.9.
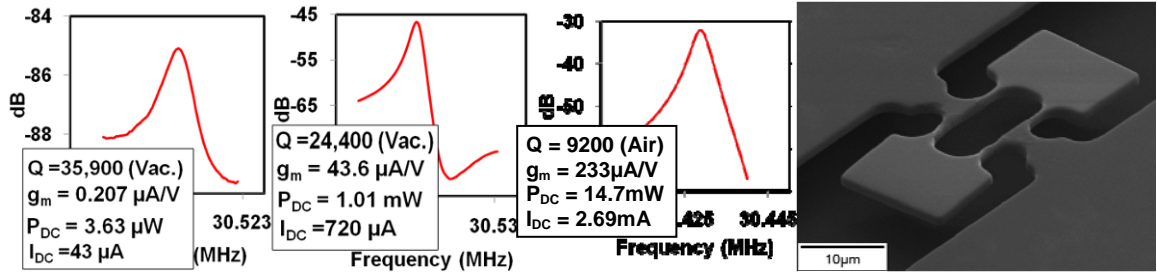
Figure 3.9. SEM view and measurement results for a 3µm thick 30.5MHz dog-bone resonator. Due to its very narrow (750nm wide) actuator beams, clear resonant peaks with motional conductance in the tens of µA/V have been measured for this resonator with sub-mA DC bias currents (sub-mW power consumption).
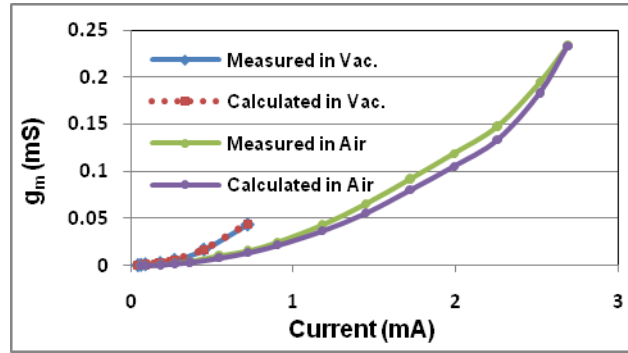
Figure 3.10. Measured and calculated values of motional conductance versus bias current in both air and vacuum for the 30.5MHz resonator shown in Fig. 3.9 showing an acceptable agreement between the recordings and the model predictions. Measured Q values are used to find the calculated values.

In order to examine and verify the validity of the derived model, several measurement results for I^2-BAR resonators with different dimensions were compared to the values calculated by the model. Table 3.1 presents some of the measured data for different resonators under different bias current and pressure conditions. Considering the several possible sources of error, there is a good agreement between the measured and calculated gm values for most of the data points. Some of the major sources of error include uncertainty in resistivity and other physical properties of the structural material (e.g. piezoresistive coefficient) as well as changes in such properties at elevated temperatures, uncertainty in structural dimensions and rounded corners and concave shape of the actuator beams (especially for smaller devices), and errors in extraction of

the motional conductance values from the logarithmic measured transmission data (from the network analyzer) and de-embedding the effect of the parasitic resistances.

Table 3-1 Measurement and calculation results for different thermal-piezoresistive I²-BARs.

Scale Factor	Resonator Dimensions (μm)						Measured Parameters					Calculated Parameters				
	a	b	c	L	W	H(μm) Resistivity (Ω.cm)	Current (mA)	Q. Factor	Freq. (MHz)	g_m (mA/V)	Power (mW)	R_A (Ω)	C_{th} (nJ/°K)	g_m (mA/V)	F.M./Q. (10^{-6} V^{-2})	Power (mW) @ g_m=1 (mA/V)
1X	274	30	67	31	4	10	16.8	29000	7.94	2.53	6.00	5.81	2.02	2.93	16.8	2.05
							40.5	37000	7.75	27.0	34.9			23.3	18.1	1.49
0.7X	193	21	47	22	2.7	1.5×10^{-3}	26	24000	10.87	10.2	16.3	6.11	0.968	9.12	23.2	1.79
							30.5	16000	10.63	10.9	22.5			8.95	24.8	2.52
0.5X	144	16	35	16	2		21.3	12000	13.94	5.80	10.8	6.00	0.521	4.83	37.0	2.25
							30.2	7000	13.78	10.0	21.8			5.86	38.3	3.73
1X	80	53	16	64	17.4	10	55	28500	15.89	2.18	63.5	11.0	18.1	1.56	0.86	40.6
							80	29000	15.65	8.08	134			3.52	0.90	38.2
							50	10800	15.91	0.60	52.5			0.49	0.86	107
							90	10900	15.73	4.29	170			1.65	0.89	103
0.5X	39	25	8.5	32	8.5	6×10^{-3}	20	29000	31.18	0.319	9.09	11.3	4.43	0.48	1.82	18.9
							65	38500	30.72	11.3	96.0			7.04	1.90	13.6
							30	11000	31.17	0.271	20.4			0.41	1.82	49.8
							70	12000	30.9	2.88	111			2.50	1.87	44.5
NA	18.5	11.5	4.4	14.9	0.77	3	0.043	36000	30.52	2.07×10^{-4}	1.71×10^{-3}	645	5.61×10^{-2}	2.30×10^{-4}	3.73	7.44
							0.72	24400	30.52	4.36×10^{-2}	0.481			4.38×10^{-2}	3.73	10.9
							0.062	13250	30.52	1.42×10^{-4}	3.56×10^{-3}			1.76×10^{-4}	3.73	20.2
							2.69	9200	30.43	0.234	6.71			0.233	3.77	28.8
NA	18.5	12.3	4.4	12.9	1.03	2×10^{-2}	0.544	3800	41.73	4.87×10^{-4}	0.220	417	6.50×10^{-2}	1.06×10^{-3}	1.26	208
							5.32	2600	40.60	1.98×10^{-2}	21.1			7.51×10^{-2}	1.37	280
							0.363	2700	40.60	2.32×10^{-4}	0.098			3.63×10^{-4}	1.37	270
							5.21	2300	40.70	3.37×10^{-2}	20.3			6.34×10^{-2}	1.36	319
NA	12.9	9	3	8.67	0.43		0.441	1400	45.20	8.88×10^{-4}	0.182	672	1.82×10^{-2}	8.87×10^{-4}	3.49	204
							5.55	1700	43.78	5.28×10^{-2}	28.8			0.188	3.84	153
							0.266	1300	45.20	3.72×10^{-4}	0.066			3.00×10^{-4}	3.49	220
							5.47	1500	43.90	6.33×10^{-2}	28.0			0.160	3.81	175
NA	22	15	4.4	18	5	15	60	14000	61.64	5.73	32.3	4.20	2.20	5.4	11.8	6.01
							100	12000	60.85	21.5	89.8			15.7	14.5	5.73
						3.5×10^{-3}	60	7500	61.65	3.38	32.3			3.39	13.9	9.53
							100	7700	61.11	12.9	89.8			9.9	14.3	9.04
																= data obtained under atmospheric pressure

3.5 Resonator Optimization and Behavior Prediction

In order to achieve higher performance for the thermal-piezoresistive resonators, it is desirable to maximize the resonator motional conductance (g_m) (for improved signal to noise ratio) with minimal power consumption. Therefore, a figure of merit for the

resonators has been defined as the ratio of the resonator g_m to the overall DC power consumption:

$$F.M. = \frac{g_m}{P_{DC}} = \frac{2\alpha E \pi_l Q}{C_{th} \omega_0 (R_A + R_s)} \qquad (3.10)$$

where $P_{DC} = I_{DC}^2.(R_A + R_S)$ is the DC power consumption of the resonator. Different parameters that can be used to maximize $F.M.$ are as follows.

3.5.1   Actuator Beam Dimensions

Generally, smaller actuator dimensions lead to smaller C_{th} improving resonator figure of merit. However, the effect of actuator dimensions on its electrical resistance (R_A) should also be taken into account.

Since the extensional stiffness of the actuator beams define the I^2-BAR resonant frequency, in order to maintain the same resonant frequency for an I^2-BAR while reducing its actuator thermal capacitance, both length and width of the actuator should be scaled down simultaneously. Such scaling does not affect the actuator electrical resistance (R_A). Therefore, scaling down both the length and width of the actuator beams by a scale S_a, results in an improvement in the resonator $F.M.$ by a factor of S_a^2 while maintaining an almost constant resonant frequency for the device.

3.5.2   Resonant Frequency and Resonator Scaling

At a first glance at Eq. 3.10, higher frequencies seem to have a deteriorating effect on resonator figure of merit. However, if higher resonant frequencies are achieved by shrinking the resonator size, at the same time C_{th} will be shrinking sharply.

If all resonator dimensions are scaled down proportionally by a factor S, $C_{th} \propto S^3$, $\omega_0 \propto S$, and $(R_A + R_S) \propto S$. Therefore, $F.M. \propto S$, i.e. $F.M.$ increases proportionally if the resonator dimensions are scaled increasing its resonant frequency at the same time.

To experimentally investigate the effect of resonator scaling, scaled versions of similar resonators (with the same horizontal dimensional aspect ratios), were included in the layout and fabricated. In order to have a fair comparison between $F.M.$ values for different resonators, the effect of resonator mechanical quality factor was factored out by defining a coefficient (K) defined as:

$$K = \frac{F.M.}{Q} \tag{3.11}$$

Values of K coefficients extracted from the measurement results for different resonators under different DC bias current are shown in Fig. 3.11 with the data corresponding to similar resonators with different scales presented on the same axes. These plots confirm that smaller scale resonators with higher resonance frequencies have higher transduction strength.

It can be concluded from the last two discussions that the capability to fabricate resonator actuator beams with very small (nanoscale) dimensions is the key to achieving very high performance levels for thermal-piezoresistive I^2-BARs, both at low and high frequencies.
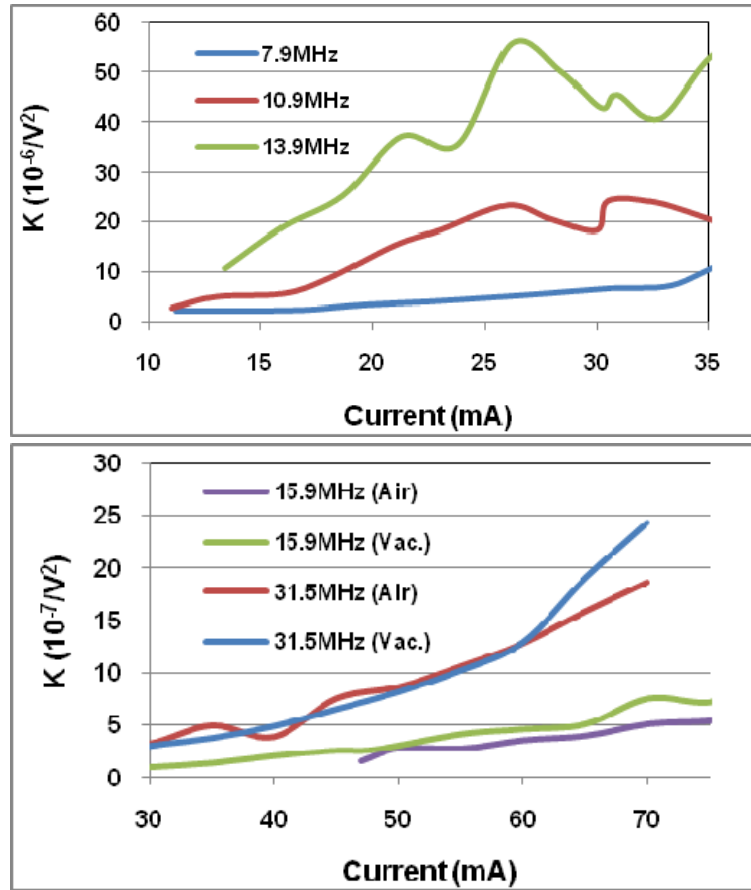
Figure 3.11. Extracted K values for similar scaled resonators versus resonator bias current. In both sets of resonators, the smaller (higher frequency) devices have higher transduction strength.

3.5.3 Electrical Resistivity and Other Material Properties

The most important parameter that can also be controlled for some of the most popular resonator structural materials (e.g. Si or SiC), is the electrical resistivity of the structural material. Lower electrical resistivity of the structural material improves the resonator transduction figure of merit by lowering $R_A + R_s$. This can be explained by the fact that, with lower electrical resistivity, the same amount of DC bias current and therefore the same motional conductance can be maintained while burning less ohmic power in the structure. A number of other structural material properties also affect the figure of merit for the thermal-piezoresistive resonators. Higher thermal expansion

coefficient and lower specific heat capacity improve the thermal actuation resulting in proportionally higher *F.M*. Higher piezoresistive coefficient improves the piezoresistive readout having the same effect on *F.M*. One interesting and promising fact is the giant piezoresistive effect found in single crystalline silicon nanowires that has been observed and reported by different researchers [43]. Therefore, as the resonators are scaled down to reach higher resonant frequencies in the hundreds of MHz and GHz range, it is expected that the actuator beams with deep submicron width exhibit such strong piezoresistivity significantly improving resonator performances.

Using structural materials with higher Young's modulus (*E*) can also improve the resonator figure of merit while increasing its resonant frequency.

3.5.4   Thermal Actuation at GHz Frequencies

It was shown through theoretical derivations and measurements that thermal actuation is not only a suitable mechanism for high frequency resonator applications, but also it can provide higher performances at higher rather than lower frequencies. In this section, the derived resonator model is utilized to predict the performance of higher frequency thermal- piezoresistive I^2-BARs with resonant frequencies in the GHz range. Two scaled down versions of the 61MHz resonator of Fig. 3.2b with resonant frequencies of 900MHz and 2.1GHz with resistivity of 3.5×10-3 Ω.cm were analyzed using the developed model. The results are presented in Table 3.2 showing that gm as high as 1mA/V can be achieved for such high frequency resonators with power consumptions in the sub-mW range. The same gm values with much lower power consumption can be achieved on lower resistivity substrates. Table 3.2 also includes calculated characteristics

for resonator with scaled down actuator dimensions to further minimize their power consumptions (maximize F.M.). For such devices power consumption as low as a few μW, can provide motional conductance of 1mA/V.

It should be noted that for all the calculations presented in Table 3.2, the bulk piezoresistive coefficient of silicon has been used. However, for such high frequency resonator, thermal actuators are practically silicon nanowires and are expected to have up to 40X higher piezoresistive coefficients than that of bulk silicon [43]. Therefore, it is expected that the resonator performances in the GHz range will even be better that what is shown in Table 3.2.

Table 3-2 Predicted resonator performance parameters for two scaled down versions of the 61MHz resonator of Fig. 3.2b with resonant frequencies of 900MHz and 2.1GHz obtained from the developed model.

Scale Factor	Resonator Dimensions (μm)						Measured/Assumed Parameters			Calculated Parameters				
	A	b	c	L	W	h	Current (mA)	Q. Factor	Freq. (MHz)	Power (mW)	R_A (Ω)	g_m (mA/V)	F.M. ($10^{-6}/V^2$)	Power (μW) @ g_m=1 (mA/V)
1X	22	15	4.4	18	5	15	60	14000	61.64	32.3	4.2	5.4	11.8	6013
0.0723X	1.59	1.08	0.39	1.3	0.36	1.08	4.67	14000	900	2.40	58.5	5.4	161	445
0.5X Act.*				0.65	0.18		2.24	14000	904.5	0.578	58.5	5.4	667	107
0.25X Act.*				0.32	0.09		1.09	14000	905.7	0.139	57.6	5.4	2775	25.7
0.031X	0.68	0.46	0.14	0.56	0.15	0.46	1.99	14000	2100	1.02	142	5.4	378	189
0.5X Act.*				0.28	0.075		0.961	14000	2111	0.246	142	5.4	1567	45.6
0.25X Act.*				0.14	0.037		0.475	14000	2113	6.18×10^{-2}	143	5.4	6243	11.4

* Scale factors identified by "Act*" show devices for which actuator sizes have been further scaled down in addition to the overall scaling of the resonator.

4. **CONTROLLED BATCH FABRICATION OF CRYSTALLINE SILICON NANOBEAM-BASED RESONANT STRUCTURES**

Unique properties such as huge piezoresistive coefficients observed in silicon nanowires compared to bulk silicon [43] as well as extremely high mass sensitivity of nanowire resonators [44] can pave the way towards more sensitive highly integrated sensor arrays. The work on chapter two and three on thermally actuated high frequency electromechanical resonators showed that thermal actuation could be a viable candidate for high frequency applications provided that small enough thermal actuator beams (practically nanowires) can be realized [38]. However well-defined and controlled batch fabrication of such nanoscale structures remains a formidable challenge. Bottom-up fabrication should generally be followed by sophisticated assembly procedures. In addition, adequate reproducibility and uniformity are extremely hard to realize for the bottom-up techniques. In case of top-down processes, the main challenge is to control and eliminate size variations along the length and edge roughness causing undesirable performance variations. Furthermore, most top-down approaches use costly serial nanolithographic processes such as e-beam lithography.

4.1 Silicon Nanowire Fabrication Method

The self-aligned nanofabrication technique demonstrated in this chapter takes advantage of the crystalline structure of silicon that can provide the ultimate high-precision alignment and size control, to define nanoscale features. Anisotropic wet

etching of silicon in alkaline solutions is a well known process that has been vastly used for implementation of larger scale MEMS. This process can provide extremely smooth surfaces and well defined features (straight lines and sharp corners) with atomic level precision.

The developed technique is based on inducing a rotational misalignment between the photo-lithography defined patterns and the crystal orientation of the silicon substrate. As shown in Fig. 4.1, this results in undercutting the mask layer and leaving behind much thinner features after etching, provided that the etch time is long enough. The major difference between this undercut and the undercut resulting from isotropic wet or plasma etch processes is its self-control and relative independence from the speed and length of the process. The first (111) plane in the structure that is fully covered by the mask on top acts as a strong etch-stop. The size of the final structure is defined by the angle between the initial pattern and the appropriate crystalline orientation (110 direction in case of 100 silicon substrate) and the size of the lithographically defined pattern:

$$W_f = W_d - L_d \tan \theta \qquad\qquad (4.1)$$

where W_d and L_d are the initially defined dimensions on the photolithography mask, W_f is the width of the resulting beam after a long enough etch, and θ is the angle between the initial pattern and the crystalline orientation.
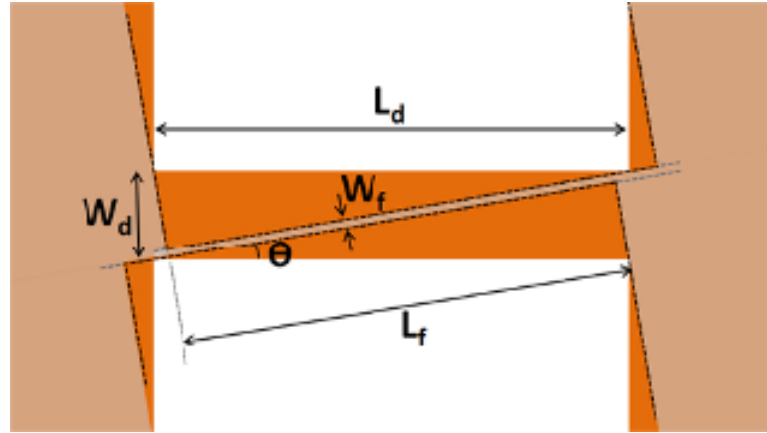
Figure 4.1 Schematic view of the self-aligned fabrication technique for definition of sub-micron silicon features using conventional micro-lithography.

4.2 Silicon Nanowire Fabrication Results

The proposed fabrication technique was utilized on different SOI and regular silicon substrates to demonstrate nanoscale feature sizes and nanowires. Figure 4.2 shows the fabrication sequence that starts with definition of microscale features on a thin (~100nm) thermally grown silicon dioxide mask on the substrate. The silicon device layer is then etched anisotropically in a heated (~65ºC) aqueous KOH solution. The samples were left in the etchant solution for a long enough time to undercut the oxide mask all the way until stopping at the 111 planes. This was followed by a short Hydrofluoric acid (HF) dip to remove the oxide mask on top and, in case of SOI substrates, to also undercut the remaining narrow features. A basic lithography system with minimum feature size capability of 2μm was utilized to generate the patterns.
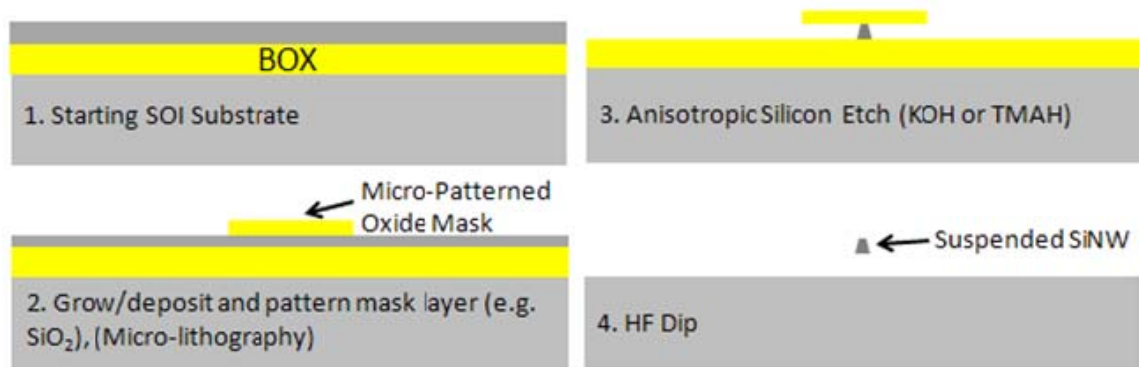
Figure 4.2. Schematic cross-sectional view of the fabrication sequence for implementation of silicon nanowires on thin SOI device layers.

Figure 4.3 shows the SEM view of a fabricated suspended silicon bridge with an upper surface width of less than 100nm fabricated on a SOI substrate with device layer thickness of ~1.3μm using the described nano-pattern generation technique. The 54.7º sidewalls are the (111) crystalline planes acting as an etch-stop. Well-defined suspended nanowires can be fabricated by performing the same procedure on thinner SOI substrates. Furthermore, vertical sidewalls can be achieved on 110 silicon substrates [45].

Figure 4.4 shows the SEM view of one of a similar features generated on a regular silicon substrate. The oxide mask is left on top of the structure deliberately to show the undercut of the oxide layer and the resulting submicron silicon feature underneath it. The combination has a similar shape as predicted and depicted in Fig. 4.1. As clearly seen in Fig.s 4.3 and 4.4, this technique also eliminates the rounded corners that are typically generated by optical lithography leaving behind sharply defined 90º angles at the corners. Figure 4.5 shows the SEM view of the resulting structure from a similar fabrication sequence performed on a SOI substrate with a very thin (~250nm thick) silicon device layer. The resulting silicon wire has a trapezoidal cross-section with cross-sectional dimensions in the 200-300nm range.
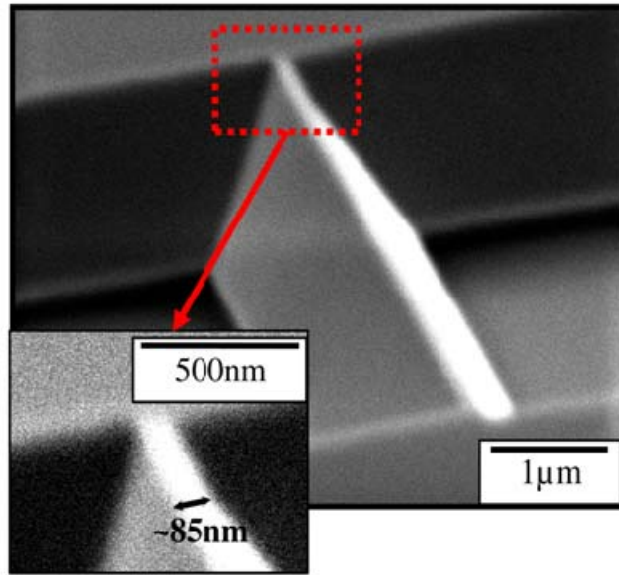
Figure 4.3. SEM view of a suspended silicon bridge with a width of ~85nm on its upper surface fabricated on a SOI substrate with device layer thickness of ~1.3μm.
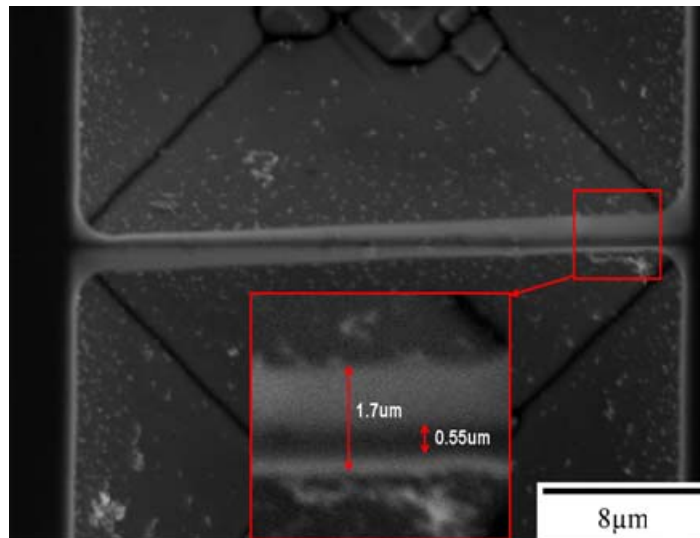
Figure 4.4. SEM view of a submicron feature generated on a regular 100 silicon substrate using an optical lithography defined oxide mask and rotational misalignment between the layout and the crystalline orientation of the substrate. The light area on the oxide layer is the undercut region and the darker area shows the remaining silicon beam underneath the oxide mask after anisotropic wet etching of silicon.

Finally, a 100nm thick oxide layer was thermally grown on the same nanowire and the oxide was removed in HF consuming about 50nm of the silicon on surfaces all around nanowire. The resulting nanowire has a diameter of ~100nm as shown in Fig. 4.6. Oxidation of the nanowires fabricated using this technique helps round the edges of the

54
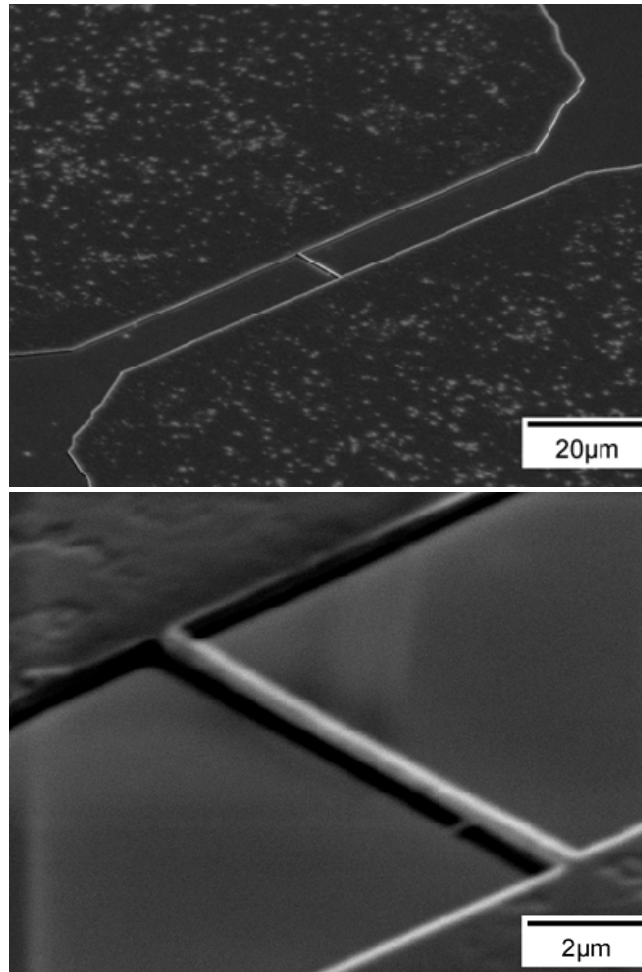
Figure 4.5. SEM views of a silicon nanowire fabricatied between two large pads on a 100 SOI wafer with the device layer thickness of ~250nm and buffer oxide thickness of 100nm. The fabricated nanowire has a trapezoidal cross-section with a width of 200-300nm.
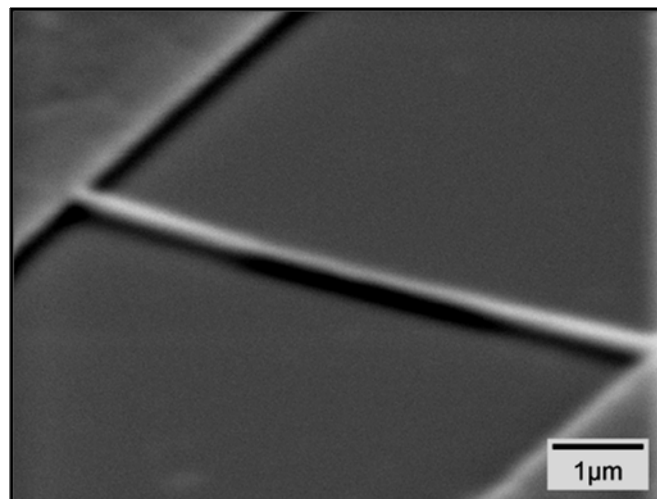
Figure 4.6. SEM view of the silicon nanowire of Figure 5 after thermal growth and removal of a 100nm silicon dioxide layer. The resulting nanowire has a thinner diameter (~100nm) and rounded overall cross-section.

wires leaving behind a somewhat circular cross-section. Due to the high smoothness and uniformity of the nanowires fabricated using this technique along their length, thermal oxidation can conveniently be used to significantly reduce or tune their cross sectional area without causing extreme non-uniformities or discontinuities in the wires.

4.3 Fabrication of Dual Plate Resonators with Nanobeam Thermal Actuators

The same method can be applied to the thermally actuated resonators. Since the rounded corners are unstable in KOH solution, a new structure developed in which all the corners of the resonator structure are stable. In this new structure the support beams have been connected to the outer corners of the two plates rather than the thermal actuators. Figure 4.7 shows the top view of a dual plate resonant structure fabricated on a 1µm thick SOI substrate with the oxide mask left on top of it after wet etching of silicon. The oxide mask has been kept on top of the structure to show how the undercut of the mask leads to nanoscale line widths for the beams in the middle of the structure.
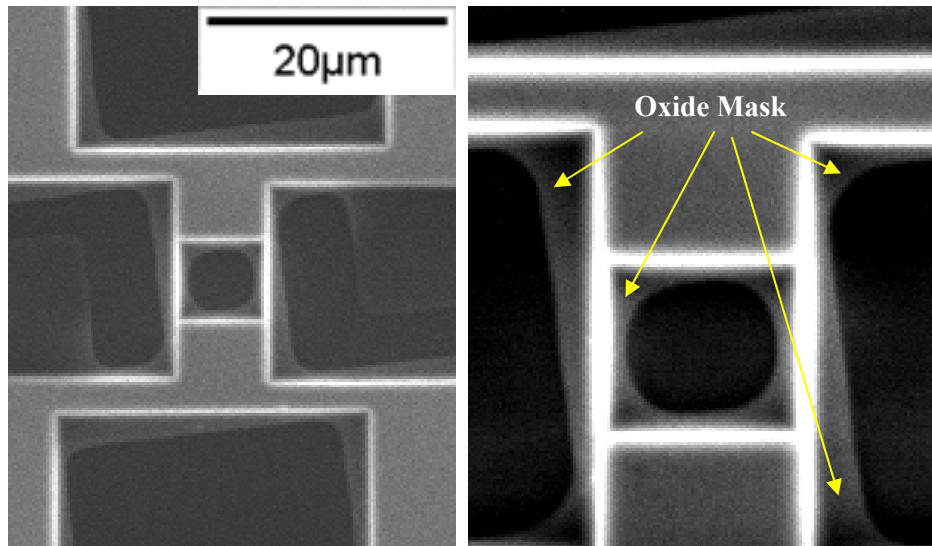
Figure 4.7. SEM view of a wet-etched silicon structure showing feature size reduction and edge sharpening of the structure compared to its angled microlithography patterned oxide mask.

Figure 4.8 shows two similar dual-plate resonators with different misalignment angles after removing their oxide masks showing a smaller beam width of ~250nm for the structure with the larger misalignment angle.

Figure 4.9 compares the harshly rounded and unpredictable features on a lithographically defined structure with a similar wet-etched structure.
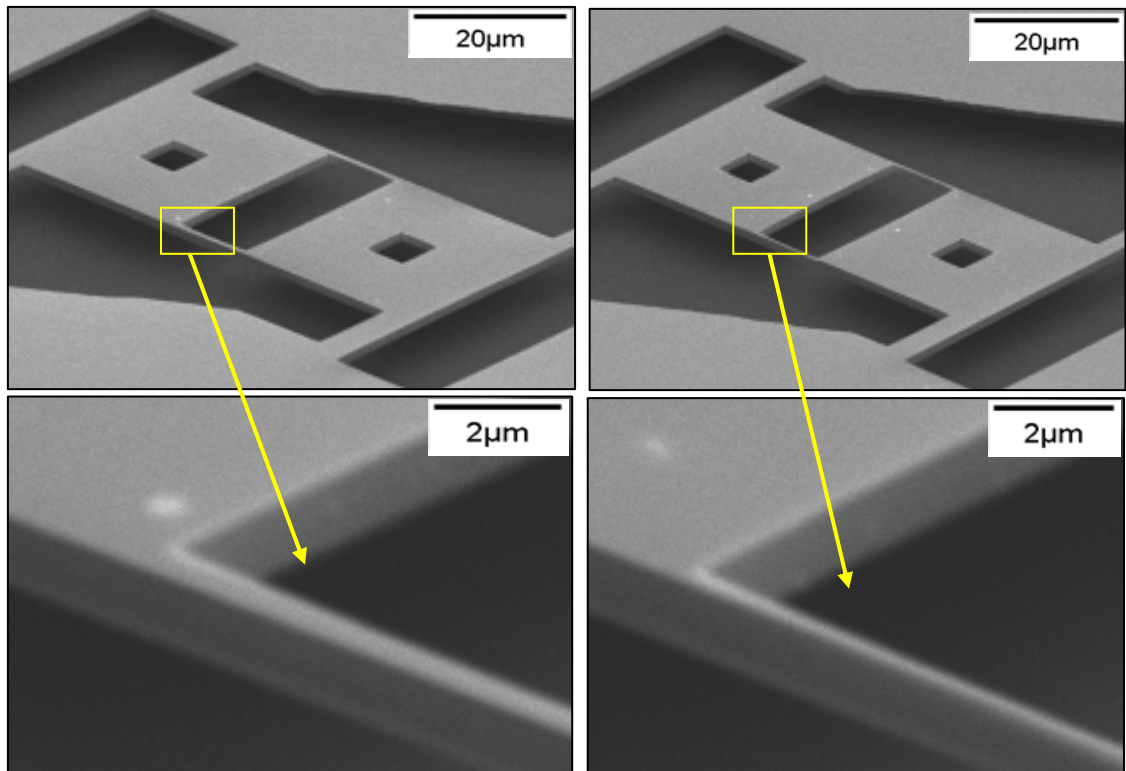
Figure 4.8. SEM view of two fabricated resonant structures with similar microlithography patterns but different alignment angles showing a much thinner width for the actuator beams of the resonator on the right side that has a misalignment angle of 1º larger. A photolithography tool with resolution of 2μm has been used for the initial patterning.
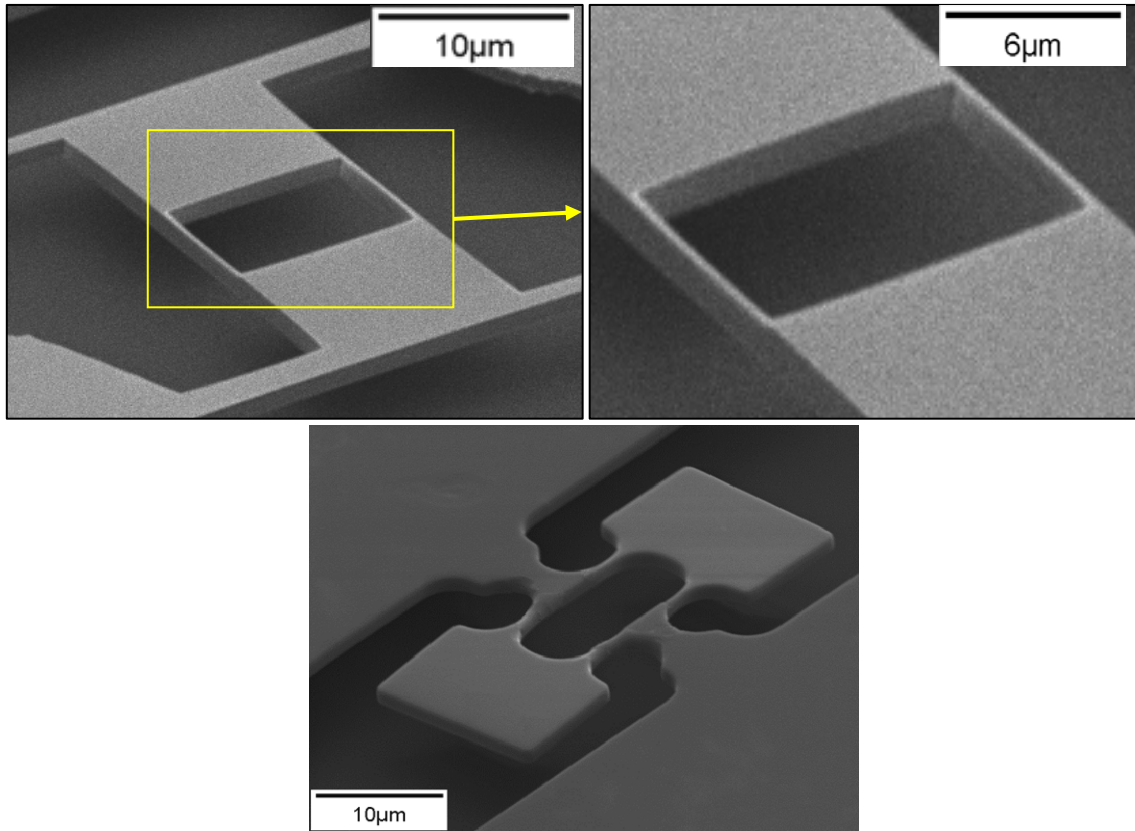
Figure 4.9. Comparison between a structure fabricated using the presented self-aligned technique and another structure with similar feature sizes patterned via optical lithography and thinned down via thermal oxidation and oxide removal. The wet-etched structure has very smooth and uniform features and sharp corners, while the smaller features in the other structure are harshly rounded and unpredictable.

4.4   Measurement Results

Figure 4.10 shows the measured frequency responses for the resonators in Fig.s 4.8 and 4.9.
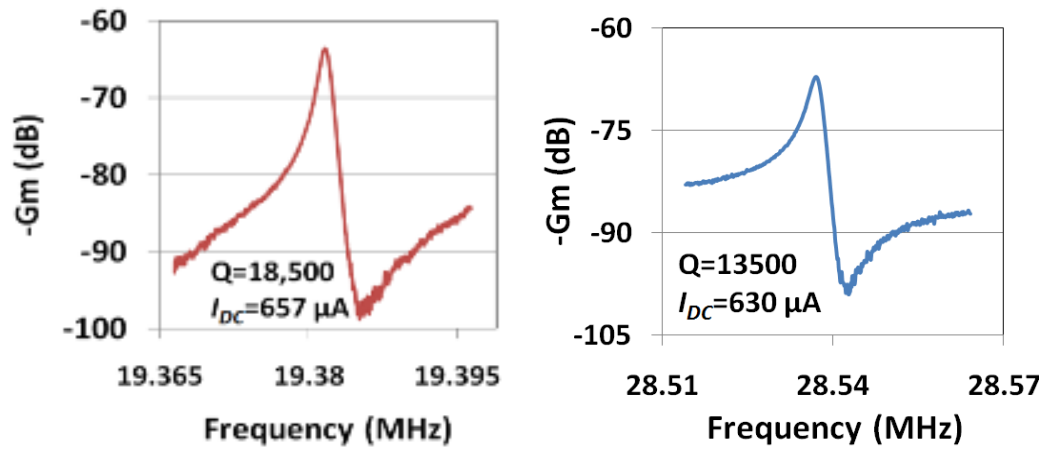
Figure 4.10. Measured frequency responses for the 19.4MHz resonator of Fig. 4.3 (the device on the right side) and the 28.5MHz resonator of Fig. 4(the wet etched device). The nanobeams thermally actuate the structures into resonance and sense the resonance as piezoresistors.

5. INTERNAL THERMAL-PIEZORESISTIVE FEEDBACK IN MICROMECHANICAL STRUCTURES

Thermal actuation is one of the mechanisms widely used in micro/nanoelectromechanical systems capable of providing large forces. In addition, it has the advantage of being extremely simple to implement within a simple structure. By heating only specific parts of the MEMS structure, variety of movements can be generated. Such local heating inside thermal actuators can be fulfilled by passing a current through them. The elevated temperature causes a thermal expansion which also depends on physical property of the used material. The expanded parts experience stress which in turn due to the piezoresitive effect, changes their resistance. The resulted variations in resistnce affects the overall power consumption of the element. This change in power consumption results in a change in temperature and therefore causes a mechanical movement. Such thermo-electro-mechanical loop can pump some electrical energy into the mechanical structure.

This chapter demonstrates the existence of thermal-piezoresistive energy pump in the mechanical structure of higher frequency extensional mode dual-plate resonators. By applying a DC bias current to the proposed resonators, at lower currents only a part of the mechanical losses will be compensated by the electrical energy which results in self-Q-enhancement in such devices [39]. However, by increasing the DC bias current after passing a threshold, the mechanical losses could be fully compensated leading to self-sustained oscillation of the resonant devices [40]. The proposed resonant structures are

capable of oscillating under both vacuum and atmospheric pressure with higher output voltage amplitudes.

5.1   Device Structure and Concept

Figure 5.1 shows the in-plane resonant mode shape of a dual-plate resonator. In this mode the two plates are moving back and forth, while the two thermal actuators between them are moving in their extensional mode. Figure 5.2 shows a schematic diagram, quantitatively demonstrating the series of events happening during resonator transduction. Upon the application of a combination of AC and DC voltages across the resonator, it heats up by the resulting ohmic loss. Due to the higher resistance of the narrow beams in the middle of the structure the ohmic loss is maximized in them. The alternating ohmic loss causes the generation of a fluctuating temperature in narrow beams. The AC temperature in turn results in a periodic mechanical force inside them actuating the resonator in its in-plane extensional mode. In this mode, the two plates move back and forth in opposite directions causing periodic expansion and contraction in the beams connecting the two plates. At the same time due to the piezoresitvive effect, the fluctuating stress and strain causes a periodic change in the resistance of the thermal actuators. This change can be modulated as an output AC current. In addition, this change in resistance due to the applied DC voltage across the resonator can further produce an AC power with the same frequency and phase as that of the AC input power. This added AC power forms an internal positive feedback loop that takes electrical power from the applied DC voltage and feeds it to the mechanical structure of the resonator. This internal

positive feedback can partially or even fully compensate for all the mechanical energy losses in the structure.
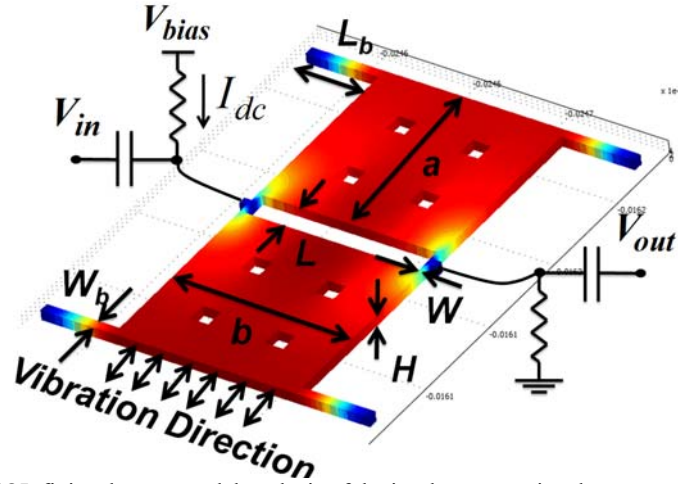
Figure 5.1. COMSOL finite element modal analysis of the in-plane extensional resonant mode of a dual plate 4.5MHz resonator and the used one-port electrical measurement configuration. Red and blue show the maximum and minimum vibration amplitudes respectively.
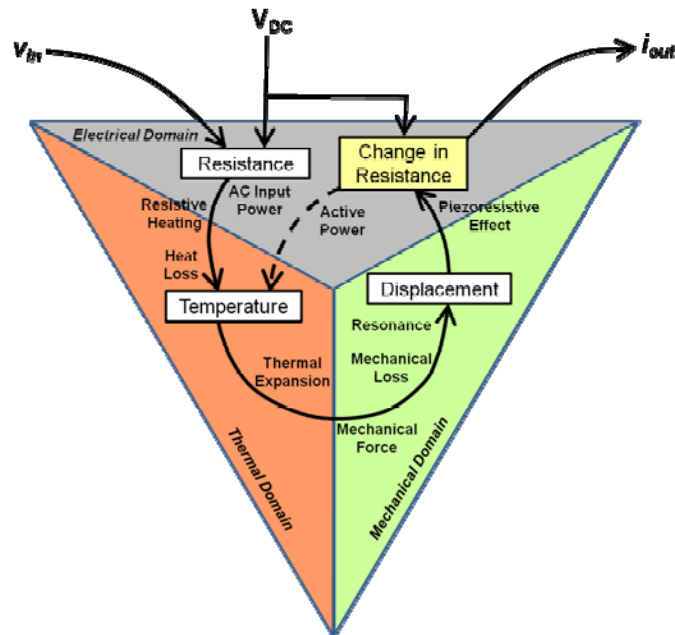
Figure 5.2. Schematic diagram of a thermal-piezoresistive resonator showing the interaction between the three physical domains of electrical, thermal and mechanical. It demonstrates that how the operation of the resonator based on its internal positive feedback loop leads to self-Q-enhancement capability

The operation of such resonator is a result of interactions between three different physical domains of thermal, mechanical and electrical. By modeling each of these domains the overall equivalent electrical circuit of the resonator which is shown in Fig. 5.3 is obtained [38].
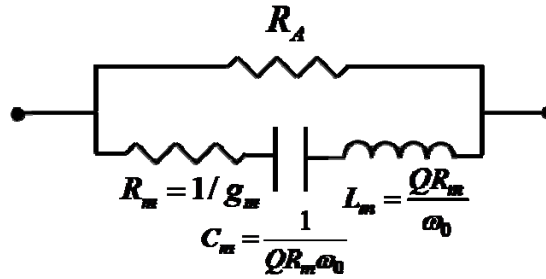
Figure 5.3. Overall equivalent electrical circuit for one-port thermally actuated resonators with piezoresistive readout. R_A is the electrical resistance of the actuators.

Moreover, the motional conductance (g_m) for such devices which is the ratio of the output motional current versus input AC voltage is given by Eq. (2.13). Unlike the piezoelectric and electrostatic micromechanical resonators that can only have positive (passive) motional resistance/conductance, based on Eq. (2.13) thermal piezoresistive resonators can potentially have negative (active) motional conductance provided that the piezoresistive coefficient (π_l) of the structural martial is negative. In case of N-type single crystalline silicon the piezoresistive coefficient is negative [53].

A negative resistance/conductance in electronics is considered as an active energy pump. Therefore, as opposed to the passive resonators that just lose energy through their mechanical structure as well as their electronic circuitry, such thermal-piezoresistive resonators can feed some energy back into their mechanical structure. Based on Eq. (2.13) by increasing the DC bias current, the motional conductance increases with a squared relationship. The increased motional conductance can compensate for a higher

63

portion of the mechanical losses. Therefore, by increasing the current effective quality factor of such devices increases. This leads to even higher Q enhancement to values well beyond the mechanical limit.

The increase in the effective quality factor of the resonator can be shown as a function of the motional conductance. To do so quality factor is defined as the ratio between the energy stored (E_S) in the resonator over the energy dissipated (E_D) per cycle in it:

$$Q = \omega_0 \frac{E_S}{E_D} \tag{5.2}$$

Considering a series RLC circuit which is the equivalent circuit of a mechanical resonator, the mechanical quality factor of the resonator could be found. The maximum energy stored in the inductor (L_m) is:

$$E_S = \frac{1}{2} L_m I_{MAX}^2 \tag{5.3}$$

where I_{MAX} is the maximum current passing though the RLC circuit. There is no energy stored in the capacitor at this instant because the current passing though the elements and the voltage across the capacitor are 90° out of phase. On the other hand, the energy lost in the circuit is:

$$E_D = \frac{1}{2} R_m I_{MAX}^2 \tag{5.4}$$

By replacing Eq.s (5.3) and (5.4) into (5.2) the mechanical quality factor of the resonator can be found as follows:

$$Q_m = \frac{\omega_0 L_m}{R_m} \tag{5.5}$$

In order to find the effective quality factor of the resonator, the circuit in Fig. 5.3 could be used which consists of a series RLC circuit in parallel with the physical resistance of the resonator. In this case the stored energy is the same as the previous case and only the energy loss decreases:

$$E_D = \frac{1}{2}\left(R_m + \frac{R_m^2}{R_A}\right)I_{MAX}^2 \tag{5.6}$$

By replacing Eq.s (5.3) and (5.6) into (5.2), the effective quality factor can be found. By dividing both sides of the obtained equation by Eq. (5.5), the relationship between the mechanical and effective quality factors of a resonator can be derived:

$$Q_{eff} = \frac{Q_m}{1 + R_A \cdot g_m} \tag{5.7}$$

where Q_m and R_A are the mechanical quality factor and physical electrical resistance of the resonator respectively. According to Eq. (5.7) the value of Q_{eff} can potentially be set to values orders of magnitude higher than the mechanical Q of the structure by tuning the value of g_m. This can be simply accomplished by tuning the bias current of the resonator.

If the absolute value of the negative motional conductance resulting from negative piezoresistive coefficient is increased to reach and surpass the value of R_A^{-1}, instead of the resonator losing part of its energy in every cycle, it gains some extra energy in each cycle, which leads to instability of the resonant system and self-sustained oscillation. As shown in Fig. 5.4, physically this can be explained as follows: upon application of a DC bias, the thermal actuators heat up, pushing the plates further away from each other. Due

to the mass (inertia) of the plates, the beams experience an over-expansion after pushing the plates and undergo tensile stress. Due to the negative piezoresistive coefficient, the tensile stress translates into reduced electrical resistance in the beams. Since a constant DC bias current is passing through the beams, this reduces their ohmic power and therefore their temperature forcing them to contract. Again due to the mass of the plates, the actuators experience over-contraction and undergo compressive stress which increases their resistance. This increases the power consumption forcing the structure to expand again. If the resulting driving force (due to heating and cooling) in each cycle is large enough to compensate for mechanical losses of the structure, the same sequence is repeated over and over in a self-sustained manner and the vibration amplitude keeps increasing until it is limited by nonlinearities. Figure 5.4 also shows how the thermal and mechanical delays provide an overall phase shift of 360 degrees for the loop leading to a perfect timing for the abovementioned sequence of physical phenomena to continue. The loop can be divided into two half cycles of heating and cooling.
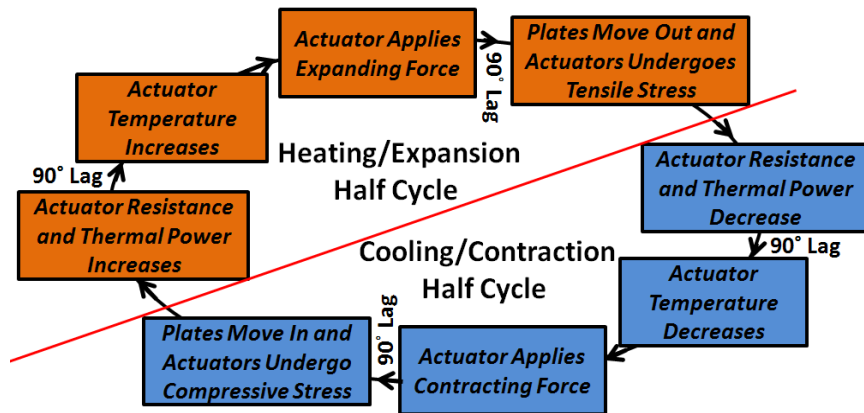
Figure 5.4. Sequence of events causing an internal positive feedback loop that provides 360 degrees of phase shift in thermal-piezoresistive resonators biased with a constant current that lead to self-sustained oscillation.

5.2   Fabrication and Measurement Results

Figure 5.5 shows the SEM view of a 4.5MHz (a) and 18.1MHz (b) dual-plate resonators fabricated on a low resistivity (0.01-0.05 Ω.cm) N-type SOI substrate. The standard single-mask SOI-MEMS process was used to fabricate the resonators in Fig. 5.5

To minimize the resonators power consumptions and at the same time improve the performance of such, the actuator beams were thinned down by thermal oxidation and subsequent oxide removal using HF. The four support beams on the outer corners of the plates are to add to the vertical stiffness of the plates and avoid their stiction to the handle layer during HF release. In order to further minimize acoustic loss through the support beams and maximize resonator mechanical quality factors (Q), the dimensions of the beams are chosen so that their first flexural mode frequency is close to the first in-plane extensional mode of the dual-plate resonator. The four openings in each of the plates in Fig. 5.5a are to expedite plates' release time in HF and avoid excessive undercut of the testing pads. To maximize the resonator transduction coefficient and get higher output signals, the structures are aligned to the 100 crystal orientation, where the absolute value of the longitudinal piezoresistive coefficient is maximum [53].

The self-Q enhancement capability of thermal-piezoresistive resonators was studied using the one-port measurement configuration shown in Fig. 5.1. The applied DC bias currents were less than the oscillation threshold currents needed for initiating the self-sustaining oscillation. Figure 5.6 shows the measured frequency responses for the 18.1MHz resonator in Fig. 5.5b with different bias currents directly taken from the network analyzer. As the DC bias current of the resonator increases the absolute value of

67
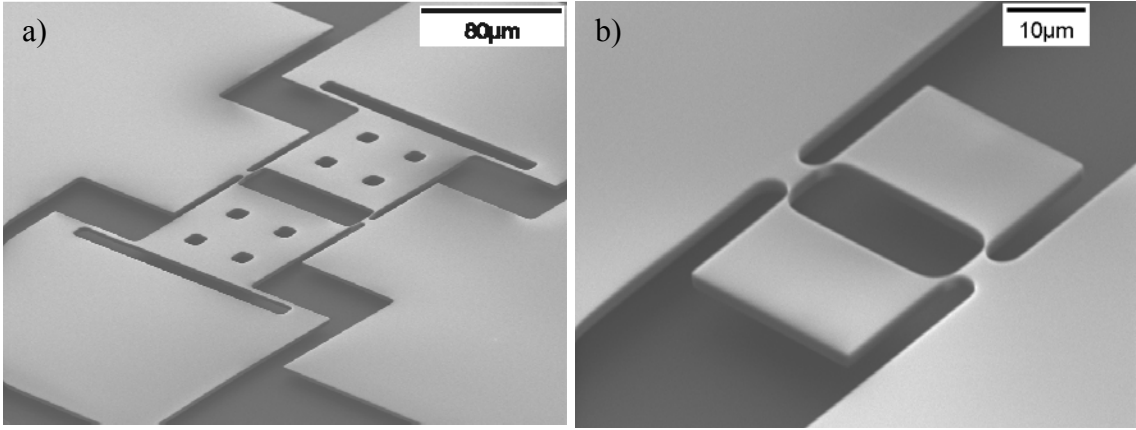
Figure 5.5. SEM view of two fabricated 3.3μm thick N-type in-plane extensional mode dual-plate resonators along 100 crystalline orientation of silicone with resonant frequencies of a) 4.5MHz and b) 18.1MHz.
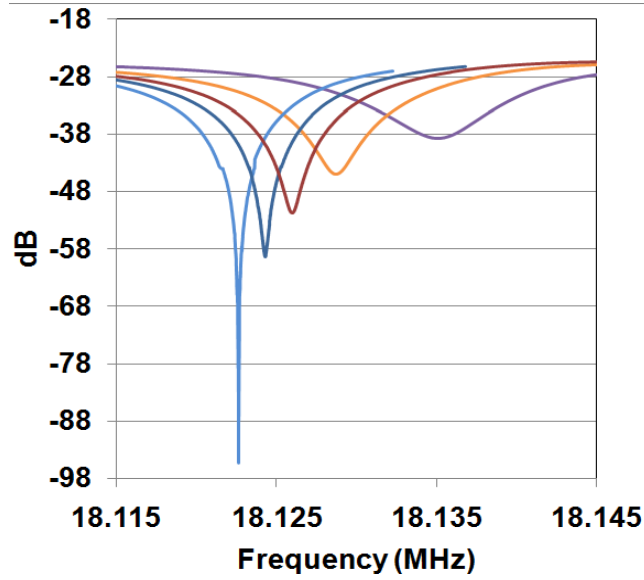
Figure 5.6. The measured frequency response of the 18.1MHz resonator of figure 5.1b under different DC bias currents which is directly taken from the Network Analyzer.

the negative gm increases leading to a sharper decrease in conductance at resonance and therefore higher effective quality factor.

Figure 5.7a shows the frequency response of the 18.1MHz resonator which is the calculated absolute value of the motional conductance of the resonator at a low bias current of 3.468mA. At this low current the absolute value of gm is very small and the measured Q is actually the mechanical Q of the resonator. At higher currents the absolute value of gm increases, leading to sharper increase in the impedance of the structure at

resonance. Figure 5.7b shows the calculated overall resistances of the same resonator upon application of higher bias currents, extracted from the measured frequency responses of Fig. 5.6. These plots could be used to measure the resonator effective electrical Q. While the mechanical Q of the resonator measured at lower bias currents is only ~2,000, the measured effective Q of the resonators increases sharply as the bias current is increases above 6mA and reaches ~2,100,000 with bias current of 6.2mA. The
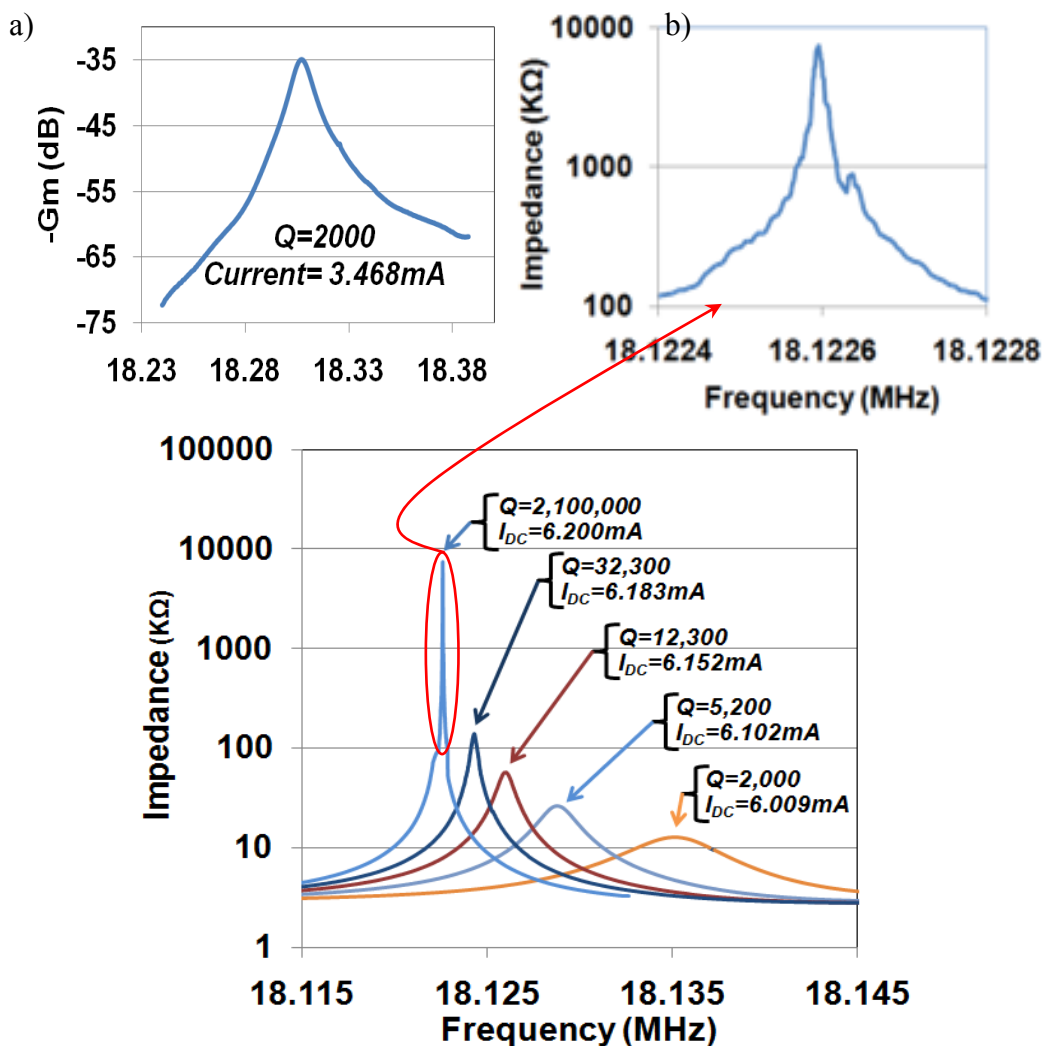
Figure 5.7. a) Frequency response of the 18.1MHz resonator of Fig. 5.1b biased at a low bias current. The negative value of gm is very small in this case and the measured Q is the mechanical quality factor of the resonator. b) Frequency responses for the same resonator at higher bias currents extracted from the measured plots in Fig. 5.6 showing significant Q-enhancement as the bias current increases.

effective electrical Q has been calculated as the bandwidth in which the impedance decreases to half of its peak value divided by the resonance frequency.

Table 5.1 summarizes the measurement results obtained for both the 4.5MHz and 18.1MHz dual-plate resonators in Air. Showing significantly increased Q values as high as ~40,000,000 for the 4.5MHz resonator.

Table 5-1. The measured Q-enhancement results for the two dual-plate resonators of Fig. 5.5 operated in Air with the thickness of 3.3µm.

Res. Dimensions (µm) a/b/L W/L_b/W_b	Current (mA)	Freq. (MHz)	Q_{eff} (×10³)	Q_m / R_A (KΩ)		$Z_{Res.}$ (KΩ)	Power (mW)
98/98/15.5 0.3/41.7/3.3	3.097	4.49813	4.60			7.20	18.2
	3.304	4.49746	12.0			14.4	20.7
	3.403	4.49709	24.0	4500		27.6	22.0
	3.443	4.49694	37.9			44.9	22.5
	3.484	4.49678	96.0			105	23.1
	3.504	4.49670	455	1.9		509	23.3
	3.507	4.49669	666			656	23.4
	3.509	4.49668	**1060**			**1130**	23.4
	3.511	4.49667	**40000**			**3985**	23.4
20/30/11.5 0.5/-/-	6.009	18.13500	2.00			12.9	37.9
	6.102	18.12870	5.10			26.6	39.1
	6.152	18.12599	12.3	2000		57.4	39.7
	6.162	18.12543	15.6			72.2	39.9
	6.174	18.12488	19.6			93.1	40.0
	6.183	18.12428	32.3			140	40.1
	6.192	18.12364	60.0	1.05		269	40.3
	6.197	18.12273	274			1060	40.3
	6.199	18.12271	**362**			**1760**	40.3
	6.200	18.12260	**2100**			**7490**	40.4

Figure 5.8 shows a resonator and the used electrical circuitry for testing the self-oscillation capability of such. A constant DC bias current has been applied to the resonator working in air without any amplifiers involved. The output is connected to an oscilloscope. Relatively large resistors (5-10X larger than R_A) were placed in series with the resonator to simulate a constant current source. As the bias current increased at some

point, the sinusoidal signal emerged on the oscilloscope. Further increase of the DC bias current increased the amplitude of the sinusoidal output waveform.

f = 6.60MHz, V_pp = 140mV
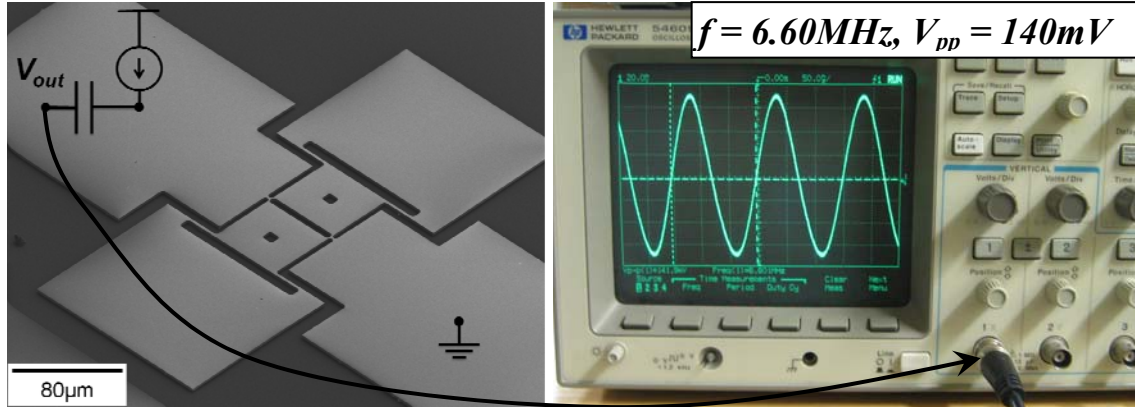
Figure 5.8. SEM view and output signal shape of a 6.6MHz 3.3µm thick N-type silicon thermal-piezoresistive dual-plate resonator capable of self-sustained oscillation. Only a DC bias current of 5.7mA is being applied to the resonator (no amplifier) and the resonator is operating in air.

Table 5.2 summarizes the self-sustained oscillation measurement results for several tested dual-plate resonators with different dimensions under both vacuum and atmospheric pressures. At lower oscillation frequencies air damping in one of the dominant sources for energy loss, therefore higher oscillation threshold currents are required in air in compare with that of vacuum (for instance 5.25MHz), whereas in case of smaller resonators with higher oscillation frequencies air damping becomes less dominant and oscillation threshold currents are almost the same under both atmospheric and vacuum pressures (for instance 19.3MHz). Jitter measurements performed on some of the single-device micromechanical oscillators show stability similar to commercially available quartz oscillators with similar frequencies. However, it is expected that much higher performance and superior phase noise characteristics can be achieved for such devices because the electronic amplifier noise, which is the main source of phase noise in conventional oscillators has been eliminated in them. Short-term fluctuations in the

71

resonator frequency caused by temperature fluctuations might be the main source for jitter in such oscillators. This short term temperature fluctuations are suspected to be caused by the electronic noise in the bias current. Therefore, much better oscillator stabilities are expected to be achievable via passive temperature compensation of the resonators (e.g. using degenerate doping [5]). It is also believed that using a low noise current source instead of using a large resistor in series with the resonant structure would further improve the jitter.

Table 5-2. Measured self-oscillation results for dual-plate resonators with different dimensions

Resonator Dimensions (µm)							Freq. (MHz)	Oscillation Current (mA)	R_{DC} (KΩ)	V_{P-PAC} (mV)	Power (mW)	$V_{Res.DC}$ (V)	Jitter (Period Std. Dev.)	Pressure
a	b	L	W	L_b	W_b	H								
97	97	27	~0.05	37	2.1	2	1.48	0.86	13.5	126	10.1	11.7	-	Vac.
198	198	16	~0.25	60	3.3	3.3	2.05	2.9	1.5	450	12.6	4.35	868ps	Air
98	98	16	~0.30	42	3.3	8.3	4.47	3.5	2	325	24.5	7	-	Vac.
98	98	16	~0.30	42	3.3	3.3	4.50	3.53	1.9	400	23.2	6.65	-	Air
67	67	17	~0.20	34	2.2	2	5.01	1.5	1.95	30	4.44	2.94	-	Vac.
67	67	27	~0.40	-	-	17	5.25	36	0.25	825	324	9	501ps	Air
								17		475	72.2	4.25	-	Vac.
68	68	10	~0.10	32	3.2	2	5.26	2.9	1.7	50	14.2	4.93	-	Vac.
68	68	16	~0.35	36	3.3	3.3	6.60	5.7	3.3	140	107	18.8	440ps	Air
67	67	17	~0.40	33	2.4	2	6.67	1.4	9.4	40	18.9	13.3	-	Vac.
20	30	11.5	~0.45	-	-	3.3	16.06	4.9	1.7	55	40.8	8.33	-	Air
20	30	11.5	~0.50	-	-	3.3	18.05	6.3	1.3	65	51.6	8.19	-	Air
20	30	11.5	~0.55	-	-	3.3	19.32	7.29	1.05	63	55.8	7.65	-	Air
							19.38	7.83		41	64.3	8.22	-	Vac.
							19.38	7.98		65	66.8	8.38	-	Vac.

5.2.1 Oscillator Optimization

In order to achieve higher performance for the proposed thermal-piezoresistive resonators, their oscillation condition could be used in which the overall conductance of

the structure should be negative ($g_m + R_A^{-1} < 0$). By replacing the g_m from Eq. (2.13), this oscillation condition could be rewritten as follows:

$$P_{DC} > \frac{KLC_{th}\omega_m}{4\alpha E^2 |\pi_l| QA} \tag{5.8}$$

where $P_{DC} = R_A I_{DC}^2$ is the DC power consumption inside the resonator structure. From Eq. (5.8) the minimum required DC power consumption that can lead to self-oscillation could be found:

$$P_{DC_{Min}} = \frac{KLC_{th}\omega_m}{4\alpha E^2 |\pi_l| QA} \tag{5.9}$$

One of the interesting aspects to look into is how this power requirement changes if the resonator dimensions are shrunk down to reach higher frequencies. If all resonator dimensions are scaled down proportionally by a factor S, $K \propto S$, $C_{th} \propto S^3$, $\omega_m \propto S$, $A \propto S^2$, therefore $P_{DCMin} \propto S^2$, meaning that if the resonator is scaled down, the oscillation power requirement goes down with a square relationship, therefore, if we can fabricate such devices with smaller dimensions, we should be able to demonstrate much higher frequency self-sustained oscillators with much lower power consumptions.

The other advantageous aspect is to lower the minimum power consumption by changing the resonator dimensions while keeping the oscillation frequency constant. It can be easily shown that this could be realized by keeping the size of the plates unchanged and scaling down the dimensions of the thermal actuators. In this case if a scale factor of S be used to scale down the dimensions of the thermal actuators, the minimum DC power consumption decreases in the squared relationship:

$$P_{DC_{Min}} \propto LA \propto S^3 \tag{5.10}$$

5.2.2 Dual-Harmonic High Frequency Oscillator

In order to improve the performance of such oscillators, in this work a wider third bar has been added to the I^2-shaped structures (Fig. 5.1). The I^3-shaped structure of Fig. 5.9 explored. In the resulting I^3-shaped structure the stiffness of the resonator is mainly determined by the wider middle bar. Therefore higher resonance frequencies can be achieved while maintaining very narrow actuator beams. For the same reason fabrication induced changes in the dimensions of the narrow thermal actuators will not have a significant effect on the frequency of the resonator.
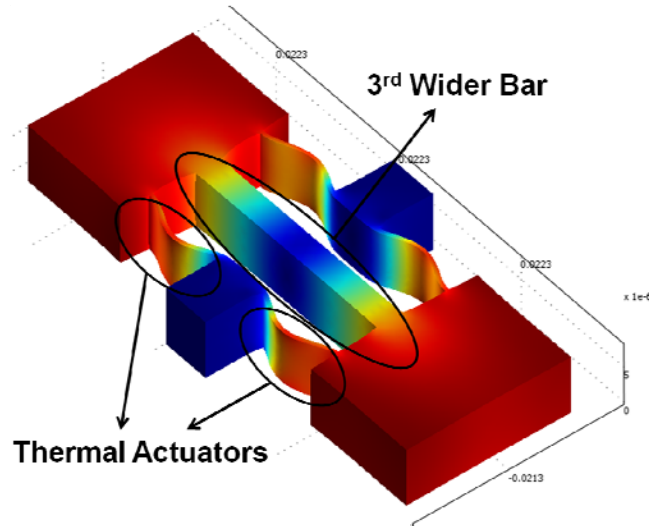
Figure 5.9. Modal analysis results showing the fundamental in-plane resonance mode shape for an I^3 resonant structure. In this structure a third wider bar has been added in the middle of the structure to further increase the resonance frequency of the resonator. Red and blue colors show locations with the largest and smallest vibration amplitudes respectively.

Figure 5.10a shows the SEM view of a fabricated resonator as well as the schematic view of the required bias current and electrical connections for oscillator operation and measurement. For this resonator a series of thermal oxidation steps followed by oxide removal in hydrofluoric acid were carried out to narrow down the thermal actuators. Instead of current sources relatively large resistors with values a few

times (up to 10X) larger than the electrical resistance of the resonator, were used to provide the resonator bias currents. The AC output was connected to a high frequency digital oscilloscope. By gradually increasing the bias current, after passing a threshold, the waveform in Fig. 5.10b with oscillation frequency of 36.54MHz emerged on the oscilloscope. As it can be seen in Fig. 5.10b, the output signal shape is far from a sinusoidal due to existence of different frequency harmonics. Since the tested resonator has its first in-plane resonance mode at 17.4MHz, it can be concluded that the second harmonic is the dominant component. The first harmonic shows itself as uneven level of the consecutive peaks in the output waveform. In addition, the small ups and downs in the waveform can be blamed on higher frequency harmonics. It was noticed that by further increasing the bias current, the output voltage waveform constantly changes and at some point the first frequency harmonic with frequency of ~17.5MHz becomes dominant. Figures 5.10c-f show how the output waveform changes by increasing the bias current. Figure 5.10f shows a close to sinusoidal waveform at the same frequency as the mechanical resonance frequency of the structure.
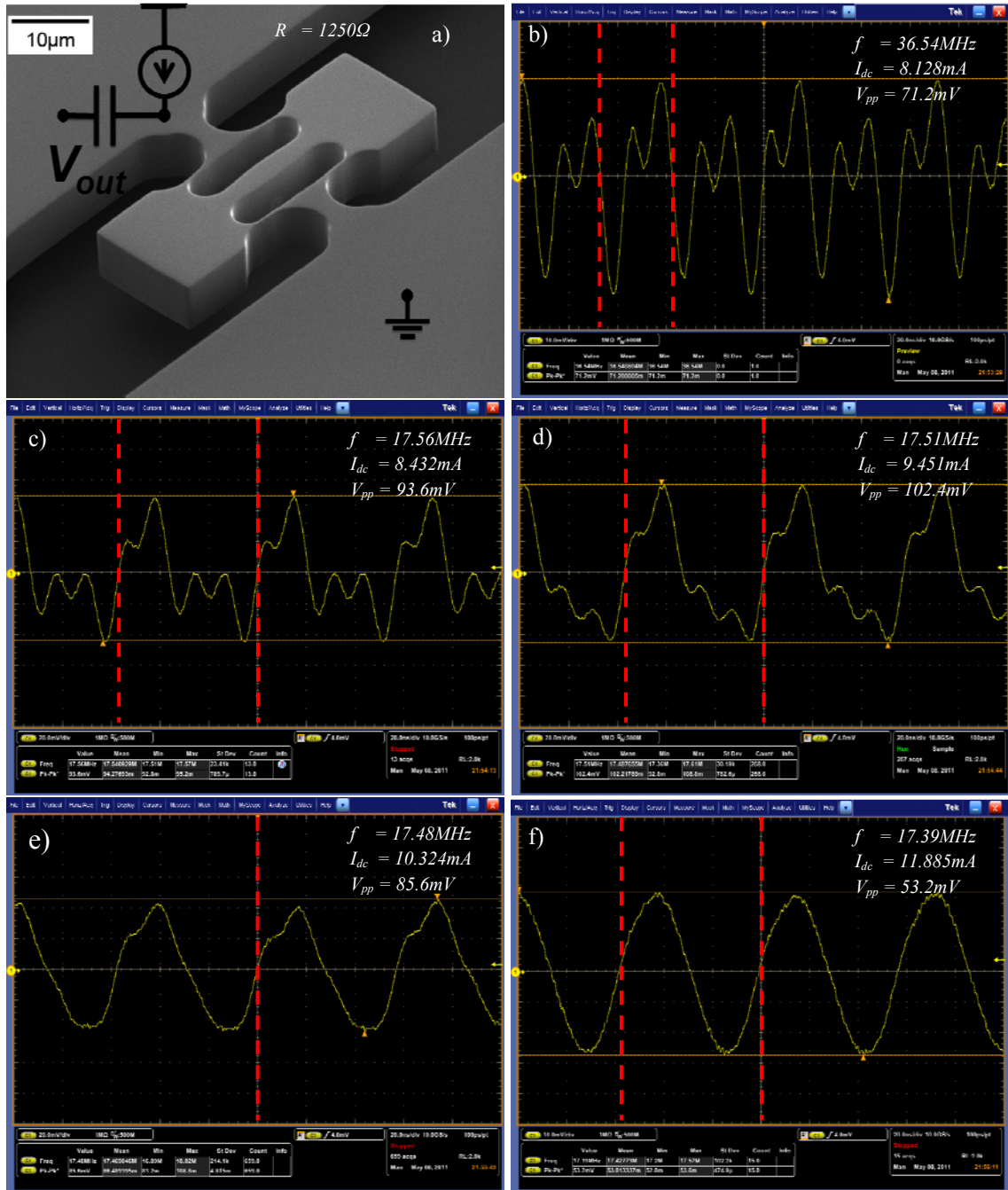
Figure 5.10. a) SEM view of a fabricated dual-mode silicon I3 resonator with oscillation frequencies of b) 36.54MHz at Ibias=8.128mA, c) 17.56MHz at Ibias=8.432mA, d) 17.51MHz at Ibias=9.451mA, e) 17.48MHz at Ibias=10.324mA and f) 17.39MHz at Ibias=11.885mA both under atmospheric pressure. All the waveforms have the same time interval

A closer look at the mode shape for the fundamental in-plane resonant mode of

the structure reveals that the deformation of the narrow actuator beams is a combination

of both extensional and flexural deformations. Figure 5.11 shows that as the resonator moves from its fully extended state to its fully compressed state in half of the resonance cycle, the narrow support beams go from a fully bent state to their normal straight shape and back into another bent state. Each time the beams flex there will be an increase in their length leading to a frequency component at twice the vibration frequency of the resonator.

Vibration Direction
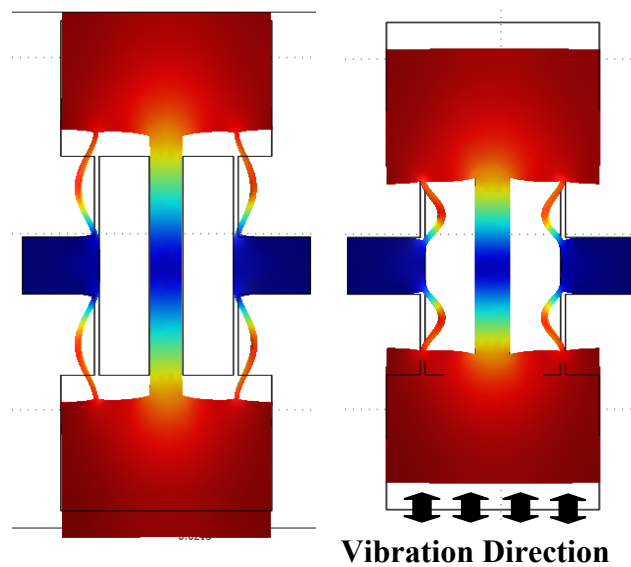
Figure 5.11. COMSOL modal analysis results showing the fundamental in-plane resonance mode-shape for an I3 resonator at its maximum expansion and compression points. It demonstrates that the deformation of narrow thermal actuators is a combination of flexural and extensional deformations and the frequency of the longitudinal deformations of the narrow beams due to flexural deformation is twice the resonance frequency of the resonator.

As shown in Fig. 5.10, by changing the applied DC bias current each of these frequency components can become the dominant component determining the output frequency of the oscillator.

6. ROTATIONAL MODE DISK RESONATORS FOR HIGH-Q OPERATION IN LIQUID

Micromechanical resonators, with their ultra-high resolution mass sensing capabilities, can provide significant new opportunities in biochemical sensing leading to more versatile, compact and low-cost tools and instruments for bio-analysis, medical diagnostics and drug discovery. However, most of the biosensing applications require sensing certain biomolecules in a liquid solution (typically aqueous). On the other hand, unlike larger scale mechanical resonators such as quartz crystal microbalance (QCM) and surface acoustic wave (SAW) resonant sensors, the resonant behavior of microscale resonant devices drastically deteriorate in liquid. This is mainly due to the larger surface to volume ratio for such smaller scale devices and consequently larger viscous damping to elastic energy ratio in them.

6.1   Past Resonant Structures for Operation inside Liquid

Several efforts have been made to operate micromechanical resonant devices in water. Magnetically actuated cantilever beams resonating in their out-of-plane flexural modes (Fig. 6.1a) have been used for mass sensing applications in aqueous environments [46-49]. However, excessive viscous damping reduces the quality factor of such devices to values as low as 5[46], 23[47], 2[48] and 10[49] in water. Quality factor of 67 has been demonstrated in liquid for a cantilever beam operating in its in-plane resonant mode [50] (Fig. 6.1b). Higher quality factor of the in-plane resonant mode in liquid is attributed to having a much smaller portion of its surface area stroking against the liquid interface compared to the out of plane cantilevers. In a more successful effort by Seo, et al [35], a

dual-half-disk structure comprised of two half-disks, resonating in an in-plane mode similar to the rotational mode of a disk (Fig. 6.1c), demonstrated quality factors as high as 94 in water. Similar to the in-plane flexural mode of microcantilivers, the straight sides of the half disks still have a perpendicular motion against the liquid interface. This suggests that there should be plenty of room for improvement and achieving higher quality factors.
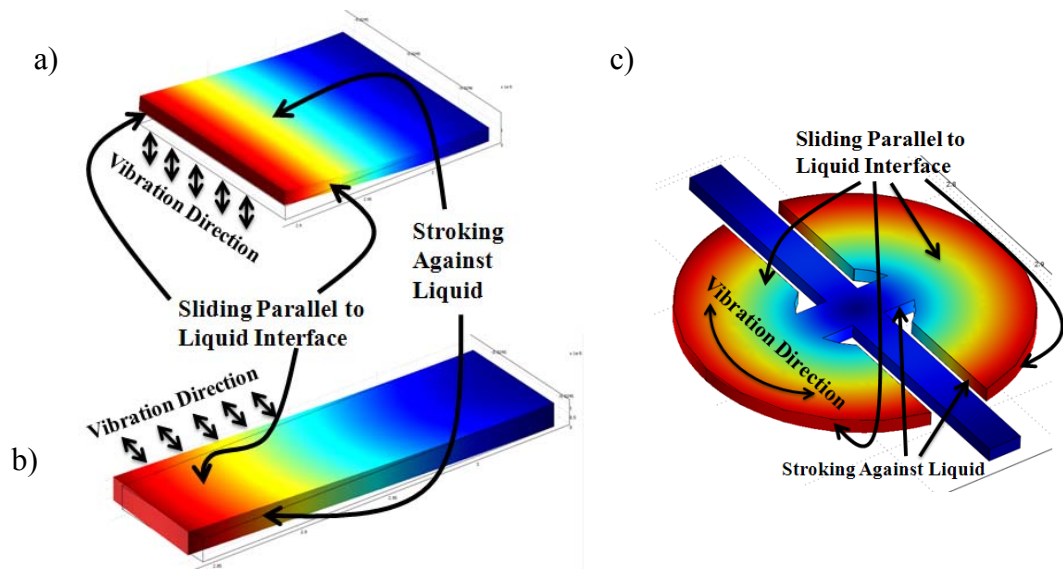
Figure 6.1. Finite element modal analysis of different resonant structures used in other works for operation in liquid, showing the mode shape and the direction of vibration and identifying surfaces which move perpendicular or parallel to the liquid interface (red is the maximum and blue is the minimum vibration amplitude): a) Out-of-plane flexural mode of a microcantiliver [46-49] b) In-plane flexural mode of a microcantiliver [50] c) Quasi-rotational mode of a dual-half-disk resonator [35].

Table 6.1 compares the data obtained from previously demonstrated resonators operating in water with results from this work. For all out-of-plane micro-cantilevers not only the quality factor drops drastically in liquid to less than 3% of its value in air, but also there is a significant reduction in resonant frequency (up to 85% reduction). However, as the resonator Q performance in liquid improves, the drop in resonant

frequency also decreases. This shows a clear connection between liquid mass loading and viscous damping.

The dual-half-disk design [35] has relatively higher quality factors and shows a frequency drop of less than 3% in water. Finally for the whole disk resonator topology in this work, the change in resonant frequency from air to water is less than 1% which further confirms the minimal liquid mass loading and therefore the superiority of the utilized resonant mode for operation in liquid.

Table 6-1. A brief comparison between the previously demonstrated micromechanical resonators operated in liquid and the results from this work.

Resonator Structure	f_{air} (KHz)	f_{water} (KHz)	Q_{air}	Q_{water}	Q_{water}/Q_{air} %	f_{water}/f_{air} %
Out-of-plane micro-cantiliver [46]	160	23	200	5	2.5	14.4
Out-of-plane micro-cantiliver [47]	400	200	1000	23	2.3	50
Out-of-plane micro-cantiliver [48]	50	16	70	2	2.9	32
Out-of-plane micro-cantiliver [49]	-	200	1000	10	1	-
In-plane micro-cantiliver [50]	-	2000	4000	67	1.7	-
Rotaional mode two-half disk [35]	601	585	1200	94	7.8	97.3
Rotational mode whole disk (This Research)	5724	5703	1140	284	25	99.6
	7391	7323	756	183	24	99.1

6.2 Rotational Mode Disk Resonators

In this research a rotational mode whole disk resonant structure with two tangential support beams has been proposed and demonstrated that can resonate with all its surfaces sliding parallel to the liquid interface (rather than stroking against it) [51]. This is expected to further limit the turbulences caused by the resonator in the

surrounding liquid and therefore minimize leakage of kinetic energy (i.e. maximize resonator quality factor).

6.2.1   Device Operation and Concept

Figure 6.2 shows the schematic view of the proposed resonant structures in this work. The resonator is comprised of a disk and two tangential support beams. Other than being structural supports, the beams act as both thermal actuators and piezoresistive stress sensors simultaneously [38]. Thermal actuation occurs by passing a current between the two pads on the two sides of the structure. Due to the tangential positioning of the support beams, such thermal stress can actuate the disk in its rotational resonance mode (periodically rotating back and forth). As a result, all the vibrating surfaces of the structure (including both the disk and the support beams) move in parallel to the liquid interface causing minimal turbulence in the surrounding liquid. Figure 6.3 shows the COMSOL modal analysis results for a 100µm diameter, 20µm thick disk with 4µm wide, 26µm long support beams.
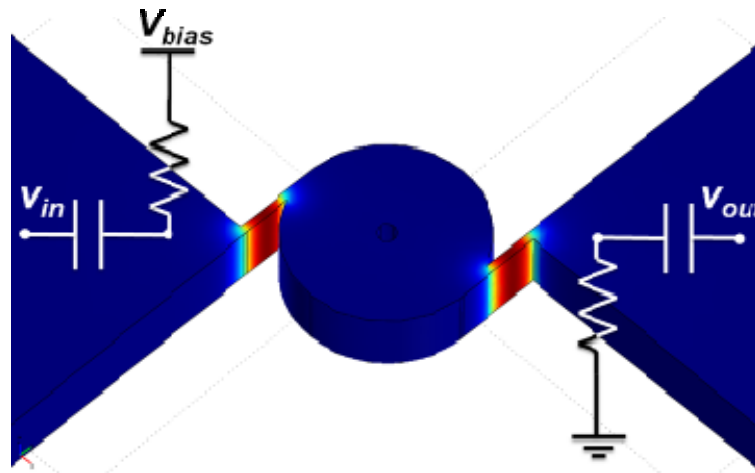
Figure 6.2. Schematic view of a thermally actuated disk resonator showing the qualitative distribution of AC temperature fluctuation amplitude in the resonator (red being the maximum and blue minimum). The electrical connections required for one-port operation of the resonator are also shown.

Since the longitudinal stress in the support beams in such resonators is directly transferred to the support pads, they are not expected to have high quality factors in air or under vacuum (due to excessive support loss). However, when operating in liquid the viscous damping is expected to be much larger than the relatively large support loss, making its effect negligible.
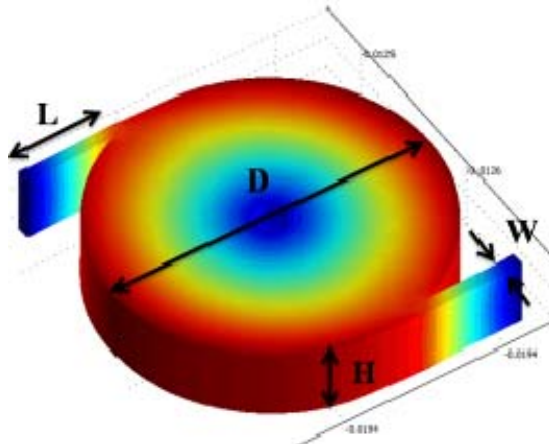
Figure 6.3. Finite element modal analysis of the rotational resonant mode of the proposed disk structure. Red and blue show the maximum and minimum vibration amplitudes respectively.

6.2.2   Resonator Fabrication

Single crystalline silicon rotational mode disk resonators with different dimensions were fabricated using the standard single mask SOI-MEMS process [38]. Resonators were fabricated on low resistivity N-type substrates with different device layer and BOX thicknesses. Figure 6.4 shows the SEM view of a fabricated 100μm diameter, 20μm thick disk resonator with 4μm wide support beams. To optimize resonator electromechanical transduction, the support beams are aligned to the <100> crystalline direction where the longitudinal piezoresistive coefficients are maximum. The hole in the middle of the disk is to reduce the undercut time in HF and due to its circular shape, it is expected to have negligible effect on viscous damping of the resonator.
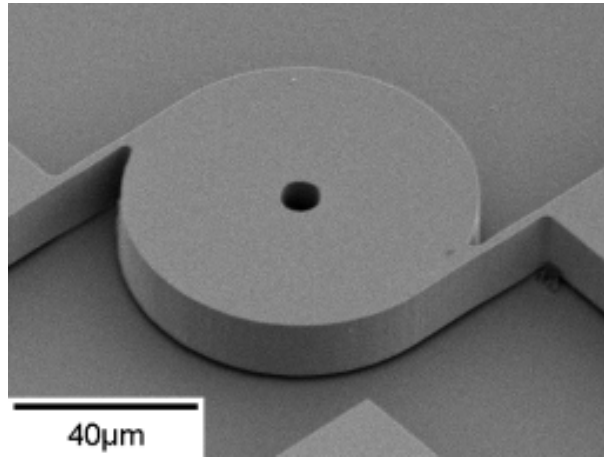
Figure 6.4. SEM view of a fabricated 100μm diameter disk resonator fabricated on an N-type low resistivity silicon substrate with device layer and BOX thickness of 20μm and 2μm respectively. The thermal actuators are along <100> crystalline direction for optimized transduction.

6.2.3   Measurement Results

The resonators were tested in a one-port configuration as shown in Fig. 6.2. Figure 6.5 shows the measured frequency responses for the 100μm disk resonator of Fig. 6.4 with different bias currents both in air and water. As expected, the resonators have relatively low quality factors in air (due to excessive support loss), however, unprecedented quality factors as high as 284 were measured in water (3X improvement compared to the previous record). Such high Q values in water confirm our hypothesis that elimination of the stroking surfaces from the mode shape can significantly improve resonator Q in liquid.

As shown in Fig. 6.5, as the resonator bias current increases resonance frequency decreases in air while it increases in water. Reduction of the frequency in air at increased bias currents is a result of the increased resonator static temperature at higher currents and the negative temperature coefficient of frequency for silicon resonators. This common trend is observed in almost all thermally actuated resonators. The opposite trend

observed in water is suspected to be due to reduction of the coupling of water molecules

to the silicon surface as a result of the increased temperature. Furthermore, the substantial

increase in the resonator quality factor at higher currents is in line with this explanation.

As the coupling to the surrounding fluid molecules decreases, fluid viscous damping

decreases as well.
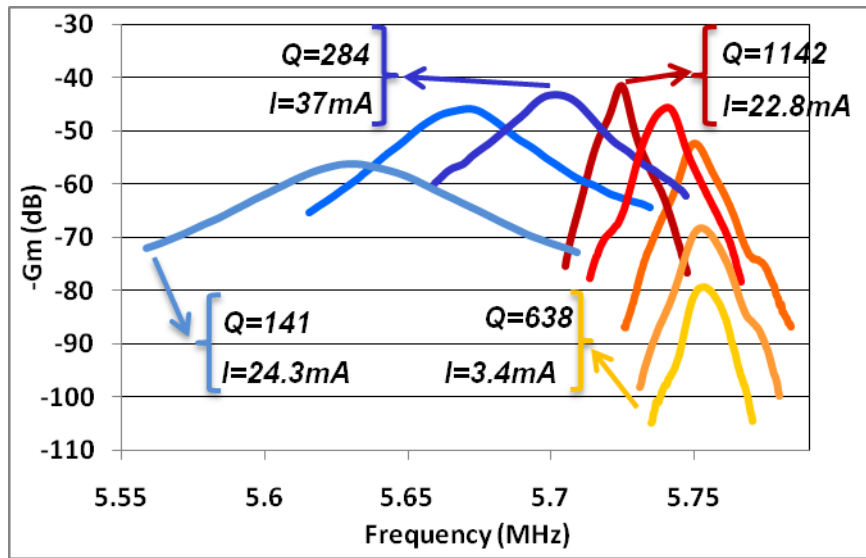
Figure 6.5. Measured frequency responses for the thermally actuated 5.6MHz resonator of Fig. 6.4 with different bias currents. Red and blue plots refer to air and water testing conditions respectively.

Table 6.2 summarizes the measurement results for three different disk resonators

fabricated on different SOI substrates with device layer thicknesses of 20, 10 and 3µm

respectively. As expected, the thicker resonator with the highest volume to surface ratio

has the highest quality factor in liquid.

The relatively thin BOX of the initial SOI substrates seems to be one of the major

factors limiting the quality factor of the resonators in this work. The liquid trapped in the

narrow gap between the SOI handle layer and resonator bottom surface, can cause

significant viscous damping. Higher quality factors are expected to be achievable using

Table 6-2. Summary of measurement results obtained from three disk resonators with different dimensions in both air and water with different bias currents.

Resonator Dimensions (μm)					Current (mA)	Cond.	Q	Freq. (MHz)	g_m (μA/V)	R (Ω)	Power (mW)
D	L	W	H	BOX							
100	26	4	20	2	3.4	Atm.	638	5.7543	-1.15	300	3.47
					15.6	Atm.	805	5.7476	-35.6	300	73.0
					22.8	Atm.	1142	5.7244	-84.5	300	155
					24.3	Water	141	5.6363	-16.4	300	177
					29	Water	181	5.6681	-35.1	300	252
					36	Water	216	5.6744	-52.5	300	388
					36.5	Water	240	5.7145	-75.7	300	410
					37	Water	284	5.7032	-71.2	300	410
100	11.5	4	10	4	17	Atm.	706	7.4322	-2.92	48	13.8
					59.4	Atm.	756	7.3906	-45.8	48	169
					51.9	Water	183	7.3232	-5.29	48	129
					62.8	Water	113	7.3591	-17.8	48	189
					79	Water	141	7.3981	-13.7	48	299
100	26	4	3	2	0.5	Atm.	6425	5.3138	-1.17	160	0.04
					2.4	Atm.	5435	5.3139	-27.0	160	0.92
					13.8	Atm.	5580	5.3163	-969	160	30.4
					12.8	Water	79.3	5.1692	-2.39	160	26.2
					15.3	Water	50.5	5.1943	-5.49	160	37.4

SOI substrates with thicker BOX layers resulting in wider underlying gap between the resonators and the handle substrate. Furthermore, according to the thermal-piezoresistive resonator modeling presented in [38], narrower actuator beams can significantly reduce the resonator power consumptions.

In order to further characterize rotational mode disk resonator quality factors, five different variations of single and multiple-coupled rotational mode disk resonators were fabricated (Fig. 6.6); 1. Single disks with straight tangential support beams, 2. Single disks with rounded support beams, 3. Parallel dual-
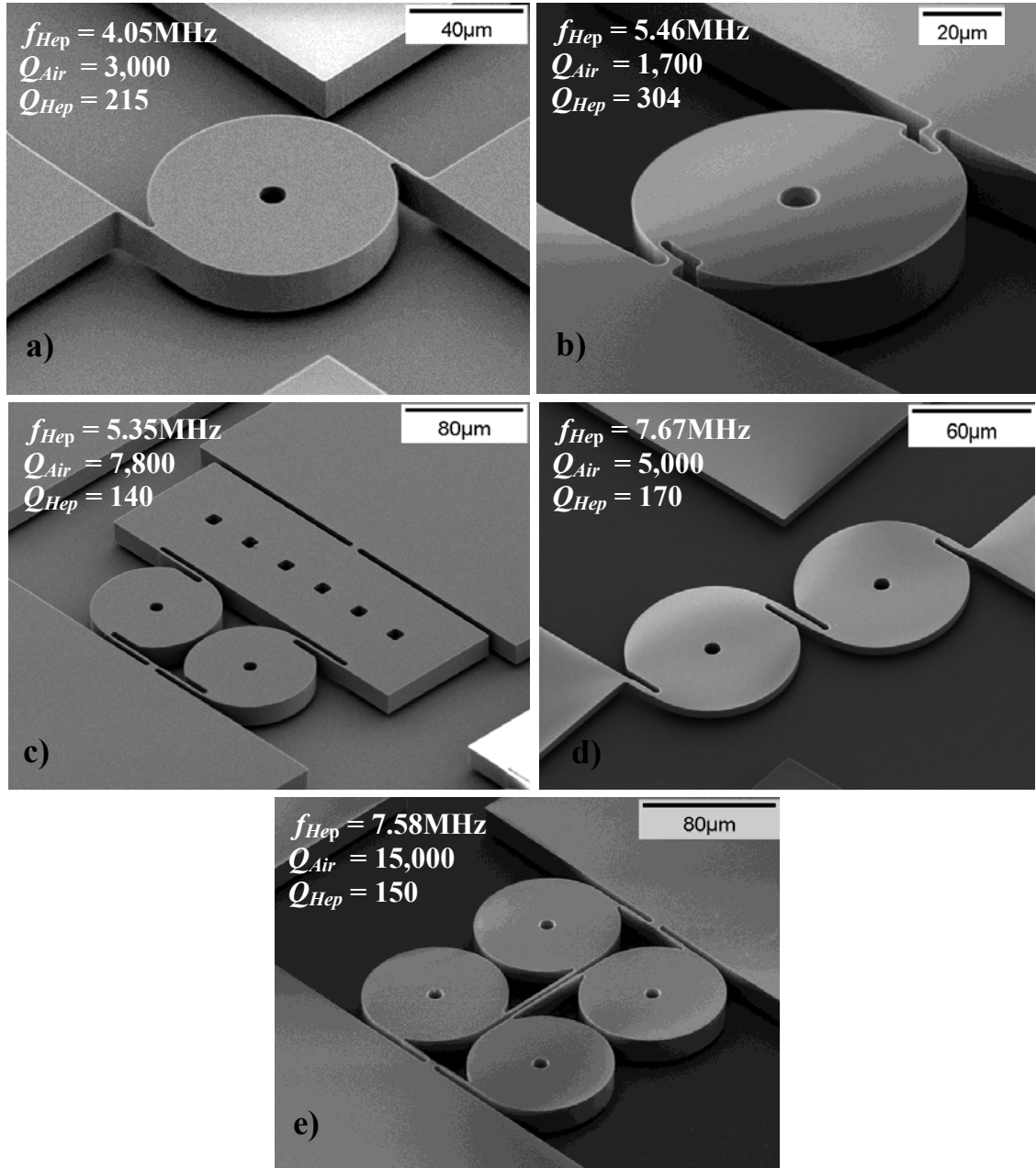
Figure 6.6. SEM view of fabricated devices along with their measured Q in both air and liquid for: a) single disk with straight tangential support beam, b) single disk with rounded support beam, c) parallel dual-disk, d) series dual-disk, e) interconnected quad-disk. The thermal actuators are along <100> crystalline direction for optimized transduction.

disks, 4. Series dual-disks, and 5. Interconnected quad-disks [52]. The resonators were

tested in a one-port configuration as shown in Fig. 6.2. The liquid tests were performed in

heptane to provide better electrical isolation and avoid contamination resulting from

electrolysis of water. Figure 6.7 shows the measured frequency responses for the 100µm

single disk resonator of Fig. 6.6b with rounded thermal actuators both in air and heptane. As expected, the resonator has relatively low quality factors in air (due to excessive support loss), however, unprecedented quality factor of 304 was measured in heptane. Such high Q values in heptane confirm our hypothesis that elimination of the stroking surfaces from the mode shape can significantly improve resonator Q in liquid.
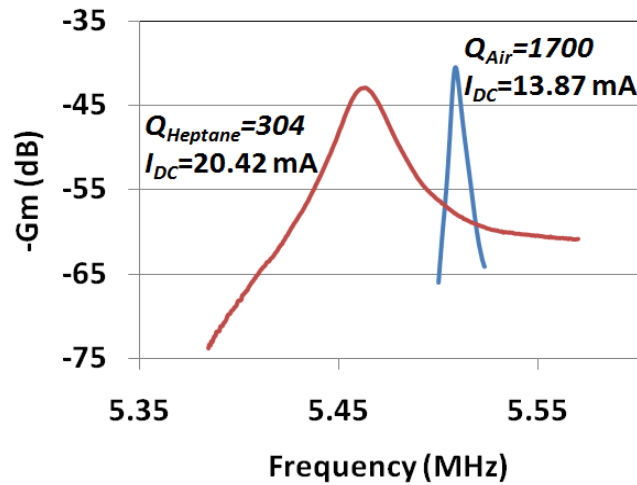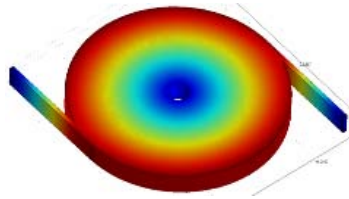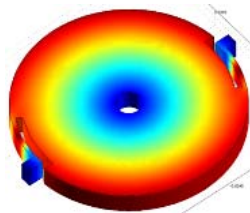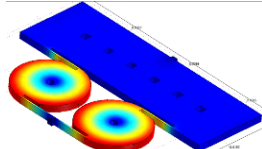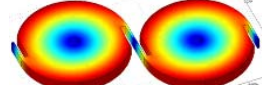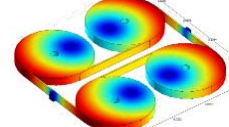
Figure 6.7. Measured frequency response for the 100μm diameter 20μm thick disk resonator shown in Fig. 6.6b with rounded support beams in air and heptanes.

Table 6.3 summarizes the measurement results for a variety of resonators of different types with different dimensions in both air and liquid. It also shows the finite element modal analysis for different structures demonstrating the vibration amplitude at different parts of the structure. The modal analysis results show that unlike the other structures the interconnected quad- disks have an off-center rotation which justifies their lower Q in liquid despite their relatively high Q in Air.

Table 6-3. Measurement results, and mode shapes for different types of single and multiple disk rotational mode resonators. Measurement results in both air and liquid (heptanes) are presented (w=2µ meter for all the support beams).

Type	Finite Element Modal Analysis Showing Resonant Mode Shape	Resonator Dimensions (µm)			Freq.·Air (MHz)	Q.·Air	Freq.·Hep. (MHz)	Q.·Hep.
		D	L_{th}	H				
Single Disk with Straight tangential support beam		100	42	5	5.500	3500	5.500	145
				10	5.144	1900	5.144	175
				20	4.052	3000	4.052	215
			17	5	6.827	2000	6.827	155
				10	6.427	1100	6.427	180
				20	5.356	1100	5.356	180
		200	55.5	5	2.586	4200	2.586	90
				10	2.383	700	2.383	170
				20	1.767	11700	1.767	110
			35	5	3.368	2800	3.368	100
				10	2.849	3000	2.849	180
				20	3.056	1400	3.056	220
Single Disk with Rounded support beam		100	24	10	7.174	3500	7.174	235
				20	4.152	3800	4.152	230
			11	5	7.366	1400	7.366	185
				10	8.406	600	8.406	195
				20	5.463	1700	5.463	304
		200	40	5	2.781	4900	2.781	95
				10	2.911	2600	2.911	230
				20	1.851	8500	1.851	160
			24	5	3.394	4000	3.394	120
				10	3.513	1100	3.513	150
				20	2.616	5500	2.616	220
Parallel Dual-Disk		100	114	5	5.594	8000	5.594	125
				10	5.627	6500	5.627	105
				20	3.973	2000	3.973	180
			103	10	5.350	7800	5.350	140
				20	3.752	2300	3.752	140
Series Dual-Disk		100	42	5	7.673	5000	7.673	170
				10	7.396	5000	7.396	180
				20	5.632	3200	5.632	180
Interconnected Quad-Disk		100	84	5	7.517	13500	7.517	155
				10	7.581	15000	7.581	150
				20	5.386	4800	5.386	50

6.2.4   Q Limiting Factors in Rotational Mode Disk Resonators

The axial stress in all the support beams of the single disk designs and half of the support beams in dual-disks is directly transferred to their clamping points and consequently into the substrate. Therefore, in air, where Q is mainly limited by support loss, the Q of single disk designs is generally smaller than that of the dual-disks, which is in turn smaller than that of the quad-disks. In liquid however, viscous damping becomes

the dominant source of loss and the Q for all designs drops to values in the 100-300 range. Although the highest Q of 304 in heptane obtained from the single disk structure with rounded supports of Fig. 6.6b, not much of a difference was observed between the performance of single disks with straight and rounded thermal actuators. Although higher quality factors are expected from the thicker resonators due to their smaller surface to volume ratio, measurement results do not show any significant improvement in quality factor of 20μm thick devices compared to 5μm thick devices. This suggests that most of the viscous damping is associated with the resonator sidewalls rather than their upper and lower surfaces. Resonator sidewall area is proportional to the resonator thickness and consequently the amount of elastic energy stored in the resonator. Therefore, if the sidewalls are the main source of loss no significant dependence of resonator quality factor to its thickness is expected. This could be blamed on the sidewall roughness caused by deep reactive ion etching, slight bending of support beams during resonance and off-center rotation of the disks due to fabrication induced asymmetries. Figure 6.8a and b demonstrate the bending of the rounded and straight support beams during the rotational
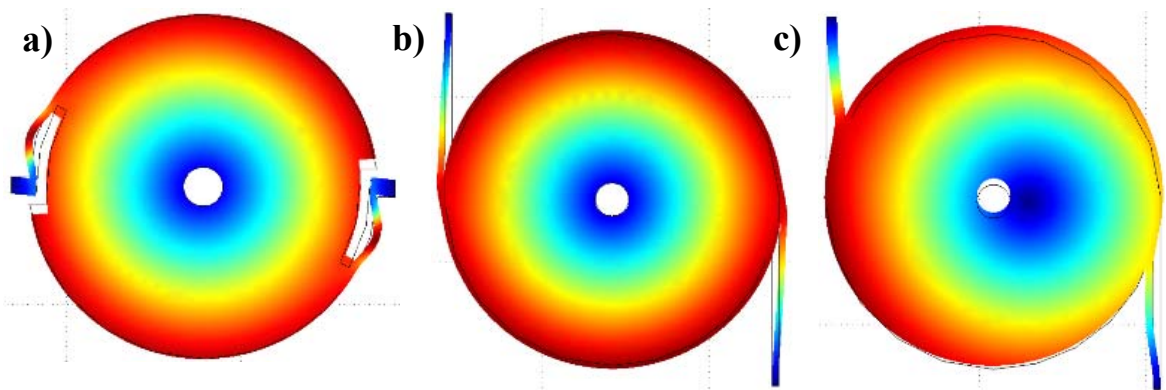
Figure 6.8. Finite element modal analysis showing different effects potentially limiting resonator quality factors in liquid: a,b) bending support beams stroking against the surrounding liquid, c) mismatched support beams causing off-center resonance. In this extreme case, the support beams have widths of 2μm and 3μm and equal lengths.

vibration of the disks and Fig. 6.8c shows the effect of a fabrication induced asymmetry on the resonance mode of single disks which causes off-center rotation and therefore stroking against the liquid interface.

7. CONCLUSIONS AND FUTURE WORKS

7.1   Contributions

The following is a list of contributions that have been achieved in this work.

- Equivalent electrical circuit for one-port high frequency thermally actuated I^2-Bulk acoustic wave resonators (I^2BAR) with piezoresistive readout in their in-plane extensional mode was derived. Then based on the model it was shown that not only by scaling down all the dimensions resonance frequency increases but also the performance of thermal actuation improves.

- High frequency single crystal silicon (SCS) thermally-piezoresistive I^2BARs were fabricated on regular SOI substrates using a Single mask SOI-MEMS process. The resonators were tested using one-port configuration. Resonance frequencies as high as 61MHz and quality factors as high as 14,000 were demonstrated. It was shown that in such resonators by narrowing the widths of thermal actuators power consumption decreases while electromechanical coupling increases. For such optimized resonators power consumptions as low as 4µW with quality factors as high as 40,000 were demonstrated. In addition by fabricating similar resonators but with different scales, the claim for increase in performance of thermal actuation at higher frequencies was practically confirmed. Then by having the results for a 61MHz resonator, using the model the performance of two scaled down versions of that resonator with resonance frequencies of 900MHz and 2.1GHz was investigated.

- A new controlled batch fabrication method for fabricating silicon nanowires based on crystalline structure of silicon was demonstrated. It takes advantage of the uneven

91

etch rates of different crystalline planes of silicon in alkaline solutions. It gives ultimately smooth surfaces with atomic level precision. Such fabrication method was employed to fabricate thermally actuated resonators with piezoresistive readout with submicron wide thermal actuators. It was demonstrated that the resulted resonant structures need bias currents less than one mili Amp to provide quality factors as high as 20,000.

- The internal positive feedback in thermal-piezoresistive resonators was demonstrated using both practical data and the electrical equivalent model for such resonators. It was shown that based on the applied bias current the active electrical power can compensate for all or at least part of mechanical losses. For lower DC bias currents, only a part of mechanical losses would be compensated leading to self-Q-enhancement in such resonators. Quality factors as high as a few millions were demonstrated for such devices. By further increasing the bias current, all the mechanical losses would be compensated leading to self-sustained-oscillation without the need for any electronic amplification circuitry. Self-oscillator structures with frequencies as high as 21MHz were demonstrated.

- A thermal-piezoresistive rotational-mode disk resonator structure was demonstrated that can operate inside liquid. It was shown that the implemented structure provides higher quality factors than the previously operated MEMS resonant structures inside liquid. Then five different variations of single and multiple-coupled rotational mode disk resonators were fabricated and characterized inside liquid. Since the thickness of the fabricated resonators didn't affect their quality factors, it was suggested that the

main energy loss mechanism in such structure happens through their sidewalls. This could be blamed on the sidewall roughness caused by deep reactive ion etching, slight bending of support beams during resonance and off-center rotation of the disks due to fabrication induced asymmetries.

Below is a list of invention disclosures, journal and refereed conference papers, that have so far occurred under this research:

7.1.1   Invention Disclosures

1. S.   Pourkamali,   and   A.   Rahafrooz,   "Self-Sustained   High-Frequency Micro/Nanomechanical Extensional Mode Oscillators," September 2010.

2. S. Pourkamali, and A. Rahafrooz, "Rotational Mode Disk Resonators for High-Q Operation in Liquid," September 2010.

3. S. Pourkamali, and A. Rahafrooz, "A Nano-Precision Fabrication Technique for Controlled Batch Fabrication of Crystalline Nanowires," October 2009.

7.1.2   Journal Publications

1. A. Rahafrooz, and S. Pourkamali, "Controlled batch fabrication of crystalline silicon nanobeam-based resonant structures," Planned submission in near future.

2. A. Rahafrooz, and S. Pourkamali, "Rotational mode disk resonators for High-Q operation in liquid," Planned submission in near future.

3. A. Rahafrooz, and S. Pourkamali, "Thermal-Piezoresistive Energy Pumps in Micromechanical Resonant Structures," Ready for submission.

4. A. Rahafrooz, and S. Pourkamali, "High-frequency thermally actuated electromechanical resonators with piezoresistive readout," IEEE Trans. On Electron Device, 2011, Vol. 58, issue 4, pp. 1205-1214.

5. A. Rahafrooz, S. Pourkamali," Fabrication and characterization of thermally actuated micromechanical resonators for airborne particle mass sensing: I. Resonator design and modeling", Journal of Micromechanics and Microengineering, Volume: 20 Issue: 12 Article Number: 125018, Nov 2010.

6. A. Hajjam, J. C. Wilson, A. Rahafrooz, S. Pourkamali," Fabrication and characterization of thermally actuated micromechanical resonators for airborne particle mass sensing: II. Device fabrication and characterization", Journal of Micromechanics and Microengineering, Volume: 20 Issue: 12 Article Number: 125019, Nov 2010.

7. A. Rahafrooz, S. Pourkamali,"Detection of sub-ppm traces of aqueous heavy-metal ions using micro-electro-mechanical beam resonators", Journal of Micromechanics and Microengineering Volume: 19 Issue: 11 Article Number: 115003. Nov 2009.

8. Yun-Bo Yi, A. Rahafrooz, S. Pourkamali, "Modeling and testing of the collective effects of thermoelastic and fluid damping on silicon MEMS resonators", J. Micro/Nanolith. MEMS MOEMS, Vol. 8, 023010 (2009).

7.1.3 Refereed Conference Papers

1. A. Rahafrooz, S. Pourkamali, "High Frequency Dual-Mode Thermal-Piezoresistive Oscillators," IEEE IIFCS and EFTF 2011, In Press.

2. A. Rahafrooz, S. Pourkamali, "Characterization of Rotational Mode Disk Resonator Quality Factors in Liquid," IEEE IIFCS and EFTF 2011, In Press.

3. A. Rahafrooz, S. Pourkamali, "Active self-Q-enhancement in high frequency thermally actuated M/NEMS resonators," IEEE MEMS 2011.

4. A. Rahafrooz, S. Pourkamali, "Controlled batch fabrication of crystalline silicon nanobeam-based resonant structures," IEEE MEMS 2011.

5. A. Hajjam, A. Rahafrooz, S. Pourkamali, "Temperature compensated single-device electromechanical oscillators," IEEE MEMS 2011.

6. A. Hajjam, J. Wilson, A. Rahafrooz, and S.Pourkamali, "Self-sustained micromechanical resonant particlute microbalance/counters," IEEE MEMS 2011.

7. A. Rahafrooz, and S. Pourkamali, "Fully Micromechanical Piezo-Thermal Oscillators," IEEE International Electron Device Meeting (IEDM), 2010.

8. A. Hajjam, A. Rahafrooz, and S. Pourkamali, "Sub-100ppb/ºC Temperature Stability in Thermally Actuated High Frequency Silicon Resonators via Degenerate Phosphorous Doping and Bias Current Optimization," proceedings, IEEE International Electron Device Meeting (IEDM), 2010.

9. A. Rahafrooz, and S. Pourkamali, "Rotational Mode Disk Resonators for High-Q Operation in Liquid," IEEE Sensors Conference, 2010.

10. A. Hajjam, J. Pandiyan, A. Rahafrooz, and S. Pourkamali, "MEMS Resonant Sensors for Detection of Gasoline Vapor," IEEE Sensors Conference, 2010.

11. A. Hajjam, J. Wilson, A. Rahafrooz, and S. Pourkamali, "Detection and Mass Measurement of Individual Air-Borne Particles Using High Frequency Micromechanical Resonators," IEEE Sensors Conference, 2010.

12. A. Rahafrooz, and S. Pourkamali, "Thermo-electro-mechanical modeling of high frequency thermally actuated I^2-BAR resonators," Hilton Head 2010, solid-state sensor, actuator and Microsystems workshop.

13. A. Rahafrooz, A.Hajjam, B.Tousifar, and S.Pourkamali, "Thermal actuation, a suitable mechanism for high frequency electromechanical resonators," Proceedings, IEEE MEMS 2010.

14. A. Hajjam, J. Wilson, A. Rahafrooz, and S.Pourkamali, "Fabrication and characterization of resonant aerosol particle mass sensors," Proceedings, IEEE MEMS 2010.

15. A. Hajjam, A. Rahafrooz, J.C. Wilson, and S.Pourkamali, "Thermally actuated MEMS resonant sensors for mass measurement of micro/nanoscale aerosol particles," Proceedings, IEEE Sensors 2009.

16. A. Rahafrooz, A. Hajjam, S. Pourkamali, "Thermal Actuation of High Frequency Micromechanical Resonators", IEEE international SOI conference, 2009.

17. A. Rahafrooz, S. Pourkamali, "Resonant MEMS sensors for detection of aqueous heavy metal ions with Sub-ppm resolution", IEEE International Conference on Electron Devices and Solid-State Circuits, 2008. EDSSC 2008.

7.2   Future Directions

The developed high frequency thermal-piezoresistive MEMS resonators have an ultimately simple fabrication process. The fabricated resonators don't require any sort of transduction gaps that may be clogged in sensing applications. In addition, their in-plane mode of vibration provides almost an even mass sensitivity which is an advantage in mass sensing applications. These resonators due to their active nature, by providing self – Q-enhacemnt and self-suiatined oscillation capabilities can open a new set of applications. Then there is no wonder that such structures have a great positional for commercialization. To reach this goal there are some areas that may pave the way as follows:

- Two-Port Resonators: although having one-port structure is beneficial (or even mandatory in case self-sustained oscillators), for some applications it is desired to have two-port thermal-piezoresistive structures. Due to the lower feed through, a two-port resonator can be easily put inside a positive feedback loop to form an oscillator or at least boost its Q. The other application of two-port resonators is in fabrication of mechanical filters.

- Nanoscale devices with frequencies in GHz range: based on the derived model it is demonstrated that having nanoscale devices with optimal design would have an improved performance. To further investigate this claim, submicron and nanoscale resonators can be fabricated using electron-beam lithography. It is probale that self-Q-enhancement and oscillation can also be observed. In this case such structure may

be a potential candidate for higher frequencies as replacements for other MEMS structures with relatively smaller dimensions and lower cost.

- Lower Power Consumptions: It is known that lowering the width of thermal actuators decreases their power consumption. However, it also lowers the stiffness and therefore, the resonance frequency of the resonators. In another words, there is a compromise between higher resonance frequencies and lower power consumptions. In addition, changing the doping level of the structure can affect both the output signal level and the power consumption. By taking all these parameters into account, optimum design can be realized.

- Higher frequency self-oscillators: In this research oscillation frequencies up to 21MHz was shown for thermal-piezoresistive resonators. Achieving higher oscillation frequencies up to GHz range is among the goals. There may be some fabrication induced limitations regarding scaling down the oscillators and therefore a need for new resonator structures to achieve higher frequencies.

- Higher Oscillation Amplitudes: if the amplitude of the self-oscillatiors is high enough, their output can be directly connected to other communication components without the need for amplification. Therefore, there is a need to completely recognize the parameters limiting the oscillation amplitude. To do so, the effect of dimensions of the thermal actuators, their structure and doping level should be investigated. Knowing the effect of each of these parameters and the complete mechanism, the optimized design can be implemented.

- Higher Qs in liquid: achieving higher Qs in liquid increases the sensitivity of the structure and lowers the effect of noise. Vibration of thermal actuators is one of the main sources of energy loss in liquid. Proper design can be made to remove any stroking of the thermal actuators against the liquid. Other than that, by further smoothing the nanoscale and submicron roughnesses of the side walls, higher Qs are expected.

- Long Term Stability and Reliability: it is important that the resonance frequency and quality factor of the resonators experience no shift over time. There should be extensive characterization on different types of thermal-piezoresistive resonators.

- Fabrication tolerance characterization and compensation: frequency tolerance between fabricated resonators with same design and dimensions can a major issue in commercialization of a resonant based product. There have not been any characterization and measurement of frequency tolerance in this research. Therefore it is an open research area. Resonator designs that can be robust to slight dimensional changes due to fabrication tolerances are of great interest as a topic for further research.

REFERENCES

[1] A. Rahafrooz and S. Pourkamali, "Detection of sub-ppm traces of aqueous heavy-metal ions using micro-electro-mechanical beam resonators," *Journal of Micromechanics and Microengineering*, vol. 19, no. 11, 115003 (7pp), 2009.

[2] C. T. C. Nguyen, "MEMS technology for timing and frequency control," *IEEE Trans. on Ultrason., Ferroelectr., Freq. Control*, vol. 54, no. 2, pp. 251 – 270, Feb. 2007.

[3] S. Trolier-McKinstry, "Piezoelectric and Acoustic Materials for Transducer Applications." New York: Springer, 2008.

[4] H. Campanella, "Acoustic wave and electromechanical resonators," *Artech House Publication*, 2010.

[5] S.-M. Chang, H. Muramatsu, C. Nakamura, J. Miyake, "The principle and applications of piezoelectric crystal sensors," Materials Science and Engineering, vol. 12, no. 1-2, pp.111-123 August 2000.

[6] M. E. Frerking, "Fifty years of progress in quartz frequency standards," 1996 IEEE international frequency control symposium, pp. 33-46.

[7] Y. L. Vorokhovsky, B.G. Drakhlis, "High-stability quartz oscillators on internally heated quartz resonators with AT and SC cuts," Proceedings of the 45th Annual Symposium on Frequency Control, 1991, pp. 447 –451.

[8] P.V. Wright, "A review of SAW resonator filter technology," Ultrasonics Symposium, 1992. Proceedings., IEEE 1992 , vol., no., pp.29-38 vol.1, 20-23 Oct 1992

[9] Y. Satoh, T. Nishihara, T. Yokoyama, M. Ueda and T. Miyashita, "Development of piezoelectric thin film resonator and its impact on future wireless communication systems," *IEEE Japanese Journal of Applied Physics*, vol. 44, no. 5A, pp. 2883 – 2894, 2005.

[10] Lakin, K.M.; , "Thin film resonator technology," Proceedings of the 2003 IEEE International Frequency Control Symposium and PDA Exhibition Jointly with the 17th European Frequency and Time Forum, 2003., pp. 765- 778, 4-8 May 2003.

[11] G. Piazza and A. P. Pisano, "Dry-released post-CMOS compatible contour-mode aluminum nitride micromechanical resonators for VHF applications," proceedings, Hilton Head 2004, pp. 37-40.

[12] G. Piazza, P.J. Stephanou, A.P. Pisano, "Piezoelectric Aluminum Nitride Vibrating Contour-Mode MEMS Resonators," Journal of Microelectromechanical Systems, vol.15, no.6, pp.1406-1418, Dec. 2006.

[13]   G. Piazza, P.J. Stephanou, A.P. Pisano, "Single-Chip Multiple-Frequency ALN MEMS Filters Based on Contour-Mode Piezoelectric Resonators," Journal of Microelectromechanical Systems, vol.16, no.2, pp.319-328, April 2007.

[14]   S. Humad, R. Abdolvand, G. K. Ho, G. Piazza and F. Ayazi, "High frequency micromechanical piezo-on-silicon block resonators," IEDM '03 Technical Digest IEEE International Electron Devices Meeting, 2003., 2003, pp. 39.3.1 –39.3.4.Z.

[15]   B.P. Harrington, M. Shahmohammadi, R. Abdolvand, "Toward ultimate performance in GHZ MEMS resonators: Low impedance and high Q," 2010 IEEE 23rd International Conference on Micro Electro Mechanical Systems (MEMS), 2010, pp. 707 –710.

[16]   H. Fatemi, B.P. Harrington, H. Zeng, J. Carlisle, R. Abdolvand, "50Ω-terminated 900MHz monolithic lateral-extensional piezoelectric filters on ultrananocryslalline diamond," 2011 IEEE 24rd International Conference on Micro Electro Mechanical Systems (MEMS), 2011, pp. 744 –747.

[17]   M. Rinaldi, C. Zuniga, C. Zuo, G. Piazza, "Ultra-thin Super High Frequency two-port ALN contour-mode resonators and filters," International Solid-State Sensors, Actuators and Microsystems Conference, TRANSDUCERS 2009 , pp.577-580, 21-25 June 2009.

[18]   W.C. Tang, T.-C.C. Nguyen, R.T. Howe, "Laterally driven polysilicon resonant microstructures," Micro Electro Mechanical Systems, 1989, Proceedings, An Investigation of Micro Structures, Sensors, Actuators, Machines and Robots. IEEE , vol., no., pp.53-59, 20-22 Feb 1989.

[19]   J.R. Clark, H. Wan-Thai, C.T.-C. Nguyen, "High-Q VHF micromechanical contour-mode disk resonators," Electron Devices Meeting, 2000. IEDM Technical Digest. International , vol., no., pp.493-496, 2000.

[20]   X. Yuan, L. Sheng-Shian, L. Yu-Wei, R Zeying, C.T.C. Nguyen, "UHF micromechanical extensional wine-glass mode ring resonators," Electron Devices Meeting, 2003. IEDM '03 Technical Digest. IEEE International , vol., no., pp. 39.2.1-39.2.4, 8-10 Dec. 2003.

[21]   S. Pourkamali, Z. Hao and F. Ayazi, "VHF single crystal silicon side supported disk resonators-Part II: implementation and characterization," J. Microelectromech. Syst., vol. 13, no. 6, pp. 1054-1062, Dec. 2004.

[22]   S. Pourkamali, G. K. Ho, and F. Ayazi, "Vertical capacitive SiBARs," in Tech. Dig., 18th IEEE Int. MEMS Conf., Miami Beach, FL, Jan. 30‑Feb. 3, 2005, pp. 211‑214.

[23]   S. Pourkamali, G. K. Ho and F Ayazi, "Low-impedance VHF and UHF capacitive silicon bulk acoustic wave resonators," IEEE Trans. Electron Devices, vol. 54, no. 8, pp. 2017-2023, Aug. 2007.

[24]   S.A. Bhave, R.T. Howe, "Silicon nitride-on-silicon bar resonator using internal electrostatic transduction," in Proc. 13th Int. Conf. Solid-State Sens. Actuators (Transducers), Seoul, Korea, Jun. 2005, vol. 2, pp. 2139-2142.

[25]   D. Weinstein, S.A. Bhave, "Internal Dielectric Transduction of a 4.5 GHz Silicon Bar Resonator," IEEE International Electron Devices Meeting, 2007. IEDM 2007, pp.415-418, 10-12 Dec. 2007.

[26]   E. Hwang, S.A. Bhave, "PN-diode transduced 3.7-GHZ silicon resonator," 2010 IEEE 23rd International Conference on Micro Electro Mechanical Systems (MEMS), 2010, pp. 208 –211.

[27]   E. Hwang, S.A. Bhave, "Experimental verification of internal friction at GHZ frequencies in doped single-crystal silicon," 2011 IEEE 24rd International Conference on Micro Electro Mechanical Systems (MEMS), 2011, pp. 424 –427.

[28]   D. Grogg, M. Mazza, D. Tsamados, A. M. Ionescu, "Multi-Gate Vibrating-Body Field Effect Transistor (VB-FETs)," in *Proc. IEEE International Electron Devices Meeting (IEDM 2008)*, June 2008, San Francisco, CA, pp.663-666.

[29]   J.T.M. van Beek, G.J.A.M. Verheijden, G.E.J. Koops, K.L. Phan, C. van der Avoort, J. van Wingerden, D. Ernur Badaroglu, J.J.M. Bontemps, "Scalable 1.1 GHz fundamental mode piezo-resistive silicon MEMS resonator," in *Proc. IEEE International Electron Devices Meeting (IEDM 2007)*, Washington, DC, Dec. 2007, pp. 411 - 414 .

[30]   J.T.M. van Beek, K.L. Phan, G.J.A.M. Verheijden, G.E.J. Koops, C. van der Avoort, J. van Wingerden, D. Ernur Badaroglu, J.J.M. Bontemps, R. Puers, "A piezo-resistive resonant MEMS amplifier," in *Proc. IEEE International Electron Devices Meeting (IEDM 2008)*, June 2008, San Francisco, CA, pp.667-670.

[31]   J.J.M. Bontemps, A. Murroni, J.T.M. van Beek, J.A.T.M. van den Homberg, J.J. Koning, G.E.J. Koops, G.J.A.M. Verheijden, J. van Wingerden, K.L. Phan, P. Vermeeren, C. van der Avoort, H.C.W. Beijerinck, P.G.M. Baltus, "56 MHZ piezoresistive micromechanical oscillator," in *Proc. 16th International Conference on Solid-State Sensors, Actuators and Microsystems, Transducers 2009*, Denver, CO. June 2009, pp.1433 – 1436.

[32]   R. J. Wilfinger, P. H. Bardell, D. S. Chhabra, "The Resonistor: A Frequency Selective Device Utilizing the Mechanical Resonance of a Silicon Substratet," *IBM Journal of Research and Development,* 1968, vol.12 ,pp. 113 – 118.

[33]   R. B. Reichenbach, M. Zalalutdinov, J. M. Parpia, and H. G. Craighead, "RF MEMS Oscillator with Integrated Resistive Transduction,", *IEEE Electron Device Letters*, vol. 27, Oct. 2006, pp. 805-807.

[34]   K. L. Phan, P. G. Steeneken, M. J. Goossens, G. E.J. Koops, G. J.A.M. Verheijden, and J. T.M. van Beek, "Spontaneous mechanical oscillation of a DC driven single crystal," ArXiv 0904.3748, 2009.

[35]   J. H. Seo and O. Brand, "High Q-Factor In-Plane-Mode Resonant Microsensor Platform for Gaseous/Liquid Environment," *J. Microelectromech. Syst.*, vol. 17, no. 2, pp. 483-493, Apr. 2008.

[36]   A. Hajjam, A. Rahafrooz, J.C. Wilson, and S. Pourkamali, "Thermally Actuated MEMS Resonant Sensors for Mass Measurement of Micro/Nanoscale Aerosol Particles," in *Proc. 8th IEEE Sensors*, Christchurch, New Zealand, Oct. 2009, pp. 707-710.

[37]   G. K.Ho, K. Sundaresan, S. Pourkamali, F. Ayazi, "Micromechanical IBARs: Tunable High-Q Resonators for Temperature-Compensated Reference Oscillators," J. Microelectromech. Syst., vol. 19, no. 3, pp. 503-515, Jun. 2010

[38]   A. Rahafrooz, S. Pourkamali, "High-Frequency Thermally Actuated Electromechanical Resonators With Piezoresistive Readout," IEEE Transactions on Electron Devices, vol.58, no.4, pp.1205-1214, April 2011.

[39]   A. Rahafrooz, S. Pourkamali, "Active self-Q-enhancement in high frequency thermally actuated M/NEMS resonators," IEEE 24th International Conference on Micro Electro Mechanical Systems (MEMS), 2011, pp.760-763, 23-27 Jan. 2011.

[40]   A. Rahafrooz, S. Pourkamali, "Fully micromechanical piezo-thermal oscillators," 2010 IEEE International Electron Devices Meeting (IEDM), , vol., no., pp.7.2.1-7.2.4, 6-8 Dec. 2010.

[41]   A. Rahafrooz, A. Hajjam, B. Tousifar, S. Pourkamali, "Thermal actuation, a suitable mechanism for high frequency electromechanical resonators," 2010 IEEE 23rd International Conference on Micro Electro Mechanical Systems (MEMS), pp.200-203, 24-28 Jan. 2010.

[42]   A. Rahafrooz and S. Pourkamali, "Thermo-electro-mechanical modeling of high frequency thermally actuated I_2-BAR resonators," in *Proc. Tech. Dig. Solid-State Sens., Actuator, Microsyst. Workshop*, Hilton Head Island, SC, Jun. 2010, pp. 74–77.

[43]   R. He and P. Yang, "Giant piezoresistance effect in silicon nanowires," *Nat. Nanotechnol.*, vol. 1, no. 1, pp. 42–46, Oct. 2006.

[44] X. L. Feng, R. R. He, P. D. Yang, and M. L. Roukes, "Phase noise and frequency stability of very-high frequency silicon nanowire nanomechanical resonators," Proceedings, IEEE Transducers, 2007, pp. 327-330.

[45] Y. Uenishi, M. Tsugai, and M. Mehregany, "Micro-opto-mechanical devices fabricated by anisotropic etching of (110) silicon," Proceedings, IEEE MEMS '94, pp. 319 – 324.

[46] A. Vidic, D. Then, and C. Ziegler, "A new cantilever system for gas and liquid sensing," Ultramicroscopy, vol. 97, no. 1, pp. 407–416, Oct. 2003.

[47] Y. Li, C. Vancura, et al, "Very high Q-factor in water achieved by monolithic, resonant cantilever sensor with fully integrated feedback," in Proc. IEEE Sensors Conf., 2003, pp. 809–813.

[48] J. Tamayo, A.D.L. Humphris, A.M. Malloy, M.J. Miles, "Chemical sensors and biosensors in liquid environment based on microcantilevers with amplied quality factor," Ultramicroscopy, vol. 86, no 1-2, pp.167-173, Jan 2001.

[49] C. Vancura, Y. Li, J. Lichtenberg, K.U. Kirstein and A. Hierlemann, "Liquid-phase chemical and biochemical detection using fully integrated magnetically actuated complementary metal oxide semiconductor resonant cantilever sensor systems," Analytical Chemistry, vol. 79, no. 4, pp. 1646-1654, Feb. 2007.

[50] L.A. Beardslee, K.S. Demirci, Y. Luzinova, J.J. Su, B. Mizaikoff, S. Heinrich, F. Josse , O. Brand, "In-plane mode resonant cantilevers as liquid phase chemical sensors with ppb range limits of detection," in Tech. Dig. Solid-State Sens.,Actuator Microsyst. Workshop, Hilton Head Island, SC, Jun. 2010, pp. 23-26.

[51] A. Rahafrooz, and S. Pourkamali, "Rotational mode disk resonators for high-Q operation in liquid," proceedings, IEEE Sensors conference, 2010, pp. 1071-1074.

[52] A. Rahafrooz, S. Pourkamali, "Characterization of Rotational Mode Disk Resonator Quality Factors in Liquid," IEEE IIFCS and EFTF 2011, In Press.

[53] A. A. Barlian, W.T. Park, J. R. Mallon, J., A. J. Rastegar, and B. L. Pruitt,"Fabrication Review: Semiconductor piezoresistance for microsystems," Proceedings of the IEEE, vol. 97, no. 3, Mar. 2009, pp. 513-552.